

CORRELATION OF FRACTOGRAPHY, MICROSTRUCTURE AND
FRACTURE TOUGHNESS BEHAVIOR OF HIGH STRENGTH ALLOYS

by

JAMES ALBERT VAN DEN AVYLE

B.S., Purdue University
(1968)

S.M., Massachusetts Institute of Technology
(1969)

Submitted in partial fulfillment of the requirements

for the degree of

DOCTOR OF PHILOSOPHY

at the

Massachusetts Institute of Technology

February, 1975

Signature of Author

Department of (Metallurgy and) Material Science + E.
January 15, 1975

Certified by

Thesis Supervisor

Accepted by

Chairman, Departmental Committee on Graduate Students

ARCHIVES



ABSTRACT

CORRELATION OF FRACTOGRAPHY, MICROSTRUCTURE AND
FRACTURE TOUGHNESS BEHAVIOR OF HIGH STRENGTH ALLOYS

by

James Albert Van Den Avyle

Submitted to the Department of Metallurgy and Materials
Science on January 15, 1975 in partial fulfillment of the
requirements for the degree of Doctor of Philosophy.

Smooth bar tensile tests, plane strain tensile tests, and fracture toughness tests were performed on maraging 300 steel and 4340 steel. Eight strength levels of maraging 300 steel, ranging from 189 to 310 ksi (1300 to 2140 MPa) were produced by different ageing treatments; K_{IC} varied from ≈ 140 to < 40 ksi-in^{-1/2} (150 to 44 MN-m^{-3/2}). Strength and toughness of 4340 steel was varied by differing tempering treatments. Four strength and toughness conditions were tested between 176 and 222 ksi (1210 and 1530 MPa) and ≈ 130 and 63 ksi-in^{-1/2} (142 and 69 MN-m^{-3/2}). Fracture toughness tests were also conducted on high strength commercial aluminum alloys 2024-T4, 7075-T6 and 7475-T651.

Tensile properties such as yield strength, strain to fracture, and work hardening exponent determined from round bar and plane strain tests on the two steels did not correlate well with existing theories to predict K_{IC} . Ratios of plane strain yield stress to smooth bar yield stress fell between values predicted by the Tresca yield criteria (1.00) and the von Mises yield criteria (1.155). Strain hardening exponents (n) were essentially equal for the two tests at equivalent strength levels.

Fractography showed that plane strain crack propagation in the aluminum alloys 2024-T4 and 7075-T6 with high inclusion density (3 volume percent) was governed by growth and coalescence of large voids around large inclusions near the crack tip. Toughness of the cleaner 7475-T651 (1% inclusions) was improved as predicted by theory, but the fracture process was complicated by formation of extensive grain boundary delamination perpendicular to the crack plane in the plane strain region.

In the 4340 and maraging 300 steels with very low inclusion volume fraction, large inclusions did not control crack propagation, and fracture occurred by a process of zig-zagging or ridge formation above and below the macroscopic fracture plane. The spacing or wavelength of the ridges was typically small compared to plastic zone dimensions.

Studies of fracture surfaces and sectioned specimens showed that zig-zags propagate on $\pm 45^\circ$ paths with no void formation below the fracture surface. These observations agree with a combined theoretical stress-strain failure criterion predicting fracture along lines of high hydrostatic stress and high shear strain in a Prandtl slipline field.

The spacing λ of zig-zags was found to increase linearly but not proportionally with K_{IC}^2 , suggesting that the size of ridges was controlled by the intensity of the surrounding applied elastic stress field. The spacing was related to a critical strain for void formation along lines of localized shear strain described for low work hardening materials by the HRR crack tip singularity solution.

Void sizes on ridge sides and plane strain tensile specimen fracture surfaces did not vary significantly with changes of toughness. Nucleating particles for these voids are the small $0.2\mu\text{m}$ Ti(C,N) inclusions in maraging 300 steel and the 0.05 to $0.1\mu\text{m}$ Fe_3C carbides in 4340 steel. Ridge side voids were larger for maraging 300 steel than for 4340 steel, and the maraging steel has greater toughness at equivalent strength. This suggested that higher toughness may be achieved by controlling size and the bond strength of the small particles which provide for zig-zag formation.

Thesis Supervisor: Regis M. Pelloux
Associate Professor of Metallurgy

TABLE OF CONTENTS

<u>Chapter Number</u>		<u>Page Number</u>
	Title Page	1
	Abstract	2
	Table of Contents	4
	List of Illustrations and Figures	7
	List of Tables	12
	Acknowledgements	13
I	INTRODUCTION	14
II	LITERATURE REVIEW	18
	2.1 Inclusions and ductile fracture	18
	2.2 Crack tip solutions for stress and strain	20
	2.3 Crack tip failure criteria and relation of mechanical properties to K_{IC}	29
	2.4 Relation of second phase particles to K_{IC}	35
	2.5 Background of previous zig-zag observations	37
	2.6 Theories for zig-zag formation	39
III	EXPERIMENTAL	47
	3.1 Materials	47
	3.1.1 4340 steel	47
	3.1.2 Maraging 300 steel	54
	3.1.3 Commercial aluminum alloys - 2024, 7075, 7475	58

<u>Chapter Number</u>		<u>Page Number</u>
3.2	Mechanical testing	60
3.2.1	Axisymmetric tensile testing	60
3.2.2	Plane-strain tensile testing of 4340 and maraging 300	63
3.2.3	Fracture toughness testing	67
3.2.4	Charpy impact testing	70
3.3	Specimen preparation for the scanning electron microscope (SEM)	70
IV	RESULTS	72
4.1	Distribution of inclusions	72
4.2	Axisymmetric tensile test results	74
4.3	Plane-strain tensile test results	80
4.4	Fracture toughness test results	86
4.5	Fractographic observations and measurements	90
4.5.1	Ridge spacing on 4340 and maraging 300 steels	90
4.5.2	Details of ridge shape from sectioned profiles and SEM observations	100
4.5.3	Void sizes on ridge sides and on plane strain tensile specimens	109
4.5.4	Ridges on 4340 notched tensile specimens	117
4.5.5	Fracture Surfaces of 4340 Charpy Impact specimens	120
4.5.6	Fracture surfaces of the aluminum alloys	120

<u>Chapter Number</u>		<u>Page Number</u>
	4.5.7 Shear lip measurements on toughness specimens	124
V	DISCUSSION	128
	5.1 Relation of tensile properties to fracture toughness	128
	5.2 Crack propagation and fracture toughness	130
	5.2.1 Role of large inclusions in crack propagation	135
	5.2.2 Delamination in aluminum alloys	138
	5.2.3 Crack initiation and propaga- tion by zig-zagging	140
VI	CONCLUSIONS	154
VII	SUGGESTIONS FOR FUTURE WORK	156
VIII	BIBLIOGRAPHY	158
	Biographical Note	165

LIST OF ILLUSTRATIONS AND FIGURES

<u>Figure Number</u>		<u>Page Number</u>
1	Approximate plastic zone (a) and slipline field (b) for Mode I plane strain crack. (after Rice ⁽¹⁹⁾).	21
2	Stress distribution in slipline field around plane strain Mode I crack (from Rice and Johnson ⁽³⁾).	22
3	Stress in y direction ahead of sharp crack tip for (a) non-hardening solution and for (b) three values of work hardening exponent. (from Rice and Johnson ⁽³⁾).	25
4	Slipline flow fields for possible crack tip blunting geometries (a) circular tip, (b) 120° tip (c) flat tip.	27
5	Stress distribution due to crack tip blunting for several strength levels (σ_y/E) and hardening exponents. (from Rice and Johnson ⁽³⁾).	28
6	Localized shear bands in "cheezy" material of plastic zone prior to zig-zag burst. (after Berg ⁽³²⁾).	41
7	Banding in 4340 steel. (Tempered 427°C for 1 hr, etched 3% nital, 10 sec.).	52
8	Martensite laths in 4340 steel. (Tempered 510°C for 1 hr, etched 3% nital, 10 sec.).	52
9	Large inclusions in (a) 4340 steel and (b) maraging 300 steel (unetched).	53
10	Martensite lath structure of maraging 300 steel. (aged 427°C for 1 hr, etched 12% nital, 75 sec.).	57
11	Inclusions in 2024-T4 aluminum (unetched).	57
12	Inclusions in 7075-T6 aluminum (unetched).	61

<u>Figure Number</u>		<u>Page Number</u>
13	Inclusions in 7475-T651 aluminum (unetched).	61
14	Plane strain tensile specimen. Dimensions are in centimeters.	64
15	Compact tension fracture toughness specimen. Dimensions are in centimeters.	68
16	Standard size charpy impact specimen. Dimensions are in millimeters.	68
17	Log σ <u>versus</u> log ϵ_p for 4340 steel axisymmetric tensile tests.	77
18	Log σ <u>versus</u> log ϵ_p for maraging 300 steel axisymmetric tensile tests.	79
19	Log σ <u>versus</u> log ϵ_p for 4340 steel plane strain tensile tests.	82
20	Log σ <u>versus</u> log ϵ_p for maraging 300 steel plane strain tensile tests.	83
21	Yield stress <u>versus</u> K_{IC} for 4340 and maraging 300 steels.	89
22	Ridges on plane strain region of fracture toughness specimen of 4340 steel ($K_{IC} \approx 130$ ksi-in ^{1/2} /142 MN-m ^{3/2} , $\lambda = 60 \pm 5 \mu\text{m}$). Tilted 20°.	91
23	Ridges on plane strain region of fracture toughness specimen of maraging 300 steel ($K_{IC} \approx 140$ ksi-in ^{1/2} /153 MN-m ^{3/2} , $\lambda = 126 \pm 20 \mu\text{m}$): (a) ridges and (b) higher magnification view of fatigue-fast fracture transition. Both tilted 25°.	93
24	Curvature of ridges which become tangential to shear lip on fracture toughness specimen of 4340 steel: (a) overall view and (b) higher magnification. Both tilted 20°.	95

<u>Figure Number</u>		<u>Page Number</u>
25	Increase of ridge wavelength with K_{IC} on 4340 steel fracture toughness specimens: (a) $K_{IC} = 70 \text{ ksi-in}^{1/2}/76 \text{ MN-m}^{-3/2}$, $\lambda = 27 \pm 4\mu\text{m}$; (b) $K_{IC} \approx 130 \text{ ksi-in}^{1/2}/142 \text{ MN-m}^{-3/2}$, $\lambda = 60 \pm 5\mu\text{m}$. Both tilted 45° .	96
26	Yield strength <u>versus</u> ridge wavelength (λ) for 4340 and maraging 300 steels.	98
27	Ridge wavelength (λ) <u>versus</u> calculated COD for 4340 and maraging 300 steels.	99
28	Ridge wavelength (λ) <u>versus</u> calculated r_p^x and r_p^y for 4340 and maraging 300 steels.	101
29	Ridge wavelength (λ) <u>versus</u> K_{IC}^2 for 4340 and maraging 300 steels.	102
30	Zig-zag profiles: (a) epoxy impregnated and wedged open fracture toughness specimen of 4340 steel ($K_{IC} \approx 130 \text{ ksi-in}^{1/2}/142 \text{ MN-m}^{-3/2}$, $\lambda = 60 \pm 5\mu\text{m}$), and (b) nickel plated fracture surface (etched) of fracture toughness specimen of 4340 steel ($K_{IC} = 98 \text{ ksi-in}^{1/2}/107 \text{ MN-m}^{-3/2}$, $\lambda = 41 \pm 4\mu\text{m}$). Propagation from right to left.	104
31	Sectioned tip of zig-zagging crack from wedged open 4340 steel fracture toughness specimen ($K_{IC} = 98 \text{ ksi-in}^{1/2}/107 \text{ MN-m}^{-3/2}$, $\lambda = 41 \pm 4\mu\text{m}$).	106
32	Sectioned profile of fatigue-fast fracture interface showing blunted crack tip. 4340 steel fracture toughness specimen ($K_{IC} = 98 \text{ ksi-in}^{1/2}/107 \text{ MN-m}^{-3/2}$, $\lambda = 41 \pm 4\mu\text{m}$).	108
33	Two ridges adjoining a valley on the plane strain region of a fracture toughness specimen of 4340 steel ($K_{IC} \approx 130 \text{ ksi-in}^{1/2}/142 \text{ MN-m}^{-3/2}$, $\lambda = 60 \pm 5\mu\text{m}$). Zero degree tilt.	110

<u>Figure Number</u>		<u>Page Number</u>
34	Several ridges on the plane strain region of a fracture toughness specimen of maraging 300 steel ($K_{IC} = 82 \text{ ksi-in}^{1/2}/89\text{MN-m}^{-3/2}$, $\lambda = 54 \pm 10 \mu\text{m}$). Zero degree tilt.	111
35	High magnification view of voids on the sides of ridges of fracture toughness specimens of 4340 steel: (a) $K_{IC} = 63 \text{ ksi-in}^{1/2}/69\text{MN-m}^{-3/2}$, $\lambda = 24 \pm 4 \mu\text{m}$; (b) $K_{IC} \approx 130 \text{ ksi-in}^{1/2}/142 \text{ MN-m}^{-3/2}$, $\lambda = 60 \pm 5 \mu\text{m}$.	112
36	High magnification view of voids on the sides of ridges of fracture toughness specimens of maraging 300 steel: (a) $K_{IC} < 40 \text{ ksi-in}^{1/2}/44 \text{ MN-m}^{-3/2}$, $\lambda = 34 \pm 10 \mu\text{m}$; (b) $K_{IC} \approx 140 \text{ ksi-in}^{1/2}/153\text{MN-m}^{-3/2}$, $\lambda = 126 \pm 20 \mu\text{m}$.	114
37	High magnification view of voids on the fracture surface of plane strain tensile specimens of 4340 steel: (a) tempered 270°C for 1 hr, $K_{IC} = 63 \text{ ksi-in}^{1/2}/69 \text{ MN-m}^{-3/2}$; (b) tempered 510°C for 1 hr, $K_{IC} \approx 130 \text{ ksi-in}^{1/2}/142 \text{ MN-m}^{-3/2}$. Zero degree tilt.	115
38	High magnification view of voids on the fracture surface of plane strain tensile specimens of maraging 300 steel: (a) aged 427°C for 1.5 hr; $K_{IC} = 121 \text{ ksi-in}^{1/2}/132 \text{ MN-m}^{-3/2}$; (b) aged 427°C for 8 hr, $K_{IC} = 62 \text{ ksi-in}^{1/2}/68 \text{ MN-m}^{-3/2}$. Zero degree tilt.	116
39	Ridges on fracture surfaces of 4340 steel notched tensile specimens: (a) tempered 510°C for 1 hr, $K_{IC} \approx 130 \text{ ksi-in}^{1/2}/142 \text{ MN-m}^{-3/2}$, $\lambda = 40 \pm 10 \mu\text{m}$; (b) tempered 427°C for 1 hr, $K_{IC} = 98 \text{ ksi-in}^{1/2}/107 \text{ MN-m}^{-3/2}$, $\lambda = 20 \pm 5 \mu\text{m}$.	118
40	Ridges on fracture surfaces of charpy impact specimens of 4340 steel. Crack propagation top to bottom. (a) tempered 316°C for 1 hr; (b) tempered 427°C for 1 hr. Both tilted 45° .	121

<u>Figure Number</u>		<u>Page Number</u>
41	Plane strain fracture surface of 2024-T4 aluminum fracture toughness specimen: (a) low magnification showing delamination parallel to crack propagation direction (bottom to top); (b) high magnification showing large number of large voids and associated inclusions. Zero degree tilt.	122
42	Plane strain surface of 7075-T6 aluminum fracture toughness specimen showing delaminations parallel to crack growth (bottom to top). Zero degree tilt.	123
43	Polished and etched section of plane strain fracture surface of 7475-T651 aluminum. Propagation perpendicular to page. (Keller's etch).	123
44	Shear lip widths (SL) <u>versus</u> plastic zone size, r_p^y and r_p^x , for 4340 and maraging 300 steels.	126
45	Shear lip widths (SL) <u>versus</u> ridge spacing (λ) for 4340 and maraging 300 steels.	127
46	On-scale schematic drawings of calculated plastic zones and crack opening displacements, zig-zags, and 2D large inclusion spacing for two toughness levels of 4340 steel: (a) $K_{IC} \approx 130 \text{ ksi-in}^{1/2} / 142 \text{ MN-m}^{-3/2}$; (b) $K_{IC} = 63 \text{ ksi-in}^{1/2} / 69 \text{ MN-m}^{-3/2}$.	131
47	On-scale schematic drawings of calculated plastic zones and crack opening displacements, zig-zags, and 2D large inclusion spacing for two toughness levels of maraging 300 steel: (a) $K_{IC} \approx 140 \text{ ksi-in}^{1/2} / 153 \text{ MN-m}^{-3/2}$; (b) $K_{IC} = 50 \text{ ksi-in}^{1/2} / 55 \text{ MN-m}^{-3/2}$.	132
48	On-scale schematic drawing of calculated plastic zones, calculated crack opening displacements, and 2D large inclusion spacings of (a) 7075-T6; (b) 7475-T651; (c) 2024-T4 aluminum alloys.	133

LIST OF TABLES

<u>Table Number</u>		<u>Page Number</u>
1	Composition of Electro-Slag Remelt AISI 4340 Steel	50
2	Composition of Maraging 300 Steel	50
3	Compositions of Commercial Aluminum Alloys	59
4	Inclusion Size, Spacing, and Volume Fraction	73
5	Axisymmetric Tensile Data	75
6	Plane Strain Tensile Data	84
7	Fracture Toughness Testing Results	87
8	Notched Tensile Test Properties of 4340 Steel	119

ACKNOWLEDGEMENTS

I wish to gratefully acknowledge several people who have contributed greatly toward making the past three years at M.I.T. both educational and enjoyable. Thanks...

-to my advisor and friend Prof. Regis Pelloux who has given me technical and professional guidance plus an appreciation for life in New England.

-to Ronnie Stoltz, Ron Selines and the other fellow students in our group who have helped with their technical discussions and experimental assistance.

-to my wife, Carol, who has constantly encouraged me throughout the past six years as I have been in and out of graduate school. Her help with typing and preparing this manuscript is especially appreciated.

-to Sandia Laboratories for their financial support during the past two years under their Doctoral Studies Program.

CHAPTER I: INTRODUCTION

With the recent trend toward using the fracture mechanics approach to design structures and components, it has become increasingly important to understand the processes of crack initiation and propagation which control fracture toughness. The fracture processes which occur in commercial high-strength alloys are of considerable interest because these alloys tend to decrease in toughness as the strength is increased. Hopefully an understanding of the micro mechanisms of fracture can lead to improved toughness through better alloy design.

The most common parameter used to express toughness is K_{IC} , the plane strain Mode I opening critical stress intensity factor which is derived from the analysis of Irwin⁽¹⁾ for the elastic stress distribution in front of a sharp crack. K_{IC} is measured by following the procedures adopted by the American Society for Testing and Materials in its Standard E399-72. Because K_{IC} measures the intensity of a linear-elastic stress field, a measurement of K_{IC} will be valid only if the relative size of the plastic zone compared to the specimen dimensions is minimized. However, for tough metals it is well known that the fracture process takes place within the plastic zone as ductile fracture by steps of void initiation, growth, and coalescence. Thus we are able to characterize a plastic stress and strain controlled phenomenon by the intensity of

the surrounding elastic stress field. Since the elastic strain distribution sets the limits for plastic deformation at the crack tip, this approach is generally successful for valid specimen geometries; but it would be more satisfying to be able to express a failure criterion based on the processes of plastic deformation and fracture occurring within the plastic zone. If this criterion were available, the metallurgist could relate the microstructural parameters to fracture toughness and could attempt to improve toughness while raising the tensile strength.

Crack propagation under ideal plane strain conditions occurs with low absorbed energy or toughness because thickness constraint limits plastic flow and sets up high triaxial stresses ahead of the crack tip. This causes a decrease in measured toughness as specimen thickness is increased and more ideal plane strain conditions are approached. Most analytical studies of crack tip conditions have been performed for plane strain loading since it can be treated as a two dimensional problem.

Fractographic observations provide direct evidence of the mechanisms of plastic deformation and fracture which occur during crack propagation. Most of the past fractography work has concentrated on measurements of the spacing of large voids which form around large inclusions in an attempt to relate the void spacing to a process zone size which would

control fracture toughness. In general the fractographic observations or measurements did not report or take into account the presence of periodic ridges parallel to the crack front. These ridges which are formed as the advancing crack "zig-zags" on a microscale above and below the macroscopic fracture plane were described first by Rogers⁽²⁾ in 1960 for OHFC copper. Since then they have been seen for a wide variety of other alloys.

Understanding the formation of these zig-zags which appear to be a unit step for crack propagation could explain the factors which control fracture toughness.

In this work we have made an attempt to:

- a) characterize and accurately describe the form and scale of the ridges.
- b) correlate their size to mechanical properties, plastic zone size, and fracture toughness.
- c) formulate a theory to explain their occurrence.

The fracture toughness of two different types of steels, maraging 300 and 4340 steels, was systematically varied by suitable heat treatments. The relationships between toughness, mechanical properties, and ridge formation were investigated. The role of large second phase inclusions in the fracture behavior of these steels and commercial high strength aluminum alloys was also studied.

Criteria for zig-zag crack propagation were derived from

a) near crack tip stress and strain conditions calculated by Rice and Johnson⁽³⁾ and b) a combined hydrostatic stress-shear strain failure criterion for fully plastic geometries proposed by McClintock⁽⁴⁾ and Carson⁽⁵⁾.

CHAPTER II: LITERATURE REVIEW

2.1 INCLUSIONS AND DUCTILE FRACTURE

Many observations⁽⁶⁻¹⁰⁾ have shown that ductile fracture in metals is controlled by the interaction of applied stress and strain fields with second phase particles or inclusions to form voids. The failure process occurs by the following sequence:

- 1) plastic straining in some region of the specimen
- 2) initiation of voids either by particle-matrix interface separation or cleavage of the particle
- 3) growth of the voids under continued straining and under a hydrostatic stress
- 4) coalescence of voids to form a crack, as in the center of an unnotched tensile specimen, or with the main crack front, as in a precracked specimen.

Fractographic observations^(7,9,11,12) and transmission electron microscope (TEM) studies^(8,9) show that voids nucleate on second phase particles which vary widely in size: inclusions ranging from tens of microns down to less than $0.1\mu\text{m}$ and precipitates less than $0.1\mu\text{m}$. Voids tend to nucleate first on larger inclusions at lower strains, and then form around smaller particles as straining increases between large voids^(7,8,9).

Roesch and Henry⁽¹²⁾ studied ductile fracture in maraging steels and found that there was a critical particle size for void nucleation below which voids do not form. They observed that overaging the alloy to grow large precipitates resulted in a marked decrease in void size on the fracture surface accompanied by a lower fracture toughness as measured by impact testing. For their alloys, critical particle size vary from 200\AA to 1000\AA ($0.02\mu\text{m}$ to $0.1\mu\text{m}$), depending on particle shape and the nature of the particle-matrix interface.

Analytical continuum mechanics solutions for void growth and coalescence, as a function of applied stress and strain, are very complicated and difficult to model. Simplified two-dimensional treatments have been presented by McClintock⁽¹³⁾ et al, McClintock^(14,15), Thomason⁽¹⁶⁾, and Broek⁽⁹⁾. A three-dimensional treatment of isolated spherical void growth was given by Rice and Tracey⁽¹⁷⁾. These analysis, particularly McClintock's⁽¹⁵⁾, show the strong effect of high hydrostatic stress toward increased hole growth. Many factors such as hole-to-hole interactions, work hardening, distributions of void size and shapes, nucleation of new voids, and three-dimensional flow must be considered in future analyses to provide solutions which can be used to predict behavior of real materials.

2.2 CRACK TIP SOLUTIONS FOR STRESS AND STRAIN

Even when more sophisticated analytic methods for void growth become available, it will be necessary to incorporate these solutions into the stress and strain distribution at crack tips in order to describe crack initiation and growth. These analytic methods have undergone continual refinement. Currently, elastic stress solutions are known for a large number of geometries of cracked specimens⁽¹⁸⁾, and the slip line field solutions have been worked out for several geometries of plane strain fully plastic specimens⁽⁵⁾ of non-hardening material. The elastic-plastic cases of contained plasticity are more difficult since these solutions depend on the work hardening and strain-history characteristics of the metal.

The plastic zone at the tip of a Mode I crack in plane strain is shown schematically in Figure 1a; an approximate slip line flow field for this contained yielding in a non-hardening material which was suggested by Rice⁽¹⁹⁾ is given in Figure 1b. Figure 2, taken from Rice and Johnson⁽³⁾, shows this field to be made up of two constant stress regions A and B within 45° wedges ahead and behind the tip.

Throughout region B ahead of the crack, the tensile stress is 2.57 times the tensile yield stress. A centered fan, region C, has radial lines as principal shear directions, and the strain increases as $1/r$ approaching the tip within C.

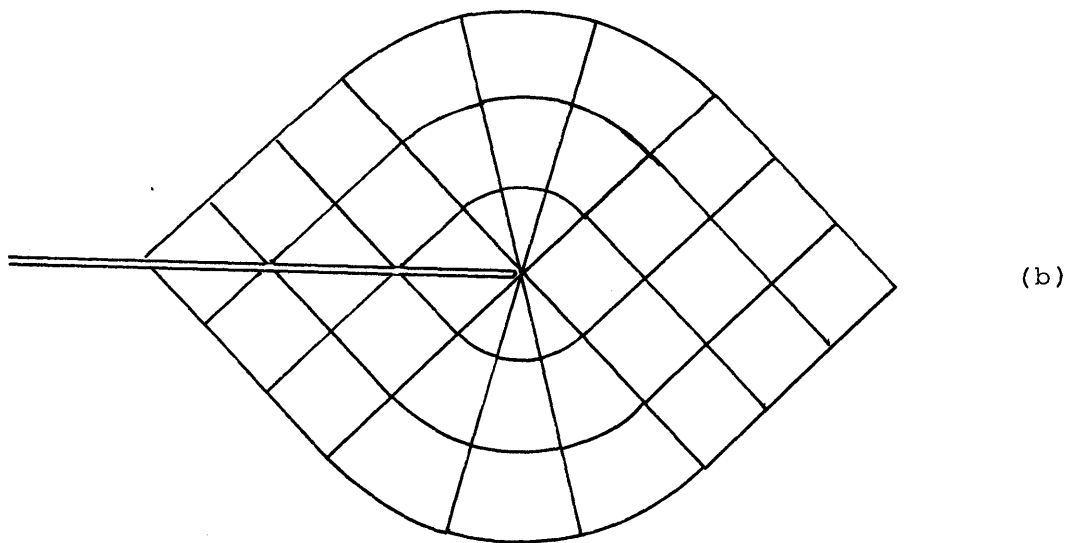
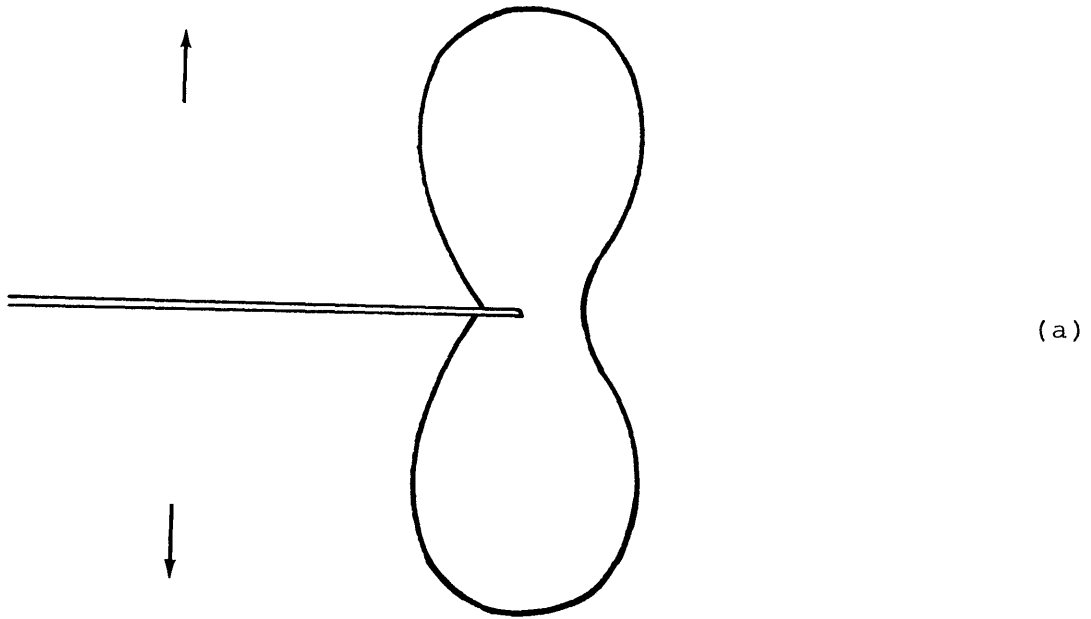


Figure 1 Approximate plastic zone (a) and slipline field (b) for Mode I plane strain crack. (after Rice⁽¹⁹⁾).

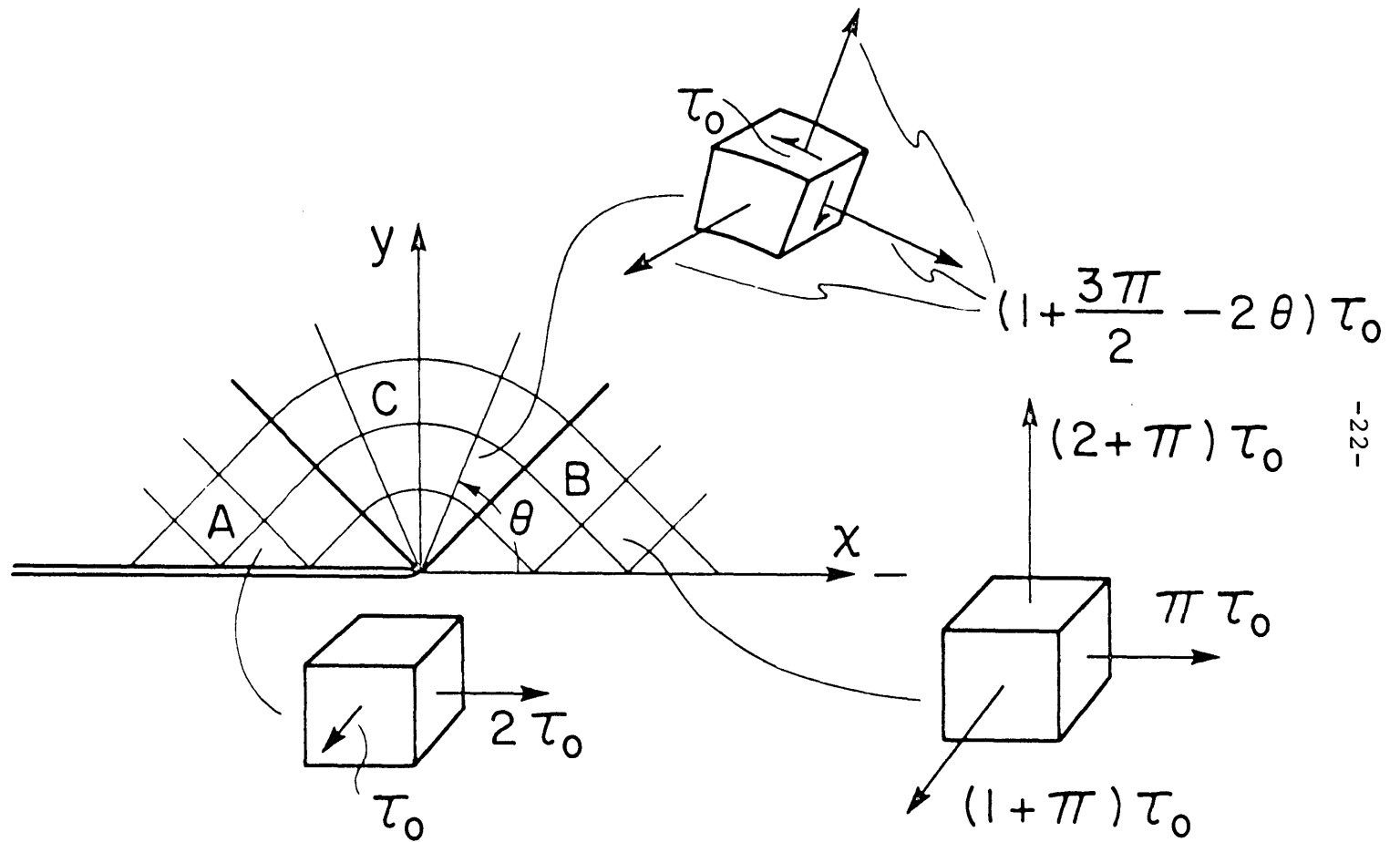


Figure 2 Stress distribution in slipline field around plane strain Mode I crack (from Rice and Johnson⁽³⁾).

No intense strain concentration is predicted directly in front of the crack in B, but the strains above and below the tip result in a crack tip opening.

Calculation of the plastic zone size and crack tip opening displacement have undergone continual refinement as summarized by Rice and Johnson⁽³⁾. The most accurate solutions reported by Rice are based on a finite element analysis by Levy⁽²⁰⁾.

Rice's values are:

maximum extent of plastic zone:

$$r_p^y = 0.175 \left(\frac{K}{\sigma_y} \right)^2, \text{ at } \theta = 70^\circ \quad \text{Eq. 1}$$

extent of plastic zone ahead of tip:

$$r_p^x = 0.032 \left(\frac{K}{\sigma_y} \right)^2 \quad \text{Eq. 2}$$

crack opening displacement:

$$\text{COD} = 0.5 \frac{K^2}{\sigma_y E} \quad \text{Eq. 3}$$

K is the applied stress intensity factor, and σ_y is the material yield strength. These expressions will be used for calculations throughout this thesis.

Rice and Johnson⁽³⁾ calculated the stress distribution directly in front of the crack for the sharp crack case of Figure I. The non-hardening solution (taken from their paper), is given in Figure 3a. Stress in the y direction normalized by the yield stress is the ordinate; distance in front of the tip normalized by $(K/\sigma_y)^2$ is the abscissa. Tick marks on the x axis are (left to right) the extent of the plastic zone directly in front of the crack and the maximum extent of the plastic zone at $\theta = 70^\circ$.

Figure 3b shows Rice's solution for a material which obeys a power hardening law of the type:

$$\tau = \tau_0 (\gamma/\gamma_0)^N \quad \text{Eq. 4}$$

where τ_0 and γ_0 are the shear stress and strain at yield. Note the expanded distance scale of Figure 3b. Very large stresses which increase with strain hardening are predicted to occur near the tip. Stresses decrease to the non-hardening solution at distances approximately two-thirds the extent of the plastic zone in front of the tip. This model predicts large stress gradients in front of a sharp crack tip.

The slip line flow field of Figure 1 for a sharp crack predicts no strain concentration directly ahead of the tip, yet large local strains should be necessary for void growth. This was recognized by Rice and Johnson⁽³⁾ and McClintock⁽⁴⁾

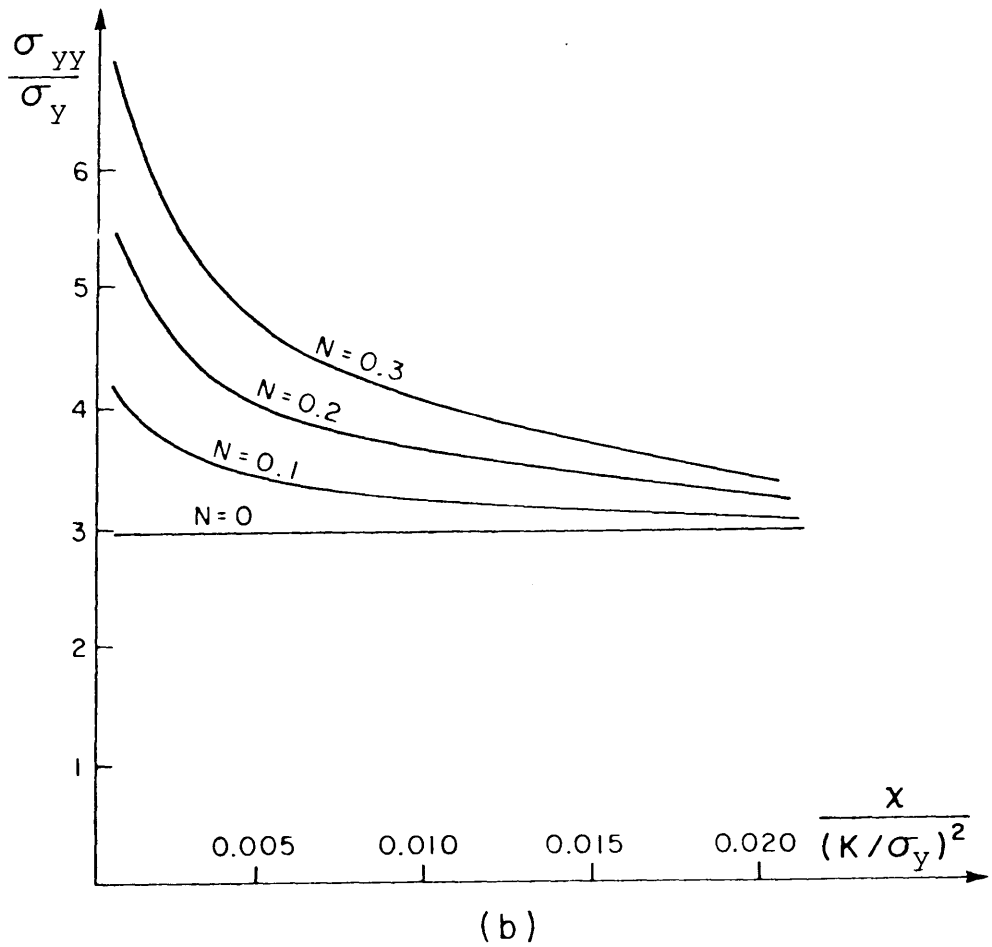
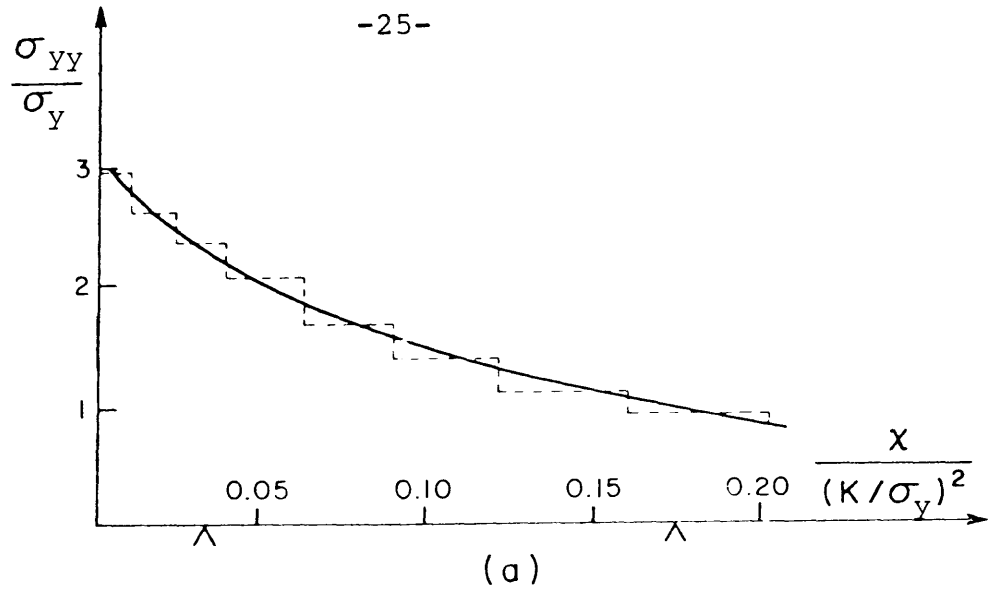


Figure 3 Stress in y direction ahead of sharp crack tip for (a) non-hardening solution and for (b) three values of work hardening exponent. (from Rice and Johnson⁽³⁾).

who proposed that crack tip blunting could account for the needed strain. Many blunted tip shapes are possible; slip line fields for rounded, angular, and flat tips are shown in Figure 4a-4c. These fields are greatly magnified versions of the near tip conditions of Figure 1. In Figure 4a regions A and B correspond to the constant stress regions of Figure 1. The high strain fan region C focuses large strains into the logarithmic spiral region D. It is within this region that void growth is proposed^(3,4) to occur. The other tip shapes also have similar high strain areas ahead of the crack tip. The extent of these regions is approximately twice the COD.

Rice and Johnson⁽³⁾ calculated the effect of crack tip blunting for a round tip on the stress distribution directly in front of the crack. This is shown in Figure 5 as a function of work hardening exponent and strength level. The calculations show that blunting changes the direction of the near tip stress gradient compared to the sharp crack tip predictions of Figure 3b. In general the stresses increase going away from the tip, reach a maximum at distances from 0.1 to 0.3 of the extent of the plastic zone, and decrease toward the non-hardening value. Blunting also smooths out stress gradients for high strength materials as shown by the curves for $\sigma_y/E = 0.0075$.

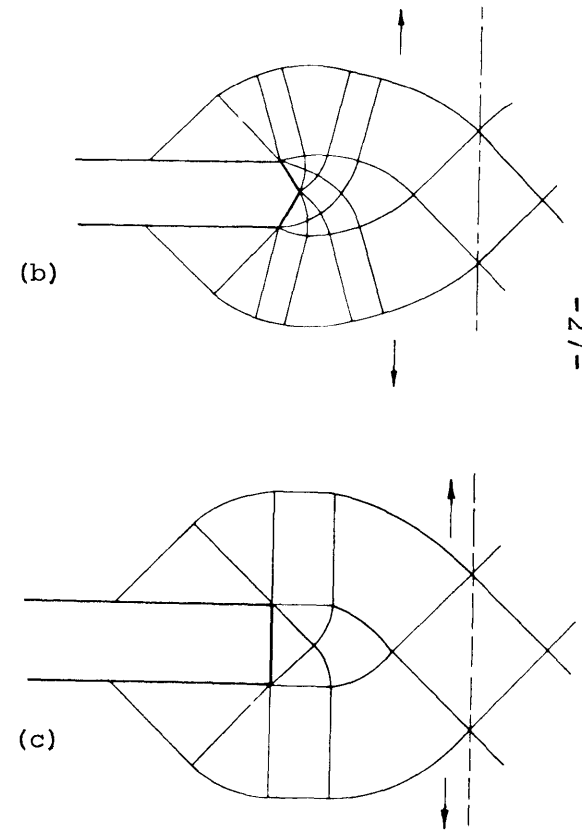
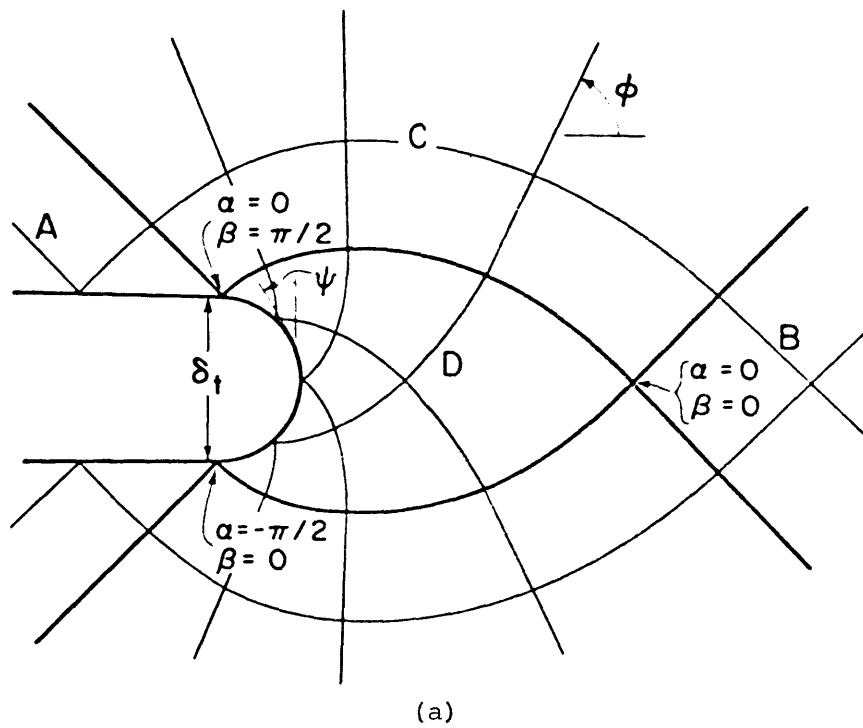


Figure 4 Slipline flow fields for possible crack tip blunting geometries
 (a) circular tip, (b) 120° tip (c) flat tip.

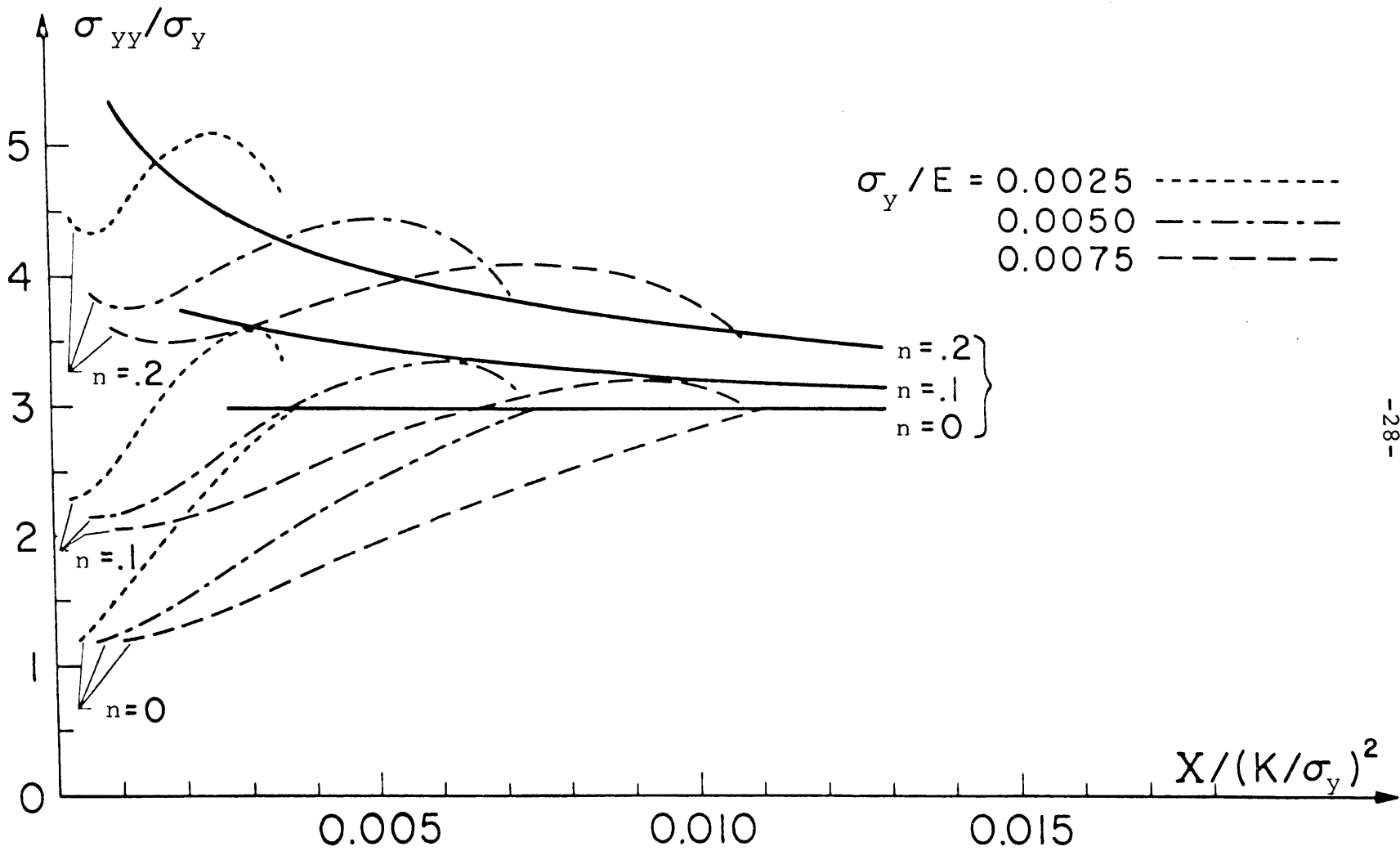


Figure 5 Stress distribution due to crack tip blunting for several strength levels (σ_y/E) and hardening exponents. (from Rice and Johnson⁽³⁾).

2.3 CRACK TIP FAILURE CRITERIA AND RELATION OF MECHANICAL PROPERTIES TO K_{IC} .

Several investigators have presented analyses which attempt to relate a crack tip fracture criteria to fracture toughness and measured tensile properties. The intention was to calculate K_{IC} rather than to conduct full scale tests which may be difficult because of specimen size requirements.

Krafft⁽²¹⁾ in 1963 was the first to propose that a critical strain must be reached over a distance which he called the "process zone size". He made the extraordinary assumption that the strain near the crack tip was given by the elastic strain distribution. This strain is given by:

$$\epsilon = \frac{K}{E\sqrt{2\pi d}} \quad \text{Eq. 5}$$

where d is distance from the crack tip. For a critical strain ϵ_t , over a distance d_t in front of a crack, to cause failure at K_{IC} , this becomes:

$$\epsilon_t = \frac{K_{IC}}{E\sqrt{2\pi d_t}} \quad \text{Eq. 6}$$

where d_t is the process zone size.

He next assumed that ϵ_t could be approximated by the plastic instability strain to necking. For a material which

obeys a power law hardening law of the type $\sigma = k\epsilon^n$, the necking instability strain is equal to the strain hardening exponent n . Substituting n for ϵ_t and rearranging gives Krafft's formula:

$$K_{IC} = E_n (2\pi d_t)^{\frac{1}{2}} \quad \text{Eq. 7}$$

This treatment is unsatisfying because:

- a) It is difficult to unambiguously define or to experimentally determine d_t .
- b) The assumed elastic strain expression is not valid within the plastic zone where fracture occurs.
- c) The use of the necking instability strain as a crack tip failure criterion is not justified since it is a measure of geometrical instability in a round bar tensile specimen and is not necessarily associated with fracture.

Hahn and Rosenfield^(22, 23) also use a critical strain in a plastic region ahead of the tip as a fracture criterion. The maximum fracture strain was taken as a function of the COD and λ (the width of an intensely strained region):

$$\epsilon_{\max} = \alpha \frac{\text{COD}}{\lambda} \quad \text{Eq. 8}$$

This is combined with a theoretical expression for COD

$$\text{COD} = \frac{1}{4} \frac{K^2}{\sigma_Y E} \quad \text{Eq. 9}$$

and the assumption that fracture takes place as the maximum strain equals one-third the true strain to fracture in a tensile test, ϵ_{true} .

The result is:

$$K_{\text{IC}} = \left[4\alpha\lambda\epsilon_{\text{true}} E\sigma_Y \right]^{\frac{1}{2}} \quad \text{Eq. 10}$$

Hahn and Rosenfield argue that $\alpha \approx \frac{1}{6}$ and empirically show that λ approximately equals n^2 (strain hardening exponent). Thus,

$$K_{\text{IC}} = \left[\frac{2}{3} \epsilon_{\text{true}} n^2 E\sigma_Y \right]^{\frac{1}{2}} \quad \text{Eq. 11}$$

Using this expression they predict K_{IC} for a variety of alloys within an accuracy of $\pm 30\%$.

This simplified analysis can be easily challenged from the same types of criticisms.

- a) The true strain to fracture in a tensile test reflects different hydrostatic stress and plastic strain conditions than would exist at the tip of a plane strain

crack. Also, the measured true strain is only an average overall strain, and it may or may not describe the localized strain distribution occurring within the necked region.

- b) The expression for maximum strain ϵ_{\max} is a very rough approximation. The plastic strain near the tip is a function of both angle and distance, as shown in Figures 2 and 4.
- c) The expression predicts that K_{IC} increases with σ_y , while the opposite is usually observed. Hahn argues⁽²⁴⁾ that a decrease in σ_y results in a relatively greater increase in n^2 , leading to higher K_{IC} , and he shows some data to support this conclusion. Whether this is generally true is not clear at this time.
- d) In their derivation they do not directly address the actual ductile fracture processes which occur ahead of the tip.

Rice⁽⁶⁰⁾ extended these ideas somewhat in a treatment which considered strength level (σ_y/E) and work hardening (n). His expression for process zone size is:

$$d_t = 0.49 \frac{K_{IC}^2}{E\sigma_y} \left[\frac{2(1+\nu)}{\sqrt{3}} \frac{\sigma_y}{E} \frac{1+n}{n} \right]^n \quad \text{Eq. 12}$$

or:

$$K_{IC} = \left\{ \frac{d_t E \sigma_y}{0.49} / \left[\frac{2(1+\nu)}{\sqrt{3}} \frac{\sigma_y}{E} \frac{1+n}{n} \right]^n \right\}^{\frac{1}{2}} \quad \text{Eq. 13}$$

which as the above models predicts K_{IC} proportional to $\sqrt{d_t}$.
Substitution Eq. 3 into Eq. 12 gives:

$$d_t = \text{COD} \left[\frac{2(1+\nu)}{\sqrt{3}} \frac{\sigma_y}{E} \frac{1+n}{n} \right]^n \quad \text{Eq. 14}$$

Thus the process zone size for this treatment is some fraction of the COD which is determined by work hardening and strength level.

Several investigators^(25,26,27) have proposed the use of the COD itself as a failure criterion. They rationalize that the COD, which opens to a size governed by the surrounding elastic material, also is a measure of the resulting plastic strain close to the tip. COD has been measured by a wide variety of techniques including impregnated plastic replicas⁽²³⁾, measurement of stretch zones on fractographs^(25, 26,27), and angle of bend measurements for three-point bend specimens⁽²⁵⁾. The general data follow the form:

$$\text{COD} = C \frac{K_{IC}^2}{\sigma_Y E} \quad \text{Eq. 15}$$

From a large number of experiments, Robinson and Tetelman⁽²⁵⁾ find that $C \approx 1$, while Broek⁽²⁶⁾ finds $C = .40$ (in agreement with Rice's⁽³⁾ analytical calculations). Further experimental work is needed to clarify these differences between theory and experiments.

The accuracy of calculated K_{IC} from fractographic measurements of COD is only on the order of $\pm 30\%$ ^(26,27) because of the irregularities of stretch zone features along the crack front. As emphasized by Broek⁽²⁶⁾, the depth of the stretch zone is a measure of the COD; and for accuracy, measurements should be made from stereo micrographs of matching stretch zones of both fracture surfaces.

Robinson and Tetelman⁽²⁵⁾ claim that the center region of sub-size specimens (too thin to satisfy ASTM requirements for valid K_{IC} testing) is in plane strain and can provide critical COD measurements which can be used to calculate a valid K_{IC} . If this result can be shown to be quite general it would provide a practical tool for simple measurements of K_{IC} .

Thus while the critical COD approach may prove a successful technique of measuring toughness, it is still not descriptive of the actual fracture processes which occur.

2.4 RELATION OF SECOND PHASE PARTICLES TO K_{IC}

There have been several attempts to relate the size of a process zone, such as d_t in Krafft's theory⁽²¹⁾ or in Hahn and Rosenfield's analysis⁽²²⁾ to the inclusion spacing(s). The assumption here is that crack extension occurs when the intensely strained process zone reaches a size comparable to the spacing of cracked inclusions. Generally only large (>1 μ m diameter) inclusions have been considered in these theories. At that critical strain level the void associated with the inclusion can coalesce with the main crack front, giving a small segment of crack advance. Krafft's expression thus becomes:

$$K_{IC} = [En \ 2\pi s]^{1/2} \quad \text{Eq. 16}$$

Hahn and Rosenfield⁽²⁸⁾ relate K_{IC} to inclusion spacing and volume fraction by assuming the COD to be approximately equal to s, giving

$$K_{IC} \approx [2\sigma_Y Es]^{1/2} \quad \text{Eq. 17}$$

For a cubic array of spherical particles

$$s = \left[\frac{\pi}{6} \right]^{1/3} D f^{-1/3} \quad \text{Eq. 18}$$

where D is particle diameter and f is volume fraction.

This gives

$$K_{IC} \approx \left\{ 2 \sigma_Y E \left[\frac{\pi}{6} \right]^{1/3} D \right\}^{1/2} f^{-1/6} \quad \text{Eq. 19}$$

Broek⁽⁹⁾ used a similar analysis based on Krafft's assumption of an elastic strain distribution. He predicts

$$K_{IC} = \alpha \sigma_Y f^{-1/7} s^{1/2} \quad \text{Eq. 20}$$

Hahn and Rosenfield⁽²⁸⁾ present a summary of data by other investigators which shows that toughness does vary approximately as $f^{-1/6}$ of large (>1 μ m) particles for several types of alloys of equivalent (σ_Y/E) strength level. This implies that large reductions in volume fraction of second phase is necessary to achieve significant improvement in K_{IC} .

Other data by Hahn and Rosenfield⁽²⁸⁾ for several aluminum alloys and by Cox and Low⁽²⁹⁾ for 4340 and 18Ni (200) maraging steels do not support the theory that spacing of large inclusions controls toughness. Low finds a significant difference in toughness between 4340 and maraging steels which have approximately equivalent yield strengths and inclusion spacings: Low suggests that the fracture processes which link up the voids around large inclusions in fact

control toughness.

The above theories do not deal well with changes in toughness caused by varying yield strength without varying inclusion distribution. This is done, for example, through ageing or tempering.

Also it is clear that if an alloy is made clean enough the interparticle spacing becomes much larger than any high strain intensity region ahead of the crack tip. In this case the crack would only rarely interact with a large inclusion, and ductile fracture would be controlled by different processes. With this in mind, we will consider past work on fracture by zig-zagging.

2.5 BACKGROUND OF PREVIOUS ZIG-ZAG OBSERVATIONS

Periodic ridge markings have been observed in a large number of alloy systems and specimen configurations. The first to report them was Rogers⁽²⁾ in tensile specimens of OFHC copper. The ridges were formed as circumferential rings within the "flat" plane-strain region in the center of the specimen; they were visible in the optical microscope and also on polished longitudinal sections of the fracture surface. Carr, et al⁽³¹⁾ also reported circumferential ridges on round-bar tensile specimens of several steels. Zig-zag fracture surfaces have also been seen in plane-strain areas of Charpy impact specimens, dynamic-tear-energy

specimens, and fracture toughness specimens (both compact tension and three point bending) (32,33,34). Alloy systems where these have been seen include OFHC copper, 200 grade maraging steels (33,34), 4340 steels (37), martensitic stainless steels (33), titanium, aluminum, and cobalt series alloys (5), and 0.6% C, 5.0% Ni, 0.08% Mn steels (32). Measured spacings range from 10 μm (32) to 800 μm (33). The features which are common to all these observations are:

- 1) fracture by microvoid initiation, growth, and coalescence on the ridges
- 2) a high degree of triaxiality ahead of the crack tip
- 3) plane-strain conditions ahead of the crack tip.

This state is due to thickness constraint in fracture toughness specimens and occurs ahead of the internal crack initiated in the center of a necked round tensile specimen.

- 4) moderate to high fracture toughness of the alloy

While most tensile tests, DTE, and fracture toughness tests which show zig-zagging were conducted in air and were overload failures, some environments were shown by Yoder (33) and Beachem and Yoder (34) to cause slow crack propagation and ridge formation at stress intensities below K_{IC} . Ridges were produced by stress corrosion cracking a precipitation hardened stainless steel (13 Cr, 8 Ni, 2 Mo) in 3-1/2 pct

NaCl solution loaded to a stress intensity between K_{IC} and K_{ISCC} and cathodically charged at -1.5v vs SCE by coupling to a magnesium anode. Thus it appears that factors present in the environment, possibly hydrogen, may enhance this form of failure at high stress intensities.

2.6 THEORIES FOR ZIG-ZAG FORMATION

Several authors have modeled conditions ahead of the crack tip and proposed to account for zig-zag formation. Rogers (1960)⁽²⁾ etched longitudinal sections and showed regions of concentrated shear strain below the crack surface ahead of a downward crack extension from which an upward extension had occurred. He proposed that changes in crack direction occurred as the crack alternated between $\pm 45^\circ$ paths of maximum shear strain. He did not develop these simplified notions any further.

Berg (1969)⁽³²⁾ presented data by R. Broek on the spacing (wavelength) of ridges for two strength levels of 0.6% C - 5% Ni - 0.08% Mn steel and showed that the wavelength was on the order of one quarter to one third the extent of the plastic zone directly in front of the crack (calculated as $0.032 (K_{IC}/\sigma_y)^2$). The limited data showed that wavelength increased with K_{IC} . He also noted that there were from 5 - 10 dimples along each ridge hillside. Berg recognized that the small ratio of the void spacing to the plastic zone size

indicated that any analytical solution to the ductile fracture problem had to involve a fully plastic stress and strain analysis.

Berg proposed that the material within the plastic zone ahead of the crack tip would contain a large number of microvoids nucleated by the high triaxial stress acting on inclusions. He calculated the effect of this porosity on the yield locus and concluded that incipient banding zones of high localized shear strain should form within the plastic zone (Figure 6). These bands would be inclined at an angle to the macroscopic fracture plane and would contain a large number of voids. From his model he concluded that crack propagation occurred as bursts across the plastic zone when the surfaces of the incipient bands separate to give a zig-zag fracture surface. Factors which control the wavelength of the ridges would include the microvoid density ahead of the crack tip (a function of particle size and spacing) and the strain hardening rate of the porous material.

Berg presents no real experimental evidence to support his idea of zig-zags of microporous, high strain bands built up ahead of the crack tip. Polished and etched cross-sections of precracked specimens should show these bands ahead of a crack tip. At this time there is no evidence for this behavior, and most experimental observations suggest that crack ing occurs in a more or less continuous path, with only a few

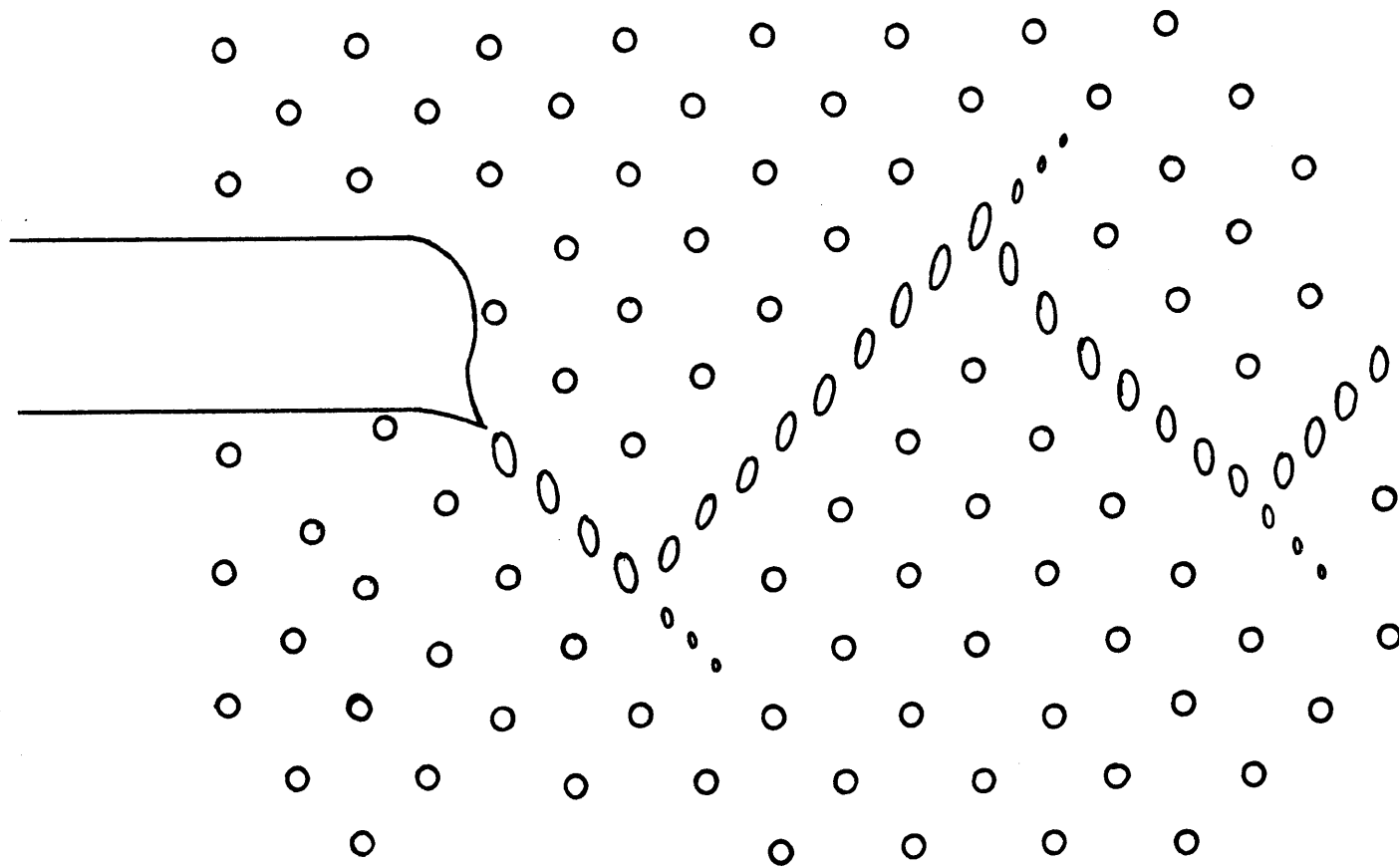


Figure 6 Localized shear bands in "cheezy" material of plastic zone prior to zig-zag burst.
(after Berg⁽³²⁾).

voids opening up ahead of the crack tip along the ridge sides.

In 1969 McClintock⁽⁴⁾ also noted that fracture in high strength metals does not occur by sheets of holes growing gradually directly in front of the crack, as he had assumed in his simplified model for hole growth in the plastic zone. He then suggested that the crack propagates at angles $\pm 45^\circ$ to the macroscopic fracture surface in a combination of Mode I (tension) and Mode II (shear). At these angles for a sharp crack tip (Figure 1) the zig-zag crack path lies on the boundary between the high shear strain fan region and the diamond-shaped region of constant high triaxiality directly in front of the crack. McClintock in effect proposed a combined triaxial stress-critical shear strain failure criteria for hole growth leading to zig-zag crack propagation. He did not consider the size and scale of the zig-zag spacing and its relation to possible crack tip blunting.

In an attempt to model zig-zag crack propagation in an elastic-plastic metal, Carson⁽⁵⁾ carried out two analysis which bracket known behavior. The first analysis was an attempt to verify McClintock's theory of a combined triaxial stress-critical shear strain criterion. He developed slip line field patterns for several assymmetrically notched fully plastic plane strain tensile specimens. He predicted that the crack path would follow border lines between high triaxiality regions and high shear strain regions. His predic-

tions work quite well for 2024-0 aluminum which has a rather high, uniform density of large inclusions which nucleate voids. They were not successful for 1100-0 aluminum and C1117 steel; fracture paths in these two alloys could be rationalized by the presence of a low inclusion density in 1100-0 aluminum and by anisotropic stringers of inclusions in the C1117 steel rather than by the slip line field analysis.

Carson also determined slip line fields for several geometries of zig-zagged (dog-leg) cracks which were under combined Mode I - Mode II loading. From these fields, using again the critical stress-strain criteria of McClintock, he was able to predict that the crack would change directions and propagate along alternating shear planes. Unfortunately in this analysis he assumed a plastic zone size much smaller than the length of a ridge side. Berg⁽³²⁾ showed just the opposite to be true, so the applicability of this part of Carson's analysis is doubtful.

Yoder⁽³³⁾ described the general fractographic features of the ridges and related ridge spacing to the tensile mechanical properties of 18 Ni (200) maraging steel.

He showed:

- 1) The lines across the fracture surface of fracture toughness specimens trace successive positions of the moving crack front. The lines were not continuous across the surface but had a length to width

of the order of 10.

- 2) For a given ageing (toughness) condition in a 18 Ni (200) maraging steel the ridge spacings seem to be constant for Dynamic Tear Energy (DTE), K_{IC} three-point bending, and Charpy specimens.
- 3) For the same toughness level, line spacings formed in round-bar tensile specimens were approximately 30% less than for the DTE specimen of the same toughness. Yoder attributed this to a difference in constraint to plastic flow.
- 4) By observing matching specimen halves in the SEM, the ridges were shown to be complimentary (ridges match with valleys).
- 5) The line spacing was shown to increase, as suggested by Berg⁽³²⁾ with increasing toughness. Toughness was measured with Dynamic Tear Energy Tests (DTE) and not by valid plane strain fracture toughness tests because the alloy studied was quite tough ($K_{IC} > 100 \text{ MN-m}^{-3/2}$), and the thickness criteria could not easily be satisfied.

To relate the line spacing, λ , to K_{IC} , Yoder proposed the use of Krafft's^(21,35) tensile ligament instability theory. He equated λ to d_t , Krafft's process zone size (see Eq. 7) and arrived at Equation 21.

$$K_{IC} = n_{TIS} E\sqrt{2\pi\lambda} \quad \text{Eq. 21}$$

Yoder used measured values of n_{TIS} and λ to calculate K_{IC} for different toughness conditions. His only valid K_{IC} datum point is approximately 50% greater than the calculated value. The plots of calculated K_{IC} versus DTE give a linear relation, which is often found for valid K_{IC} versus DTE data. Thus while the linear relationship with DTE gives some support to the Yoder-Krafft model, the applicability of the Krafft treatment, and its inherent assumptions, seems questionable as previously discussed. It is difficult to visualize the propagation of the zig-zagging crack as a series of local necking events when hole growth seems mostly dependent on a localized shearing action. In any case, the relationship between K_{IC} , λ , and other mechanical properties is of practical importance, and some further experimental results will be presented later.

The most recent published work on zig-zag fracture by Beachem and Yoder⁽³⁴⁾ reports detailed fractographic observations of this mode of crack growth in hydrogen assisted cracking (HAC) of a specimen of 13CR-8Ni-2Mo steel. Several of their observations are:

- 1) Peaks of ridges are sharp, while the matching valleys are stretched out.
- 2) The mode of failure along the ridges is mixed as indicated by counting the types of dimples. About 55% were tear dimples, 30% were shear, and 15% were equiaxed. This implies that tearing (Mode I) type deformation is predominant at the peak of the ridge.
- 3) The slopes of the ridge sides facing the crack origin are less steep than the sides facing away from the origin ($36 \pm 10^\circ$ vs $52 \pm 9^\circ$).
- 4) The cracking process was seen as occurring in four steps:
 - a) cracking along a first shear plane,
 - b) a forward tearing step,
 - c) cracking along the second shear plane, and
 - d) a second forward tearing.

To account for the crack changing direction, Beachem and Yoder propose a very simplistic theory relating the state of stress near the crack tip and the orientation and length of the dog leg. In general their observations support the idea that propagation of zig-zag cracks involves a combination of Mode I and Mode II fracture by tearing and shearing along localized planes of high shear strain within the plastic zone.

CHAPTER III: EXPERIMENTAL

3.1 MATERIALS

3.1.1 4340 STEEL

AISI 4340 steel is a medium-carbon (0.40%C) high-strength martensitic steel which has been widely used for many years. In the as-quenched condition it is very brittle, so for most applications it is given a tempering treatment which greatly improves its fracture toughness. The yield and tensile strengths, however, decrease with increased tempering and toughness. To obtain the variation in toughness desired in this study, specimens were tempered for one hour at temperatures between 260°C and 538°C.

In the as-quenched condition the martensitic structure consists of fine laths ($2000 \sim 5000 \text{Å}$)^(36,37,38) which contain a very fine high density of dislocations and some microtwins⁽³⁷⁾. Carbon occupies tetrahedral sites in the iron lattice, giving a tetragonal structure. Since an oil quench is generally used to retard quench cracking, it is probable that some tempering occurs during the relatively slow cool-down, a process called autotempering. This could take the form of carbon migration to dislocations⁽³⁶⁾, or if cooling is slow enough, epsilon (ϵ) carbides or cementite (Fe_3C) could precipitate.

The processes of tempering involve at least three stages⁽³⁹⁾ which depend on tempering temperature. The first stage is the formation of metastable coherent ϵ carbide below 200°C. The matrix remains martensitic, but the solid solution carbon content decreases to about 0.30 percent. The second stage for some steels is the decomposition of retained austenite to bainite, occurring between 100°C and 300°C. This step is not significant for 4340 since very little austenite is retained after quenching.

The third stage of tempering, which produces the greatest decrease in strength and increase in toughness^(37,40), occurs between approximately 300°C and the eutectoid temperature. In this stage the ϵ carbides dissolve, and the lower carbon tetragonal martensite loses its carbon and becomes ferrite with a cubic structure. The carbon diffuses to form the stable precipitate Fe_3C , and this results in lowered strength. Concurrent with the carbide coarsening is recovery of the dislocation structure; cell formation occurs at higher tempering temperatures (above 538°C)⁽³⁷⁾.

Transmission electron microscopy (TEM) studies of 4340 show that Fe_3C forms at lath boundaries⁽³⁸⁾, microtwin boundaries, and dislocation nodes⁽³⁷⁾. They tend to be plate-shaped at lower tempering temperatures and begin to coalesce into spheroids above 482°C. Extraction replicas and TEM observations show that for tempering below 538°C the average

platelet dimensions are less than $0.1\mu\text{m}$ thick by $0.2\mu\text{m}$ long⁽³⁷⁾. These observations are qualitative, and there is no detailed quantitative data relating size, spacing, and volume fraction of Fe_3C as a function of tempering temperatures.

The 4340 steel used in this study was produced by the Lukens Steel Co. using the electro-slag remelt process. This results in very low impurity levels, particularly sulphur and phosphorus, as shown in Table 1. The 1.5% nickel addition is made to improve hardenability in thick sections. The material was supplied as 3.8cm thick cross-rolled plate by the Army Materials and Mechanics Research Center, Watertown, Massachusetts.

Machined specimens were austenitized at 840°C for one hour in an 80% BaCl_2 -20% NaCl salt bath and oil quenched. Tempering at the various temperatures for one hour was performed in a 50% NaNO_3 -50% KNO_3 salt bath; temperatures were controlled at $\pm 5^\circ\text{C}$. The specimens were abraded with successive grades of SiC paper and given a final polish using Wenol brand metal polish. Surface decarburization which occurred during heat treatment was removed by this process, as confirmed by examination of polished and etched cross sections.

Samples were polished for optical microscopy using graded diamond polishing compounds (6,1, and $0.25\mu\text{m}$). Several microstructural features common to all tempering treatments were observed:

TABLE 1

COMPOSITION OF ELECTRO-SLAG REMELT AISI 4340

C	0.41	Si	0.23
Mn	0.76	Ni	1.60
P	0.003	Cr	0.73
S	0.003	Mo	0.28
		Fe	balance

TABLE 2

COMPOSITION OF MARAGING 300 STEEL

C	0.014	Ca	0.05
Ni	18.26	Al	0.09
Mo	4.81	Si	0.02
Co	8.82	Mn	0.05
Ti	0.66	S	0.004
B	0.004	P	0.005
Zr	0.010	Fe	balance

a) At low optical magnifications, banding (Figure 7) was seen on the LT and WT planes, while ellipsoidal regions of varying etching intensity were seen on the LW plane. These bands, which average 50 μ m thick, are due to alloying segregation retained from solidification and elongated by the rolling procedure.

b) Prior ausenite grain boundaries were revealed by electrolytic etching (9% perchloric acid, 45% acetic acid, 46% butylcellosolve, 5 $^{\circ}$ C, 30v). The grains are equiaxed with an average diameter of 10 μ m.

c) Fine lath martensite was visible at high optical magnifications of etched specimens (Figure 8). This morphology, as observed optically, did not change significantly with tempering treatment.

d) Two ranges of inclusion size were observed. Large grey inclusions with an ellipsoidal shape range in size from approximately 1 μ m to 30 μ m with an average size of approximately 5 μ m. These are shown in Figure 9a and have been identified as manganese sulfides (MnS)⁽²⁹⁾. More numerous sub-micron particles with an apparent size of approximately 0.2 to 0.3 μ m were also seen. The average spacings of both large and small inclusions were measured by counting the numbers of inclusions present in a known optical viewing area. Distribution of small inclusions were counted at 400 X magnification, and the number of large inclusions were counted at

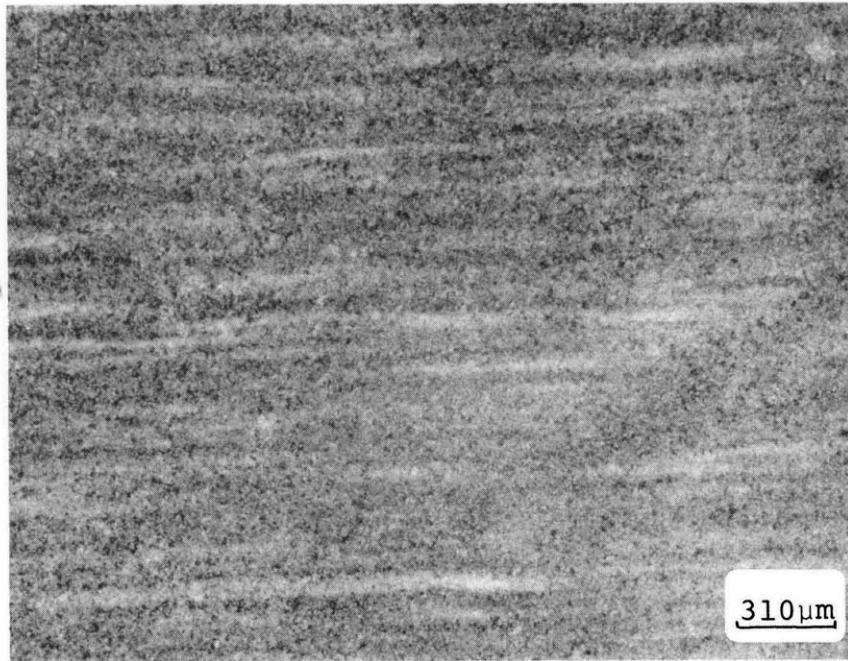


Figure 7 Banding in 4340 steel. (Tempered 427°C for 1 hr, etched 3% nital, 10 sec).

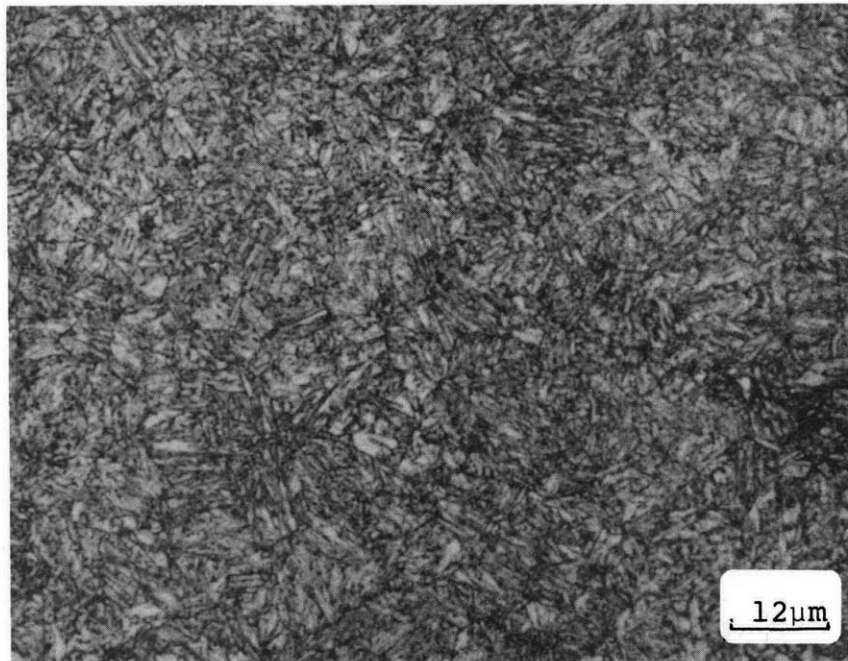
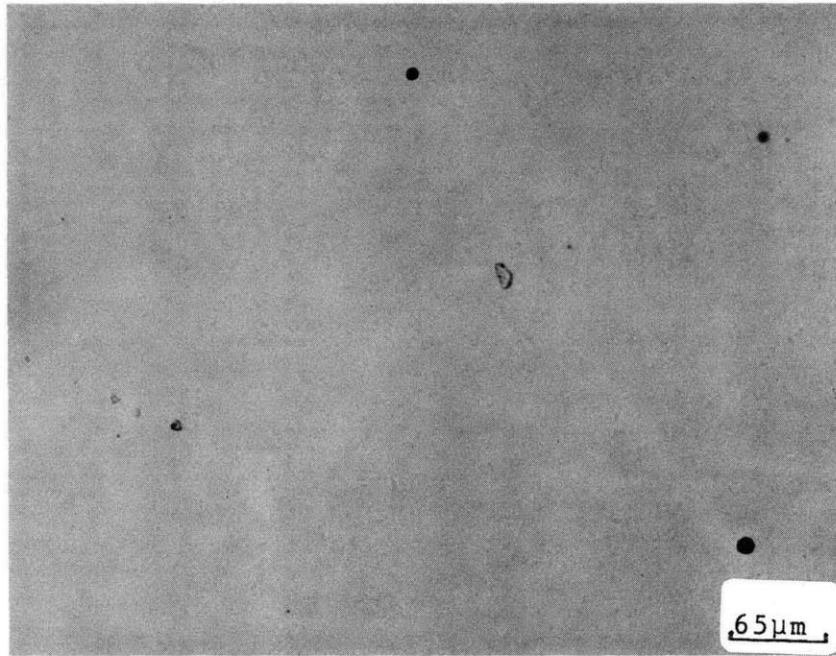
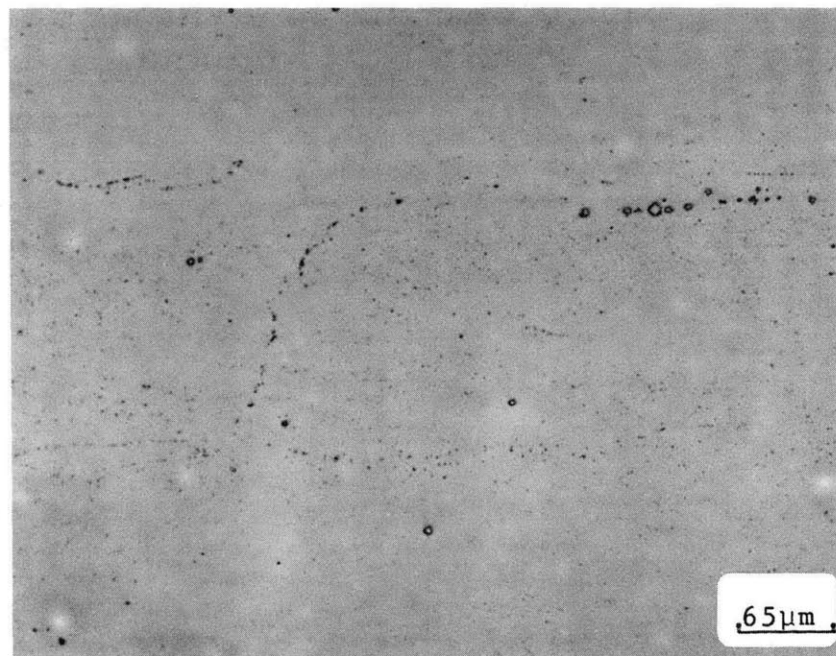


Figure 8 Martensite laths in 4340 steel. (Tempered 510°C for 1 hr, etched 3% nital, 10 sec).



(a)



(b)

T \blacktriangle

R \blacktriangledown

Figure 9 Large inclusions in (a) 4340 steel and (b) maraging 300 steel (unetched).

150 X. Ten to twenty fields of view were counted for each specimen. Using these two-dimensional planar spacings, approximate three dimensional spacings were calculated by assuming a uniform average size of particle⁽⁴¹⁾. Results of these measurements are given in Table 4 in Chapter 4.

3.1.2 MARAGING 300 STEEL

Maraging 300 Steel is one of a class of commercially available high alloy steels with very low carbon content which are strengthened by precipitation hardening in an iron-nickel martensite. The grade numbers (200, 250, 300) correspond to the strength levels in ksi which can be obtained by increasing the amounts of elements which contribute to precipitate formation; that is molybdenum, cobalt, and titanium⁽⁴²⁾.

The composition of the steel used in this study is listed in Table 2. It was supplied by Teledyne Vasco (consumable vacuum melted Vascomax 300) in the form of 10cm X 3.2cm bar.

The iron-nickel martensite transforms as a non-equilibrium structure during air cooling from a typical austenitizing-solutionizing anneal of one hour at 820°C^(43,44,45). The M_s temperatures for these grades of maraging steels are around 200°C⁽⁴⁶⁾. The martensite forms into a packet morphology with a bcc structure; packet martensite is made up of fine elongated laths, approximately 1 μ m thick with a high

dislocation density^(43,47,48). In the as-transformed condition, the alloys have a yield strength around 100 ksi⁽⁴⁹⁾, high toughness and ductility, and good machinability.

High strength in these alloys is due to the formation of age-hardening precipitates during ageing in the temperature range 400 - 500°C; the precipitates which form depend on the ageing time and temperature⁽⁵⁰⁾. The standard ageing treatment to develop full strength for maraging 300 is three hours at 480°C.

Uniformly distributed precipitates form around 400°C⁽⁵⁰⁾, while at higher temperatures they form on dislocations. Evidence indicates that Ni₃Mo is the main hardening precipitate when these alloys are aged for three hours at 480°C^(43, 51). They are rod shaped and 50 - 100Å in diameter. At higher ageing temperatures at longer times, precipitation of Fe₃Mo also occurs⁽⁵¹⁾.

It has been established^(43,50,52) that cobalt is not a precipitate constituent, but rather acts to lower the solubility of molybdenum in the iron-nickel matrix. This increases the amount of molybdenum available for precipitation.

Titanium acts as both a hardener and a getter for residual carbon and nitrogen. Identification of Ni₃Ti as a precipitate has been very difficult^(43,53) because of the structural similarity of Ni₃Mo and Ni₃Ti.

At ageing temperatures above 500°C, overageing occurs, and above 525°C austenite reversion is also significant.

To get combinations of strength and toughness for this study, machined specimens were aged at either 427°C, 483°C, or 538°C for times ranging between 1 and 100 hours. Ageing was performed in a 50% NaNO₃-50% KNO₃ salt bath with the temperature controlled to ±5°C. The specimen surfaces were abraded and polished by the same method as the 4340 specimens.

A micrograph of the alloy aged at 427°C for one hour is shown in Figure 10; angular martensite packets are well defined. Prior austenite grain size for this material is 50µm⁽⁵⁴⁾.

Three size ranges of inclusions can be resolved optically (Figure 9b). Large inclusions ranging in size from 1 to 15µm are Ti(C,N) and Ti₂S⁽³⁷⁾; an example of a rectangular Ti(C,N) inclusion (6 X 8µm) is seen in the center of Figure 10. Ti(C,N) inclusions are typically cubic in shape and appear yellow to pink in the optical microscope; they constitute a majority of the large inclusions. The Ti₂S particles are rounded and few in number. Both of these often lie in stringers along the rolling direction.

A second size range of inclusions is between approximately 0.5 to 1µm in size. These are easily seen on unetched polished surfaces in the optical microscope (Figure 9b) and appear to be randomly dispersed.

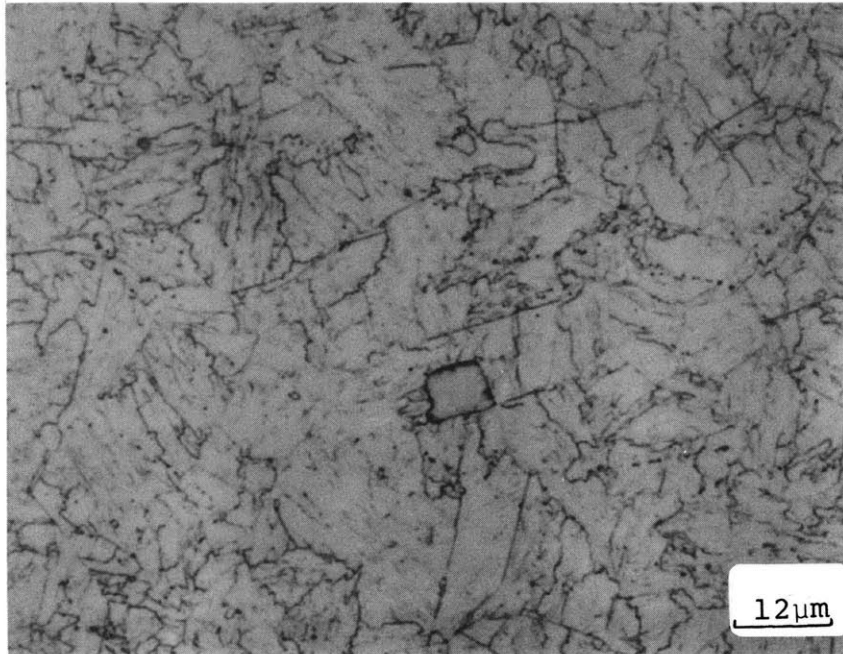


Figure 10 Martensite lath structure of maraging 300 steel. (Aged 427°C for 1 hr, etched 12% nital, 75 sec).

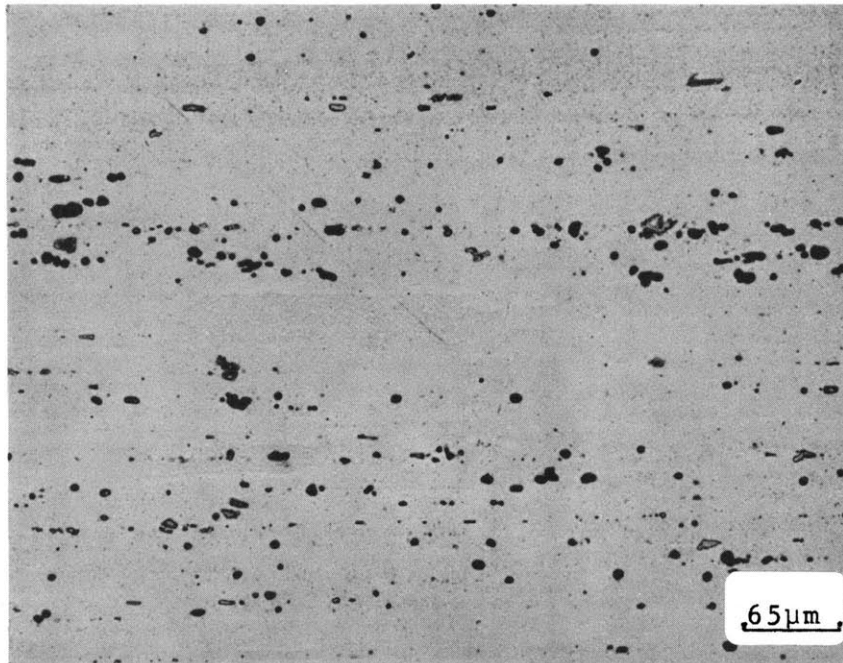


Figure 11 Inclusions in 2024-T4 aluminum (unetched).

The third size range is extremely fine ($<0.2\mu\text{m}$) and is observed as black points on etched (1.25 min, 12% Nital) surfaces (Figure 10). They often appear to lie along curved and straight lines and are possibly due to precipitation along prior austenite grain boundaries.

Inclusion spacings for these three size ranges were measured by the same technique as used for 4340 steel.

3.1.3 COMMERCIAL ALUMINUM ALLOYS - 2024, 7075, 7475

These commercial alloys are high-strength precipitation hardened alloys which are used widely in the aircraft industry. Hardening in the 2000-series alloys results from precipitates formed of Al-Cu-Mg, while precipitates in the 7000-series are composed of Al-Zn-Mg. Compositions of these alloys is given in Table 3. The difference between 7075 and 7475 is the lower Si, Fe, Mn and Ti contents; lowering these residual elements decreases the volume fraction of inclusions.

Inclusions in these alloys can be divided into three types which distinguish their size and origin⁽⁵⁵⁾.

a) Large precipitates (1-100 μm) form during casting and are composed of iron and silicon-rich compounds. These are reduced in 7475 versus 7075.

b) Intermediate size precipitates (.05 - .5 μm) are chromium, manganese, or zirconium-rich compounds which precipitate during ingot homogenization.

TABLE 3
 COMPOSITION OF COMMERCIAL ALUMINUM ALLOYS
 CHEMICAL COMPOSITION (w/o)

Alloy	Zn	Mg	Cu	Si	Fe	Mn	Cr	Ti
7075	5.2-6.2	1.9-2.6	1.2-1.9	.40 max	.50 max	.30 max	.18-.35	.20 max
7475	5.1-6.1	2.1-2.9	1.2-2.0	.10 max	.12 max	.06 max	.18-.25	.06 max
2024	.25 max	1.2-1.8	3.8-4.9	.50 max	.50 max	.30-.90	.10 max	-

7475 - Supplied as 2.54 cm plate by Reynolds Aluminum, Courtesy R.E. Zinkham

c) Small precipitates ($0.1\mu\text{m}$) are the metastable and stable precipitates which form during ageing.

Alloy 2024 was purchased as 1.27cm rolled plate. It was solutionized in air at $494 \pm 5^{\circ}\text{C}$ for five hours, water quenched, and allowed to naturally age at least 48 hours at room temperature. With this ageing treatment the alloy is designated 2024-T4. Alloy 7075 was solutionized at $483 \pm 5^{\circ}\text{C}$ for five hours, water quenched, and artificially aged at $121 \pm 2^{\circ}\text{C}$ for 24 hours in air. This is the full hardness temper designated 7075-T6.

The 7475 material was supplied as 7.6cm plate by the Reynolds Aluminum Corp. It was tested as-supplied in the -T651 temper: solutionized 483°C for five hours, quenched, stretched 1 to 3% plastically, aged 121°C for 24 hours.

Figures 11, 12 and 13 show the microstructure of the three alloys. It is seen that 2024 and 7075 contain a large volume fraction of inclusions (up to 3% ⁽⁵⁵⁾), and the number present in 7475 is relatively smaller. The number and calculated spacing of large inclusions was measured for these alloys as previously described for the steels.

3.2 MECHANICAL TESTING

3.2.1 TENSILE TESTING (AXISYMMETRIC)

Round tensile specimens were machined from each of the

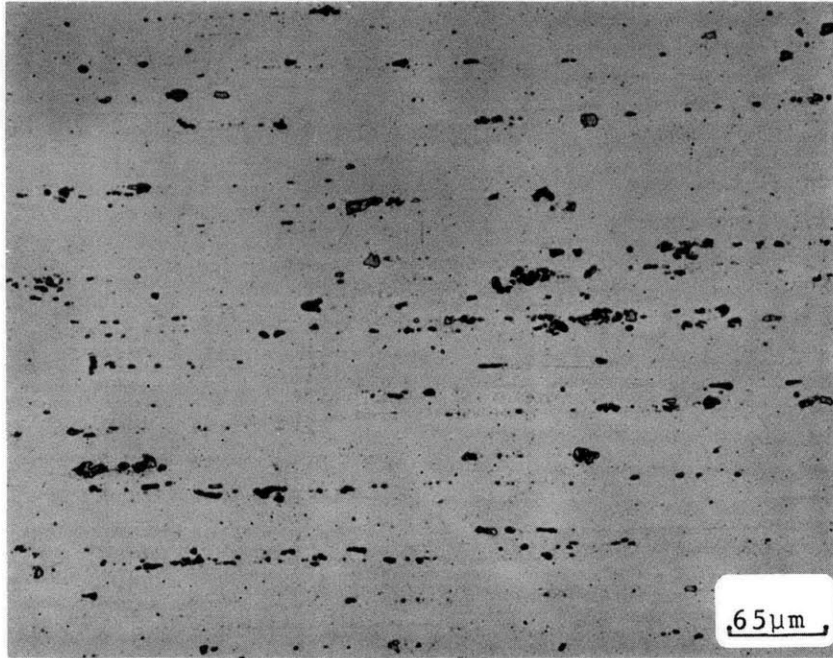


Figure 12 Inclusions in 7075-T6 aluminum (unetched).

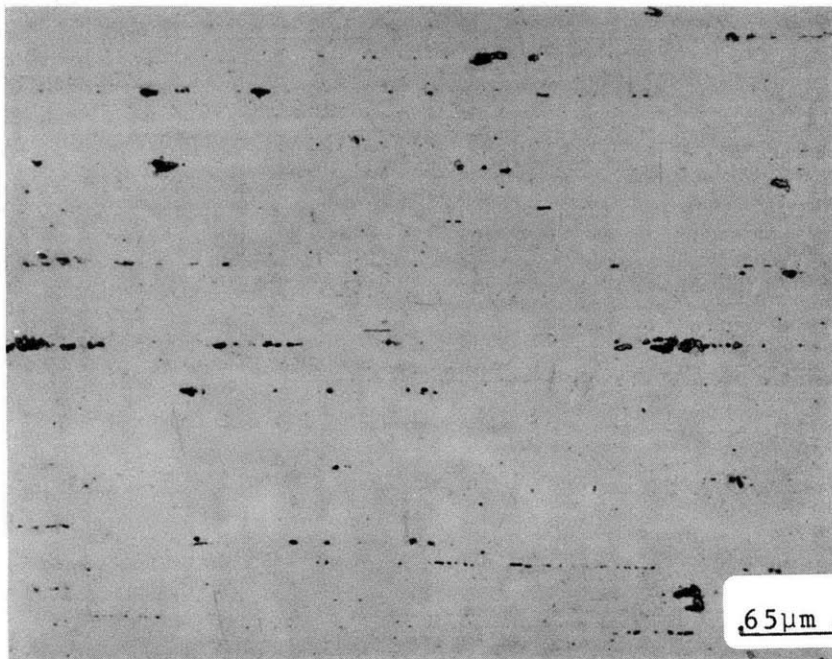


Figure 13 Inclusions in 7475-T651 aluminum (unetched)

alloys tested with their axes parallel to the rolling direction of the plate stock. This straining direction would thus correspond to the direction of maximum stress in the fracture toughness specimens. The respective heat treatments were performed, and the samples were abraded with SiC paper and polished with Wenol polish on a lathe. Diameters of the 4340 and maraging 300 specimens were 0.406cm and of the aluminum specimens were 0.635cm. The length of the reduced section was 2.86cm for all specimens to permit use of a 2.54cm Instron extensometer. Threaded specimen grips coupled with a universal joint in the load train allowed good alignment.

Tests were performed on a 10,000 lb. Instron tensile testing machine at an extension rate of 0.126 cm/min or 0.051 cm/min. An Instron extensometer was used to measure displacement over a 2.54cm gauge length. Accuracy of the extensometer readout was ± 0.0002 cm.

Parameters which were measured were 0.2% yield stress (σ_y), ultimate tensile stress (σ_u), true strain to necking (ϵ_u), strain hardening exponent (n), reduction in area (RA), and true fracture stress (σ_f). The strain hardening exponent (n) was found by taking points off the load-extension curve, converting to true stress-true strain, and plotting log true stress versus log true strain⁽⁵⁶⁾. The slope of the resulting line was taken to be n. The true stress at fracture was corrected for necking with the Bridgmen correction factor⁽⁵⁶⁾.

Reduction in area measurements were made with vernier calipers accurate to ± 0.001 cm. Strain to fracture (ϵ_f) was calculated as:

$$\epsilon_f = \ln(e_f + 1) = \ln \left[\frac{A_o - A_f}{A_f} + 1 \right] = \ln \left[\frac{A_o}{A_f} \right]$$

$$RA = \frac{A_o - A_f}{A_o} = 1 - \frac{A_f}{A_o}$$

$$\epsilon_f = \ln \frac{1}{1 - RA} \quad \text{Eq. 22}$$

Three notched tensile specimens of 4340 were tempered at 316°C , 427°C and 510°C and fractured. The purpose of these tests was to generate fracture surfaces which were produced under different constraint and triaxiality from the other tensile tests. The notched specimens had a 0.635cm outer diameter with a 60° circumferential V-notch machined around the center of the specimen. The radius at the tip of the notch was approximately 0.0046cm, and the diameter at the base of the notch was 0.48cm.

3.2.2 PLANE-STRAIN TENSILE TESTING OF 4340 AND MARAGING 300

A drawing of the plane-strain tensile specimen (PSS) used in this study is shown in Figure 14. This specimen is designed to allow only plane-strain deformation; it may elongate in the length direction and thin in the reduced

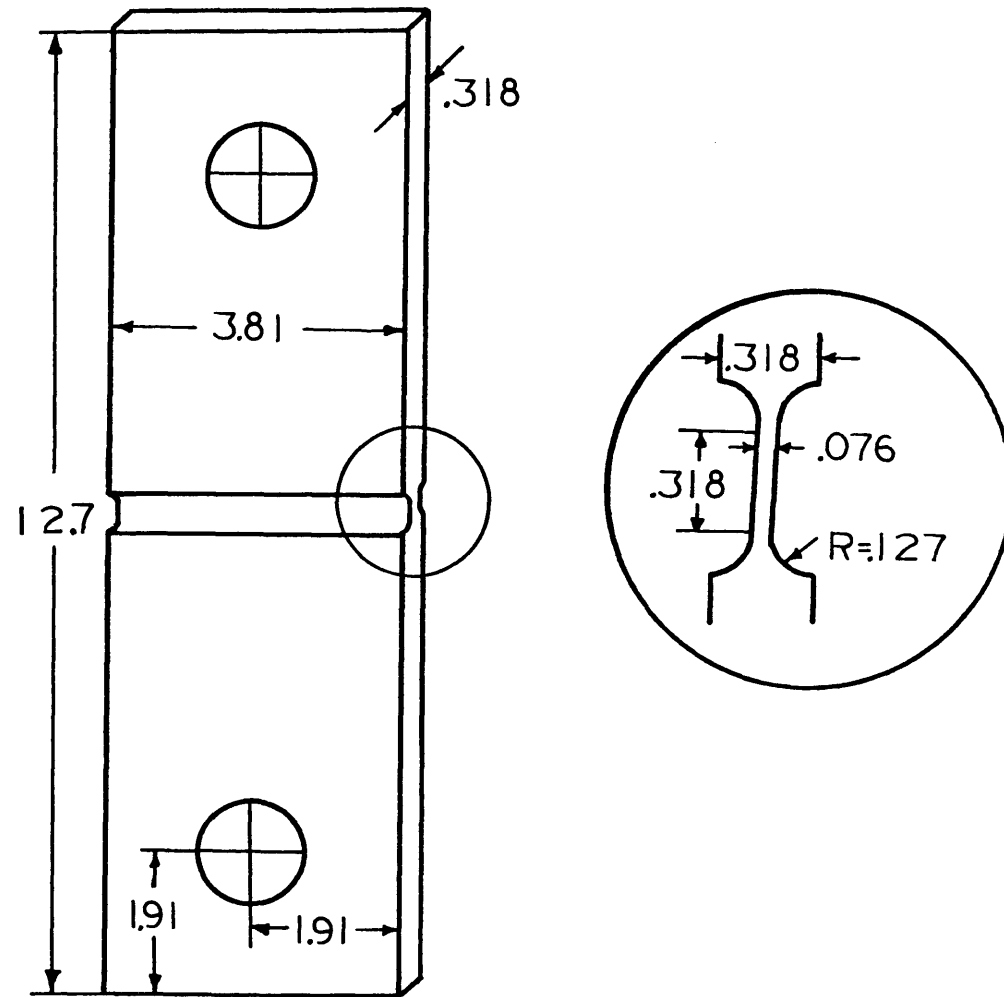


Figure 14 Plane strain tensile specimen. Dimensions are in centimeters.

section, but deformation in the width direction is prevented by elastic constraint of the unreduced thickness. Several criteria were applied to its design.

a) The height of the reduced section should be approximately four times the thickness of the reduced section. This would roughly correspond to height-diameter criteria for axisymmetric tensile specimens.

b) The unreduced section thickness should be great enough that it does not yield plastically at any of the applied loads.

c) The width of the specimen should be many times the height of the reduced section so as to minimize the effects of width-direction plastic strains which occur at each edge. This is the most difficult criterion to satisfy or correct for. Since it was desired to have the tensile ligament of these specimens oriented the same as the ligament ahead of the crack in the fracture toughness specimens, the width of the PSS specimens was limited by the thickness of the plate materials. Thus for 4340 the width was 3.81cm and for maraging 300, 2186cm, giving width to height ratios of 9:1 and 12:1, respectively.

Since yielding occurs at each edge, the over-all measured stress is less than the true plane-strain stress in the center of the specimen. An analysis by A.K. Ghosh⁽⁵⁷⁾ gives a correction factor in terms of a material strain hardening

exponent (n) and plastic anisotropy parameter R ($R = d\epsilon_2/d\epsilon_3$, thus for isotropic plastically strained materials $R = 1$ ⁽⁵⁸⁾). Ghosh measured plastic strains using photodeposited grids on the back side of singly grooved tensile specimens of brass and steel. The width-to-height ratio was 10:1. For these specimens Ghosh found that the central 50 percent of the sample was plane-strain. By using his measured strain distribution and assuming power-law hardening he arrived at the following expression to relate the measured axial stress ($\bar{\sigma}$) to the true plane-strain stress ($\sigma(0)$).

$$\sigma(0) = 4\bar{\sigma} / \left\{ 3 + \left[\frac{\sqrt{2R+1}}{(1+R)} \right]^{n+1} \right\} \quad \text{Eq. 23}$$

PSS specimens were milled and finish-ground using a special hold-down fixture to insure that the reduced section surfaces were flat and parallel. After machining, the specimens were heat treated, abraded, and polished. Finally, the specimens were electropolished (9% perchloric acid, 45% acetic acid, 45% butylcellosolve, 5°C, 30v) using a portable electropolisher with a pointed cathode which fit into the specimen groove. Typical polishing times were 5 minutes per groove side.

The samples were pulled in a Materials Testing System (MTS) Model 810 hydraulic closed-loop testing machine.

Extension was under stroke control at an elongation rate of 0.0013 cm/sec, giving an approximate strain rate to necking of 0.004/sec.

Displacements were monitored with an LVDT extensometer accurate to 2.5×10^{-5} cm⁽⁵⁴⁾ which was positioned to measure the change in thickness at the center of the reduced section. These measurements were accurate only to the necking strain since the extensometer was not generally positioned exactly at the neck location. Since the center of the specimen was in plane strain; the thickness strain equaled the axial strain. Load and extensometer displacement were recorded on a X-Y recorder. Measured quantities include yield stress, ultimate stress, fracture stress, uniform strain to necking, reduction in area, and work hardening exponent (calculated as with the axisymmetric tests).

3.2.3 FRACTURE TOUGHNESS TESTING

Fracture toughness tests were conducted using compact tension specimens designed in accordance with ASTM Standard E399-72. Figure 15 shows the specimen. Since the ASTM standards call for a certain ratio of specimen thickness to plastic zone size, thinner specimens can be used for less tough heat treatments. The specific specimen thicknesses are listed in Table 7 of Chapter 4 on Results.

Tests were performed on five tempering temperatures of

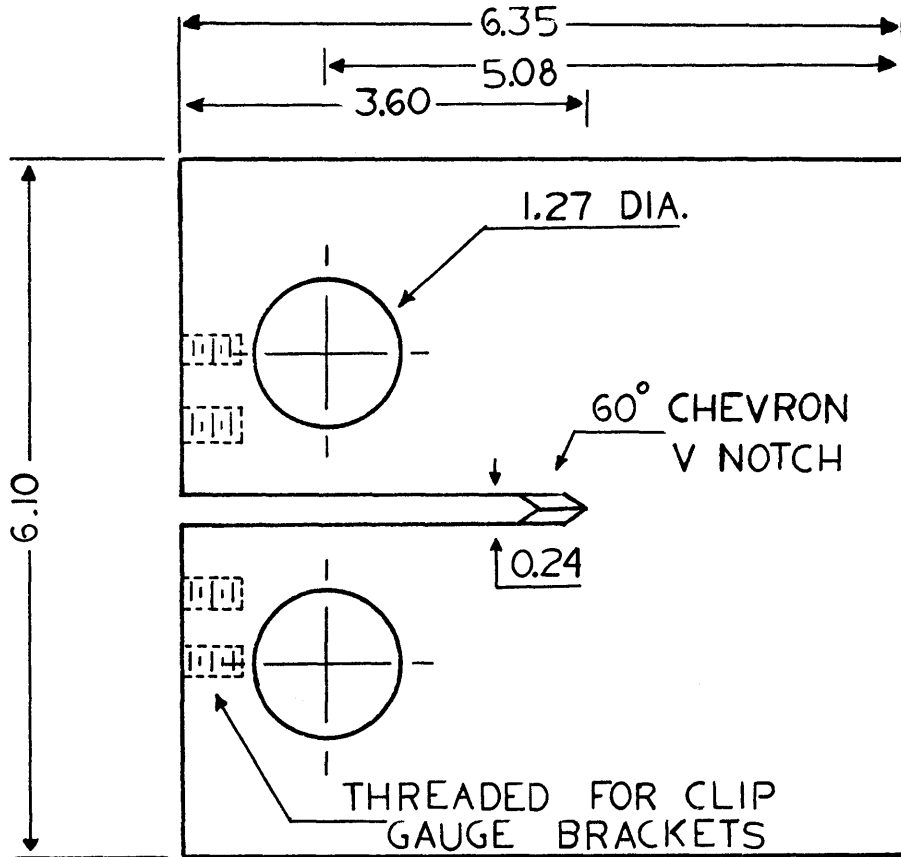


Figure 15 Compact tension fracture toughness specimen. Dimensions are in centimeters.

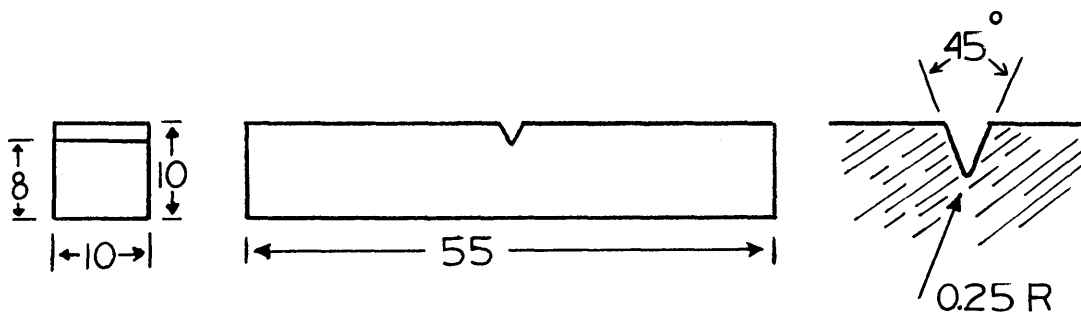


Figure 16 Standard size Charpy impact specimen. Dimensions are in millimeters.

4340, eight ageing treatments of maraging 300, and on 2024-T4, 7075-T6, and 7475-T651 aluminum. All specimens were oriented with the stress direction in the rolling direction of the plate and the crack plane perpendicular to the rolling direction.

An MTS hydraulic testing machine was used to fatigue precrack the specimens at a frequency of 10-20 Hz. The final 0.063cm of the fatigue crack was propagated at a stress intensity of less than one-half the critical stress intensity.

A clip-on gauge with four foil strain gauges was used to measure the crack opening displacement. This was clipped between two brackets which were attached to the specimen by screws. The ramp function of the MTS was used to fracture the specimen under stroke control. The displacement rate was 0.0025cm/sec. Load and crack-opening displacement were monitored on an X-Y recorder.

Three specimens of 4340 were precracked as usual, pulled to a small crack extension, and wedged open. After removal from the MTS these specimens were impregnated with epoxy and sectioned to view the crack profile. A simple impregnation apparatus was set up in which a vacuum was pumped around the specimen, degassed epoxy was introduced over the sample while in vacuum, and with the specimen covered with liquid, air was readmitted. The air pressure forced the epoxy into the end of the wedged-open crack. The brand of epoxy was Buehler No. 20-8130 Epoxide Resin mixed 5:1 with hardener.

Shear lip size was measured using a optical microscope equipped with a micrometer stage. The width of the shear lip was measured several places along the specimen surface where the lip had reached a "steady state" size. Ten measurements per specimen were made, and an average value determined.

3.2.4 CHARPY IMPACT TESTING

Charpy impact tests were conducted at room temperature on specimens of three tempering treatments of 4340 steel. Standard full-size Charpy specimens were used (Figure 16). Three specimens of each treatment were run, and the energy to fracture was recorded. Specimen fracture surfaces were preserved for fractography.

3.3 SPECIMEN PREPARATION FOR THE SCANNING ELECTRON MICROSCOPE (SEM)

It is very important to have clean, unoxidized, and un-abraded fracture surfaces to do good SEM fractography. This can be difficult if the specimen must be cut to a size which will fit on the SEM stage. For the steel specimens, it was necessary to use a cut-off wheel for sectioning.

To protect these surfaces, all specimens were sprayed immediately after fracture with several coats of a clear laquer (Krylon Crystal Clear). This was easily removed before observation by cleaning the sample in acetone in an ultra-

sonic bath. Specimens were stored as-sprayed in a desiccator.

Aluminum alloy specimens were vacuum deposited with gold-palladium to cover the fast-forming oxide which causes charging in the SEM. This gives improved resolution.

CHAPTER IV: RESULTS

4.1 DISTRIBUTION OF INCLUSIONS

The spacing of inclusions in the five alloys, measured as discussed in Section 3.1.1, are presented in Table 4. Approximate volume fractions for each size range inclusion are calculated assuming an ideal cubic array of cubic particles with an estimated average size. The uncertainties in spacing shown in the table are the root mean square deviations from the mean value determined from five to ten counting areas.

The 4340 steel produced by the electroslag remelt process has a very low ($\approx 0.03\%$) combined volume fraction of inclusions. This is reflected in the large inclusion spacing of both size ranges. The particles in 4340 tend to be randomly dispersed, rather than be in stringers.

The maraging 300 is less clean than 4340, having a combined volume fraction of $\approx 0.4\%$ (see Figure 19a, 19b and 20). The large (1-15 μm) particles tend to be in stringers, so the average inclusion spacing given is less meaningful. Medium size inclusions also lie on lines (Figure 19b) which are probably interdendritic solute-rich regions produced during solidification. The fine ($< 0.5\mu\text{m}$) particles are evenly dispersed, although some also appear along stringers (Figure 10).

TABLE 4 INCLUSION SIZE, SPACING, AND VOLUME FRACTION

Alloy	Inclusion Size (μm)		Spacing (μm)		Volume Fraction (%)
			2D	3D	
4340	1-30	(ave.=5)	300 ± 100	130	0.03
	.1-1	(ave.=.3)	60 ± 5	10	0.0003
Maraging 300	1-15	(ave.=5)	130 ± 30	50	0.14
	0.5-1	(ave.=.7)	30 ± 3	9	0.05
	.1-.5	(ave.=.2)	5 ± 2	2	0.16
2024-T4	1-50	(ave.=5)	25 ± 2	14	3
7075-T6	1-30	(ave.=5)	25 ± 4	14	3
7475-T651	1-30	(ave.=5)	40 ± 12	20	1

All the aluminum alloys have inclusion contents much higher than the steels. Alloys 2024-T4 and 7075-T6 have equal spacings and volume fractions (3%) of their respective inclusions. The 7475-T651 is cleaner, with approximately 1% second phase particles. Inclusions in all three alloys are strung out in the rolling direction; this is more prevalent in the 7000 series alloys (see Figures 11-13).

4.2 AXISYMMETRIC TENSILE TEST RESULTS

Values determined from tensile tests of the five alloys are given in Table 5. Results are the average of two tests. Data for aluminum alloys 2024-T4 and 7075-T6 were supplied by R. Selines⁽⁵⁹⁾. See Section 3.2.1 for details on the testing procedures and methods of calculation.

The 4340 steels tempered at 316°C, 427°C and 510°C for one hour all show an upper and lower yield point followed by a Luders strain before work hardening begins. The yield strength in these cases was taken from the load at lower yield. The samples tempered at 270°C for one hour exhibit a continuously increasing load with no yield point phenomena; yield stress for this case was determined from the 0.2% offset load. It is seen that the yield stress, ultimate tensile strengths, and fracture stress decrease continuously with increasing tempering temperature.

TABLE 5 AXISYMMETRIC TENSILE DATA

Alloy & Heat Treatment	σ_y ksi/MPa	σ_u ksi/MPa	σ_f ksi/MPa	n	ϵ_u	RA (%)	ϵ_f
Aluminum							
2024-T4 ⁽⁵⁹⁾	47/320	68/470	91/630	0.16	0.14	32	0.38
7075-T6 ⁽⁵⁹⁾	75/520	82/560	96/660	0.10	0.09	34	0.40
7475-T651 ⁽⁶⁹⁾	75/520	- -	- -	-	-	-	-
4340 Steel							
270° C/1 hr.	222/1530	270/1860	317/2190	0.080	0.038	54	0.78
316° C/1 hr.	220/1520	246/1700	276/1900	0.064	0.030	54	0.78
427° C/1 hr.	202/1390	212/1460	246/1700	0.035	0.027	54	0.78
510° C/1 hr.	176/1210	183/1260	220/1520	0.044	0.043	56	0.82
Maraging 300							
427° C/1 hr.	189/1300	204/1410	246/1700	0.042	0.016	62	0.98
427° C/1.5 hr.	201/1390	216/1490	253/1750	0.038	0.014	61	0.94
427° C/3 hr.	225/1550	238/1640	284/1960	0.052	0.012	58	0.88
427° C/8 hr.	253/1750	267/1840	309/2130	0.057	0.010	56	0.82
427° C/15.5 hr.	279/1920	287/1980	319/2200	0.039	0.010	50	0.69
427° C/100 hr.	310/2140	318/2190	352/2430	0.034	0.009	48	0.65
483° C/3 hr.	279/1920	284/1960	356/2700	0.032	0.016	48	0.65
538° C/24 hr.	222/1530	238/1640	256/1770	0.038	0.040	42	0.54

Work hardening exponent (n) values for 4340 tend to decrease with decreasing strength. Figure 17 is a plot of log true stress versus log true plastic strain where the slope is n . Data start at lower strain levels for the high strength specimens because the Luders strain decreases with increasing strength. Points for all four strength levels fall on a reasonably straight line.

Values of the plastic uniform strain (ϵ_u) were determined as the true strain at which the load-elongation curve first becomes horizontal. The data show that uniform elongation in 4340 is quite low, varying between 3 and 4%. Except for the 510°C tempering treatment, this strain is significantly less than n , but it does follow the same trend as n with strength.

There is no significant variation of reduction in area (RA) with strength level for 4340 steel. The steel shows good ductility with a RA of 54%; the true fracture strain calculated from this is approximately 0.8.

Load-elongation curves for maraging 300 steel have a continuously increasing load to necking, so the yield stress was determined from the 0.2% offset load. Table 5 shows that σ_y , σ_u , and σ_f increase with longer ageing times at 427°C. The standard commercial ageing treatment (483°C for 3 hours) has σ_y and σ_u equivalent to the 427°C for 15.5 hour sequence,

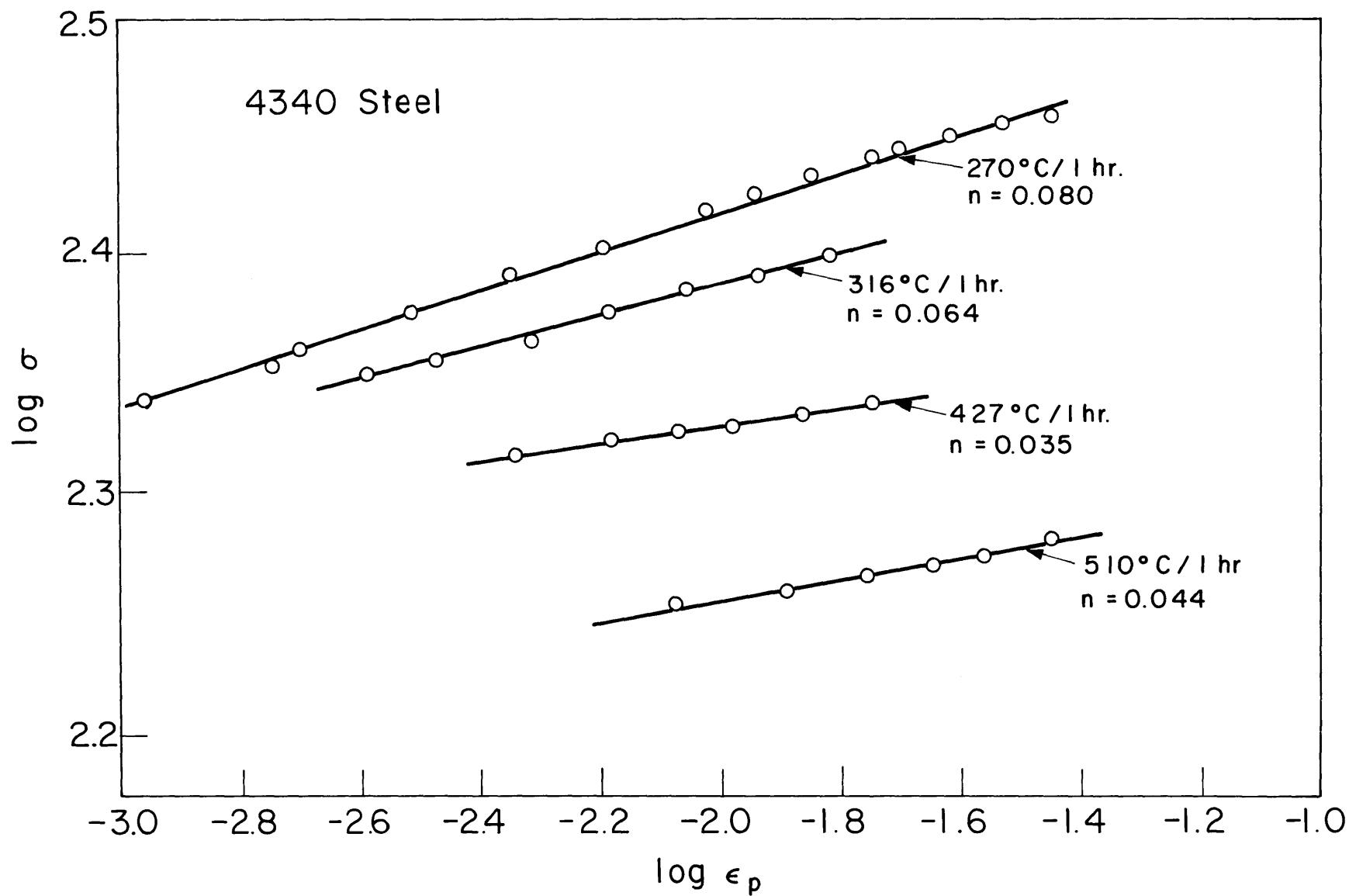


Figure 17 Log σ versus log ϵ_p for 4340 steel axisymmetric tensile tests.

but its fracture stress is significantly greater 356(2700) ksi(MPa) vs 319(2200) ksi(MPa). An over-ageing treatment (538°C/24 hr) gives σ_y and σ_u comparable to a treatment of 427°C for 3 hours, but the overaged condition has a lower fracture stress 256(1770) ksi(MPa) vs 284(1960) ksi(MPa).

Figure 18 gives log true stress-log true plastic strain plots with n as the slopes. The data show more curvature than with 4340 steel, but generally a straight line is a good fit. Values of n shown in Table 5 do not vary continuously with strength level.

The uniform elongation in maraging 300 is quite low and tends to decrease with increasing strength for ageing at 427°C. Except for the 538°C for 24 hour treatments, ϵ_u is much less than n .

Reduction of area for this material is also high, and it decreases slightly with increasing strength, except again for the 538°C for 24 hour treatment. This overaged condition has a lower RA (42% vs 58%) than the equivalent strength treatment at 427°C for 3 hours. There is no significant difference in RA between the commercial peak aged condition (483°C/3 hr) and its equivalent strength condition (427°C/15.5 hr).

Maraging 300 and 4340 steels are thus similar in several ways:

- 1) They are both high strength steels whose yield

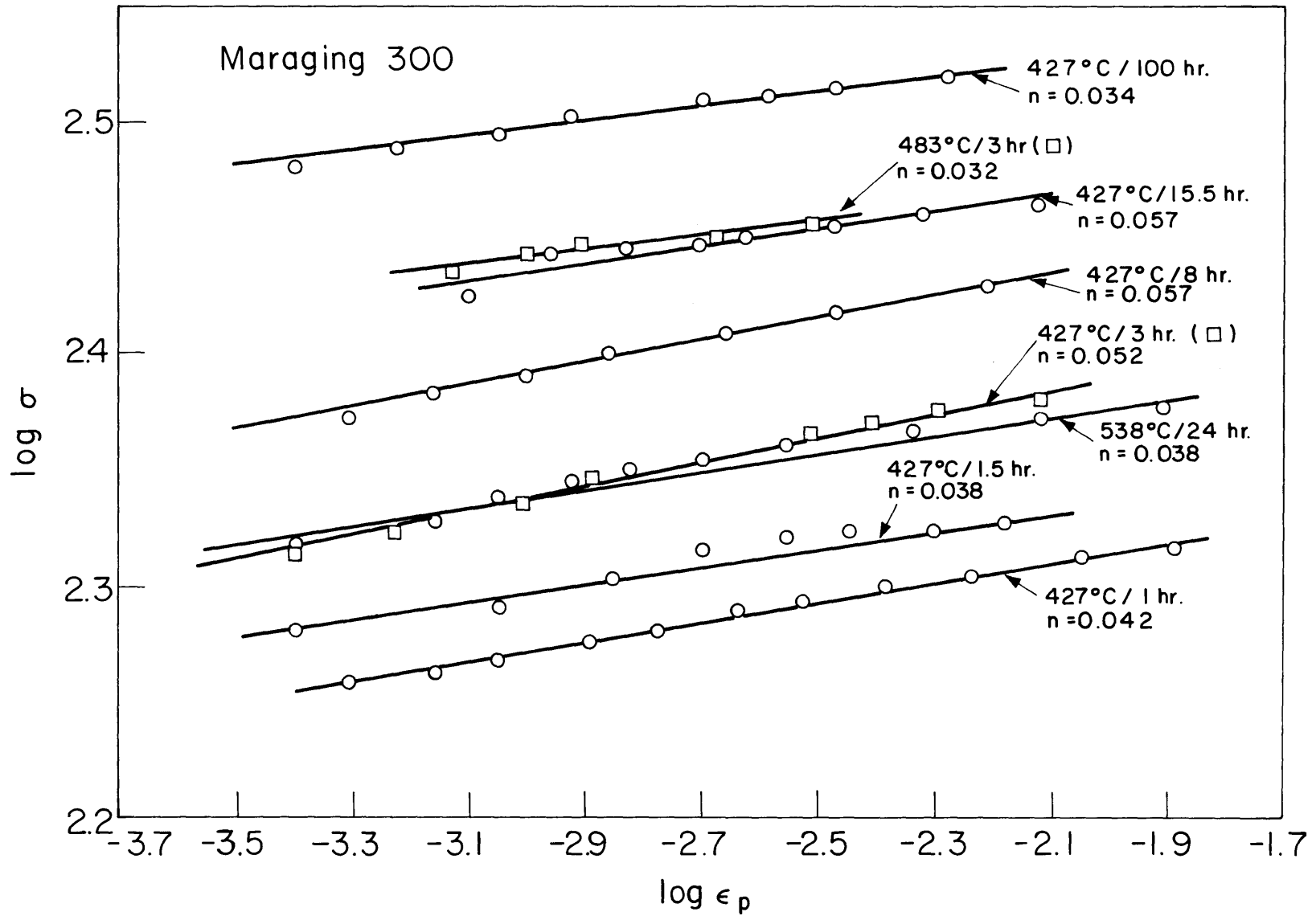


Figure 18 Log σ versus log ϵ_p for maraging 300 steel axisymmetric tensile tests.

strengths can be varied by suitable heat treatments.

- 2) They have very low uniform elongation to necking, but their reduction in area up to fracture is large. Their reductions in area do not change drastically with strength level but tend to decrease slightly with increased strength.
- 3) They have relatively low work hardening exponents which do not vary in a regular manner with the strength levels.

Aluminum alloys 7075-T6 and 7475-T651 have essentially equivalent strength properties^(59,69). Alloy 2024-T4 has considerably lower yield and tensile strengths than 7075-T6 but higher n and ϵ_u . Values of n and ϵ_u are nearly equal for each alloy. Reduction in area and fracture stress properties are similar. In comparison to the two steels, the aluminum alloys have lower strengths and RA but greater n and ϵ_u . The modulus of the aluminums is also lower: 10×10^6 psi (69×10^3 MPa) vs 25×10^6 psi (180×10^3 MPa) for maraging 300 and 30×10^6 psi (207×10^3 MPa) for 4340 steel.

4.3 PLANE STRAIN TENSILE TEST RESULTS

Data for plane strain tensile tests of 2024-T4 and 7075-T6 aluminum alloys⁽⁵⁹⁾, maraging 300 steel, and 4340 steel are

presented in Table 6. Tests were conducted as discussed in Section 3.2.2.

As expected σ_Y^{PS} , σ_u^{PS} , and σ_f^{PS} are higher in most cases than in the axisymmetric tests. The ratios of σ_Y^{PS} to σ_Y^{Axi} fall midway between 1.00, the value expected for the Tresca yield locus, and 1.155, the ratio for the von Mises yield locus⁽⁵⁶⁾.

Stress-strain curves of the plane strain specimens of 4340 steel show an inflection in slope shortly after yielding, suggestive of a Luders strain. This was less pronounced for higher tempering temperature samples. Curves for maraging 300 and the aluminum alloys increased continuously.

Strain hardening exponents for 4340 steel show a decrease with decreasing strength level and do not vary significantly from the axisymmetric data. Figure 19 plots log true stress versus log true plastic strain to get n: data points generally fall on a straight line. Similar plots for maraging 300 steel are shown in Figure 20. Data are linear for the three high strength conditions, but curvature for the 427°C/1 hr. treatment data points makes precise determination of n impossible. It varies from $n = 0.10$ for low strains to $n = 0.04$ at higher strains. Since we are interested in high strain behavior, the value of $n = 0.04$ is used for comparison in Table 6. The exponent does not vary with strength for the plane strain tests and is not much different in value from the

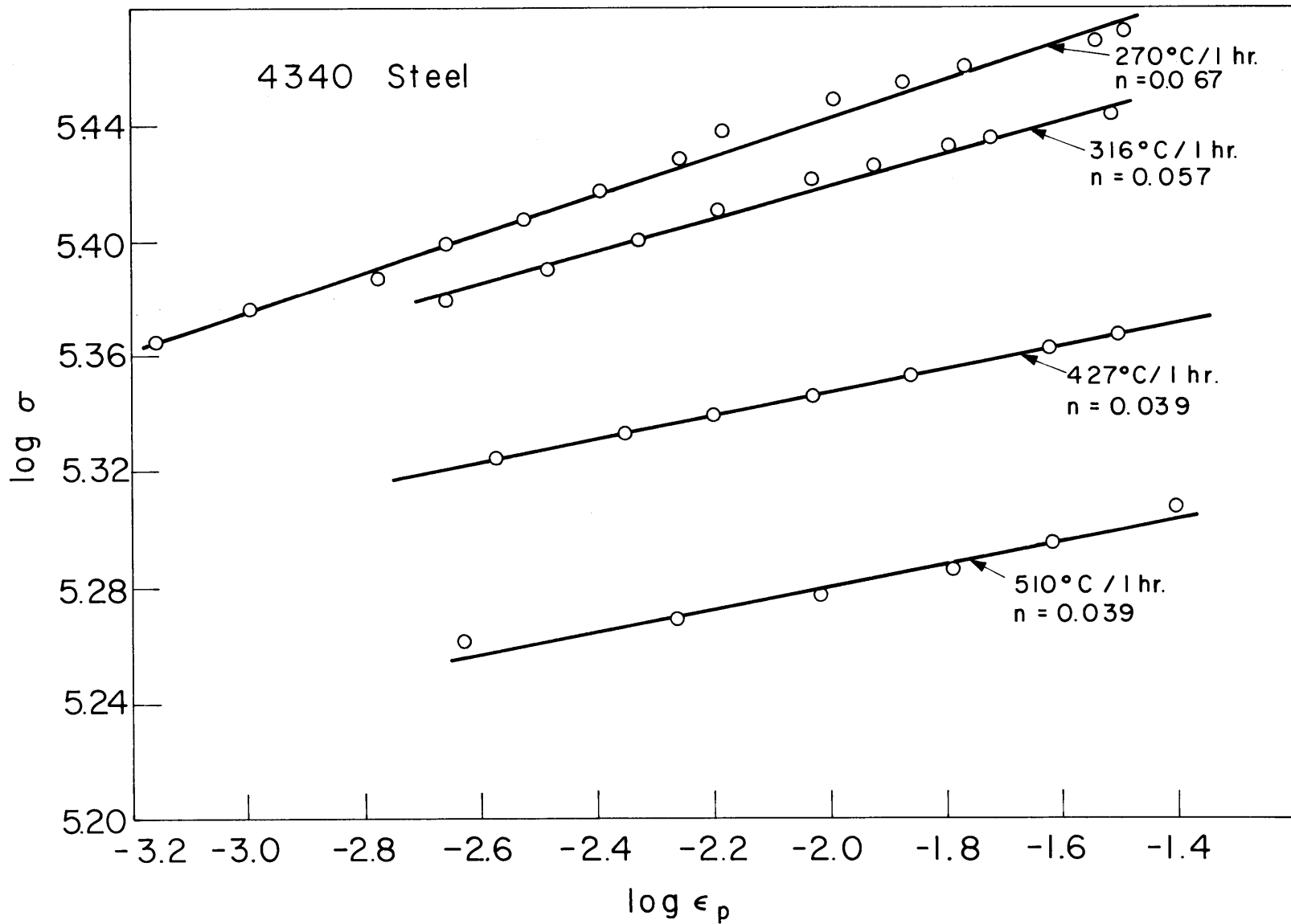


Figure 19 Log σ versus log ϵ_p for 4340 steel plane strain tensile tests.

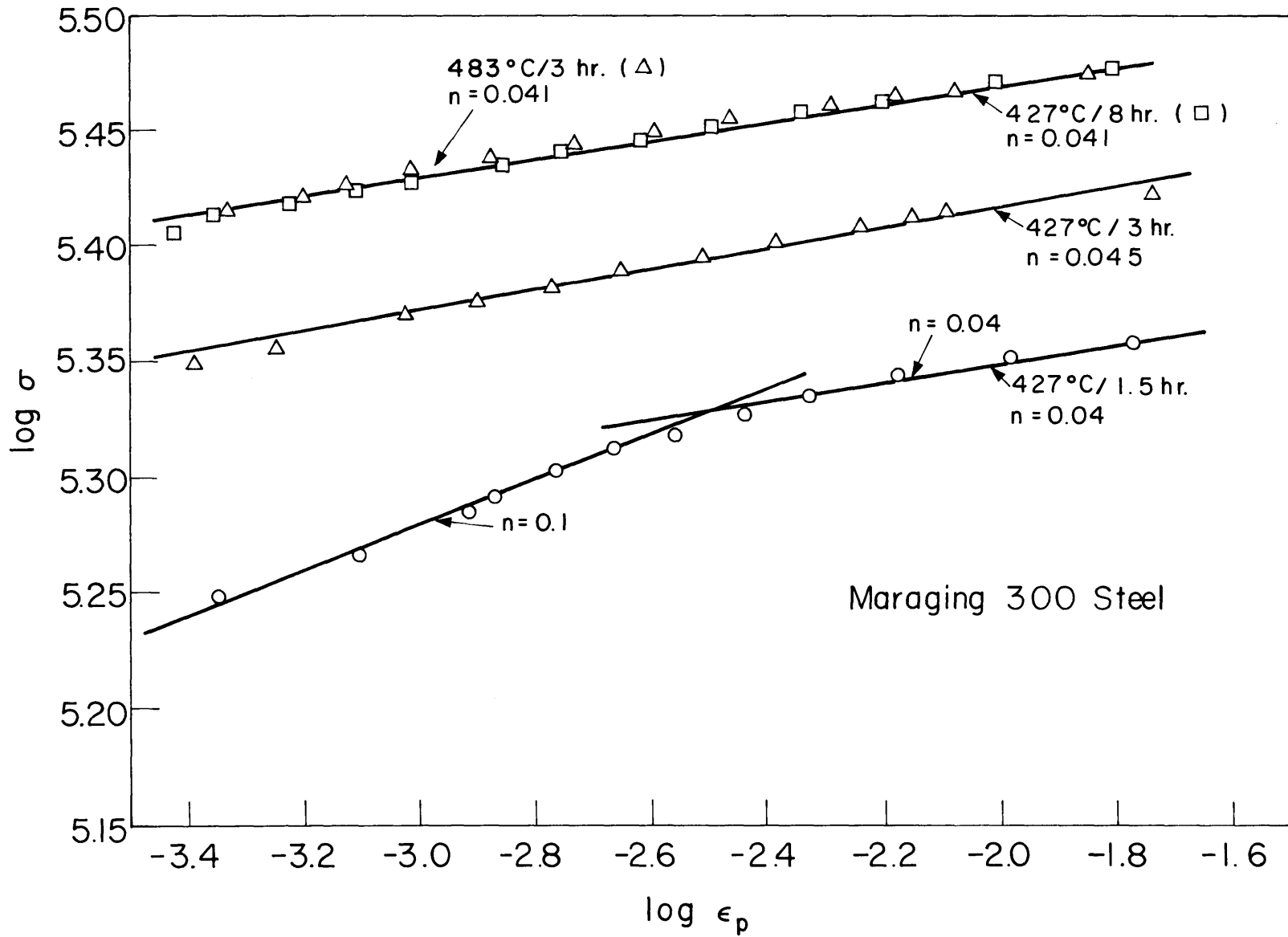


Figure 20 Log σ versus $\log \epsilon_p$ for maraging 300 steel plane strain tensile tests.

TABLE 6 PLANE STRAIN TENSILE DATA

Alloy & Heat Treatment	σ_y^{PS} ksi/MPa	σ_u^{PS} ksi/MPa	σ_f^{PS} ksi/MPa	n^{PS}	ϵ_u	RA^{PS} %	ϵ_f^{PS}	$\sigma_y^{PS}/\sigma_y^{Axi}$	% Plane Strain % \pm 5
Aluminum									
2024-T4 ⁽⁵⁹⁾	51/352	66/456	91/629	0.16	0.10	28	0.33	1.06	-
7075-T6 ⁽⁵⁹⁾	77/532	85/587	97/670	0.08	0.08	14	0.15	1.03	-
4340 Steel									
270°C/1 hr.	244/1680	296/2040	340/2350	0.067	0.032	20	0.22	1.09	83
316°C/1 hr.	237/1630	275/1900	- -	0.057	0.025	17	0.19	1.08	83
427°C/1 hr.	208/1440	233/1610	257/1770	0.039	0.031	19	0.21	1.03	82
510°C/1 hr.	181/1250	204/1410	245/1690	0.039	0.040	25	0.29	1.03	83
Maraging 300									
427°C/1.5 hr.	211/1460	240/1660	286/1970	0.04	0.023	28	0.33	1.05	82
427°C/3 hr.	250/1730	278/1920	- -	0.045	0.018	16	0.17	1.11	79
427°C/8 hr.	282/1950	308/2120	318/2200	0.041	0.020	14	0.15	1.11	77
438°C/3 hr.	289/1990	309/2130	329/2270	0.041	0.016	13	0.14	1.04	75

axisymmetric tests.

Log stress-log strain data for the aluminum alloys determined by Selines⁽⁵⁹⁾ also shows curvature. In this case, the n is lower at low strains and increases to a higher steady-state value at higher strains. For 2024-T4 n increases from 0.04 to 0.16; for 7075-T6 the change is from 0.02 to 0.08. Again the high strain values are listed in Table 6.

The uniform strains for 4340 steel plane strain specimens are about the same as the axisymmetric case, while plane strain values for maraging 300 steel are 1.5 to 2 times greater for specimens aged at 427°C. The strains are equal for specimens aged at 483°C for 3 hr. The aluminum alloys show a slight decrease in ϵ_u under plane strain.

Reduction in area is greatly decreased under plane strain loading as also shown in Tables 5 and 6. RA values for 4340 steel are less than one-half the round bar data, but there is no regular change in RA with strength. Maraging 300 steel shows a similar overall large decrease in RA, but in this case the RA decreases significantly also with increased strength. The RA for 7075-T6 drops to one-half the value for 2024-T4 (14% vs 28%) in plane strain; this follows the trend of the maraging steel.

The fracture stresses of the two aluminum alloys are nearly equal to each other (91 (629)ksi (MPa) for 2024-T4 vs 97 (620)ksi (MPa) for 7075-T6), and these values do not change

with strain mode. This is interesting considering the specimens fail by shear at 45° to the tensile axis in both the axisymmetric and plane strain tests.

Finally, the fractional width of the specimen which was under plane strain was measured using calipers to measure the width of the necked region at each side of the specimen groove. This necked region was very distinct for the steel specimens, and repeated measurements gave values accurate to well within $\pm 5\%$. These are shown in Table 6. It is seen that the width of the plane strain region averages approximately 80% of the total. This percentage is somewhat higher for the 4340 specimens since they are wider (3.81cm vs 2.86cm). The necked region was not as well defined on the aluminum alloy samples and was not measured.

4.4 FRACTURE TOUGHNESS TEST RESULTS

Data from fracture toughness tests carried out on 4340 steel and maraging 300 steel are shown in Table 7. Reference data for the aluminum alloys^(64,69) are also given. Tests were conducted according to ASTM specifications using fatigue pre-cracked compact tension specimens (see Section 3.2.3).

Load-clip gauge displacement records for 4340 steels bent over smoothly without pop-in, and candidate critical crack growth loads were determined using the secant intercept method. Specimens tempered at 510°C for 1 hr. did not

TABLE 7 FRACTURE TOUGHNESS TESTING RESULTS

Alloy & Heat Treatment	σ_Y ksi/MPa	K_{IC} ksi-in ^{1/2} /MN-m ^{-3/2}	t cm	$2.5 \frac{K^2}{\sigma_Y^2}$ cm	COD μm	r_P^x μm	λ μm	SL (±10%) μm
Aluminum								
2024-T4	47 ⁽⁵⁹⁾ /324	30 ⁽⁶⁹⁾ /33	-	2.6	25	325	-	-
7075-T6	75 ⁽⁵⁹⁾ /516	25 ⁽⁶⁴⁾ /27	-	0.7	10	90	-	-
7475-T651	75 ⁽⁶⁹⁾ /518	30 ⁽⁶⁹⁾ /33	-	1.0	15	130	-	-
4340 Steel								
270°C/1 hr.	222/1530	63/69	1.90	0.5	7	65	24±4	550
316°C/1 hr.	220/1520	71/77	2.56	0.7	9	80	27±4	1200
316°C/1 hr.	220/1520	68/74	2.56	0.6	9	80	27±4	1200
427°C/1 hr.	202/1390	97/106	2.55	1.5	20	190	41±4	2200
427°C/1 hr.	202/1390	99/108	2.56	1.5	20	190	41±4	2200
510°C/1 hr.	176/1210	144*/157	2.56	4.3	37	490	60±5	3000
510°C/1 hr.	176/1210	131*/143	2.53	3.6	37	490	60±5	3000
Maraging 300 * not valid K_{IC}								
427°C/1 hr.	189/1300	140*/153	1.53	3.8	50	430	126±20	3700
427°C/1.5 hr.	201/1390	121/132	2.54	2.3	36	290	95±12	1900
427°C/3 hr.	225/1550	96/105	1.53	1.2	20	150	64±7	1300
427°C/8 hr.	253/1750	62/68	1.27	0.4	7	50	39±6	500
427°C/15.5 hr.	279/1920	50/54	1.27	0.2	4	26	32±6	300
427°C/100 hr.	310/2140	<40/<44	1.01	0.1	≤3	≤13	34±10	350
483°C/3 hr.	279/1920	82/89	0.64	0.6	12	70	54±10	2200
538°C/24 hr.	222/1530	75/82	1.01	0.7	13	90	55±10	700

satisfy ASTM thickness requirements ($t > 2.5 \left(\frac{K}{\sigma_y} \right)^2$), and their K_Q values are noted by an asterisk. K_{IC} increases roughly by a factor of two, from 63 ksi-in^{1/2} (69 MN-m^{-3/2}) to ≈130 ksi-in^{1/2} (142 MN-m^{-3/2}), as the yield strength decreases from 222 ksi to 176 ksi. This is shown in Figure 21, along with some data from the literature on K_{IC} vs σ_y for 4340 steel. It is seen that the curve of the present data lies above the other data. Values of crack opening displacement (COD) and plastic zone size directly in front of the tip (r_p^x) are also given in Table 7 as calculated from Eqns. 3 and 2, respectively. Both r_p^x and COD increase by a factor greater than 5 times as K_{IC} doubles.

The three lowest toughness specimens of maraging 300 showed a pop-in and immediate crack propagation through the entire specimen; higher toughness specimens behaved as the 4340. The lowest toughness specimen (427°C for 100 hr.) failed during precracking at a $K \leq 40$ ksi-in^{1/2} (<44 MN-m^{-3/2}); this value is reported for comparison. The highest toughness specimen (427°C for 1 hr.) was too thin to satisfy the ASTM thickness criterion, and its K_Q values are reported with an asterick.

It is seen that K_{IC} for maraging 300 steel generally increases with lowered yield strength (see Figure 21). Toughness of the commercial treatment (483°C for 24 hr.) is considerably greater than the equivalent strength, low temper-

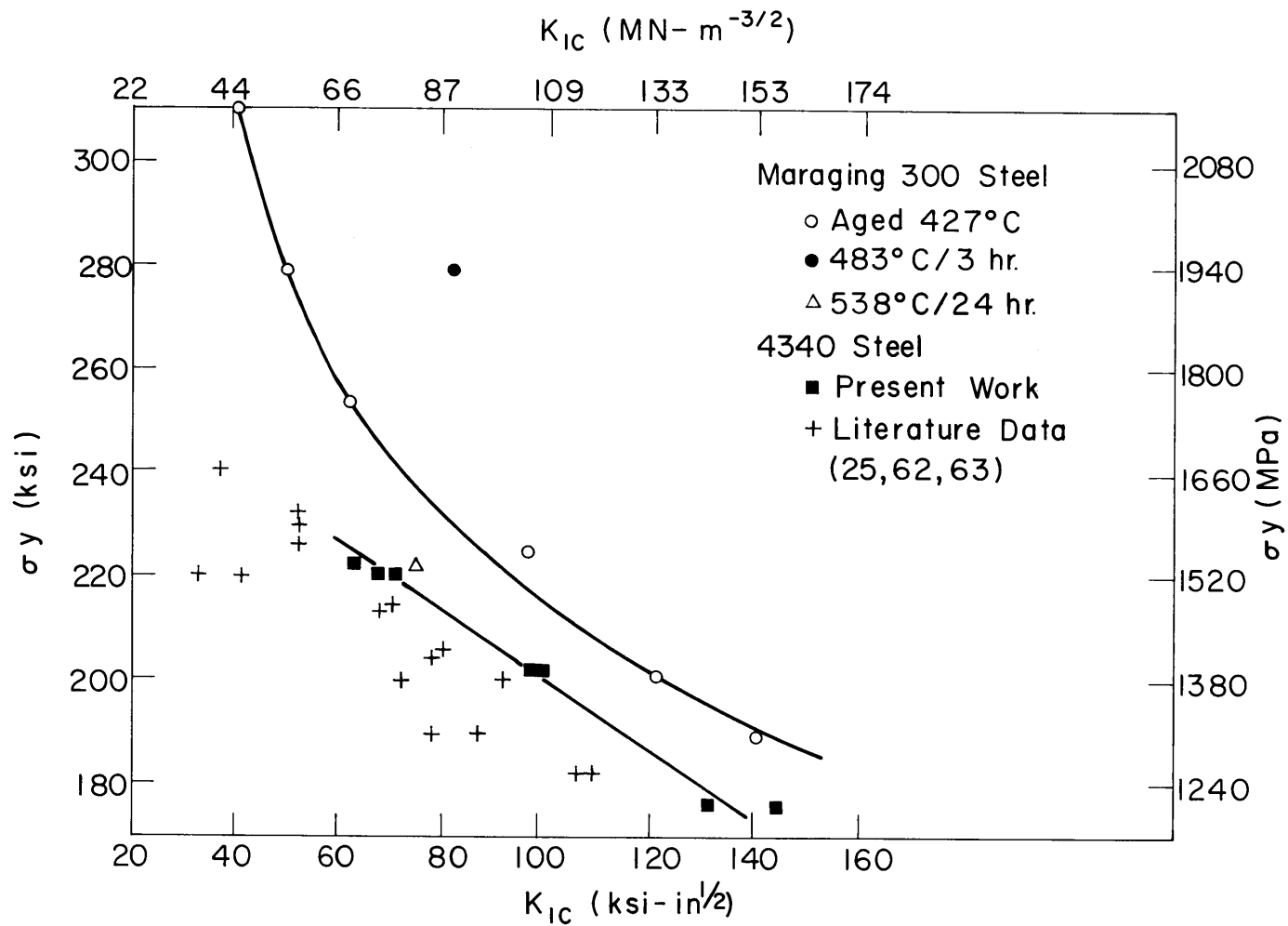


Figure 21 Yield stress versus K_{IC} for 4340 and maraging 300 steels.

ature ageing treatment (82 vs 50 ksi-in^{1/2}, 89 vs 54 MN-m^{-3/2}). K_{IC} for the over-aged specimen (538°C for 24 hr) is lower than its equivalent strength, low ageing temperature counterpart (75 vs 96 ksi-in^{1/2}, 82 vs 105 MN-m^{-3/2}). Values of COD and r_p^x vary by over a factor of 10 with strength. Comparison of equal strength levels between 4340 and maraging 300 steels shows that the maraging steel is tougher by 20 to 30 percent.

The aluminum alloys all demonstrate a low fracture toughness compared to the steels. Alloys 2024-T4 and 7475-T651 have equivalent K_{IC} , although the 2024-T4 has considerably lower yield strength. Alloy 7075-T6 is approximately 20% less tough (25 vs 30 ksi-in^{1/2}, 27 vs 33 MN-m^{-3/2}) at the same yield strength.

4.5 FRACTOGRAPHIC OBSERVATIONS AND MEASUREMENTS

4.5.1 RIDGE SPACING ON 4340 AND MARAGING 300 STEELS

Optical and scanning electron microscope observations showed ridges or zig-zags, on the plane strain portions of fracture toughness specimens of 4340 and maraging steels. They were also seen on notched tensile specimens and charpy impact specimens of 4340 steel. Zig-zags were not observed on any of the aluminum alloy specimens nor on the smooth bar tensile specimens of the steels.

Figure 22 shows an SEM micrograph of ridges on the flat plane strain surface of a 4340 fracture toughness specimen

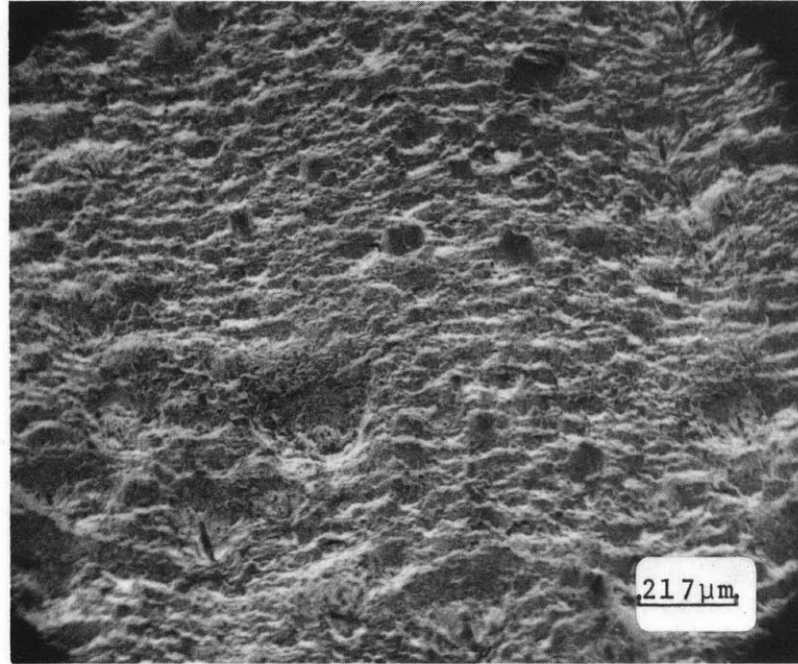
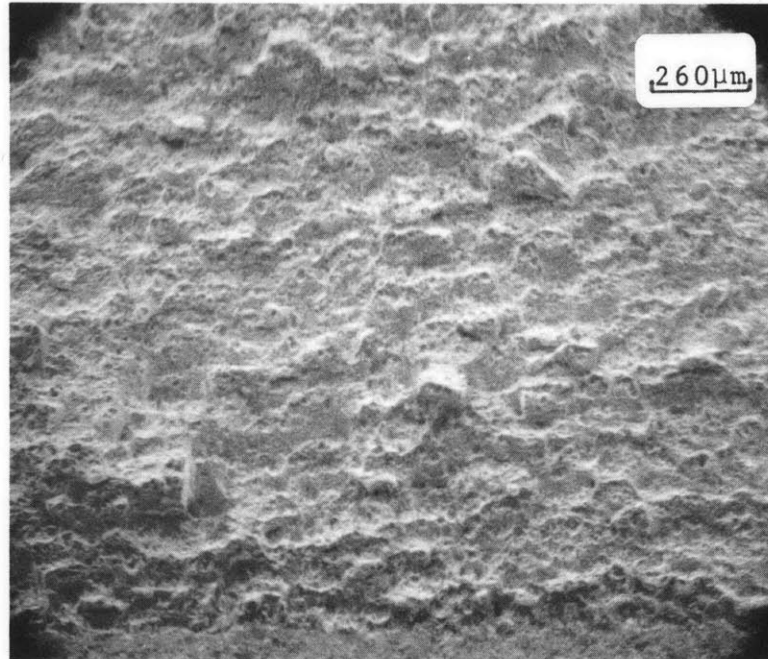


Figure 22 Ridges on plane strain region of fracture toughness specimen of 4340 steel ($K_{IC} \approx 130 \text{ ksi-in}^{1/2} / 142 \text{ MN-m}^{-3/2}$, $\lambda = 60 \pm 5 \mu\text{m}$). Tilted 20° .

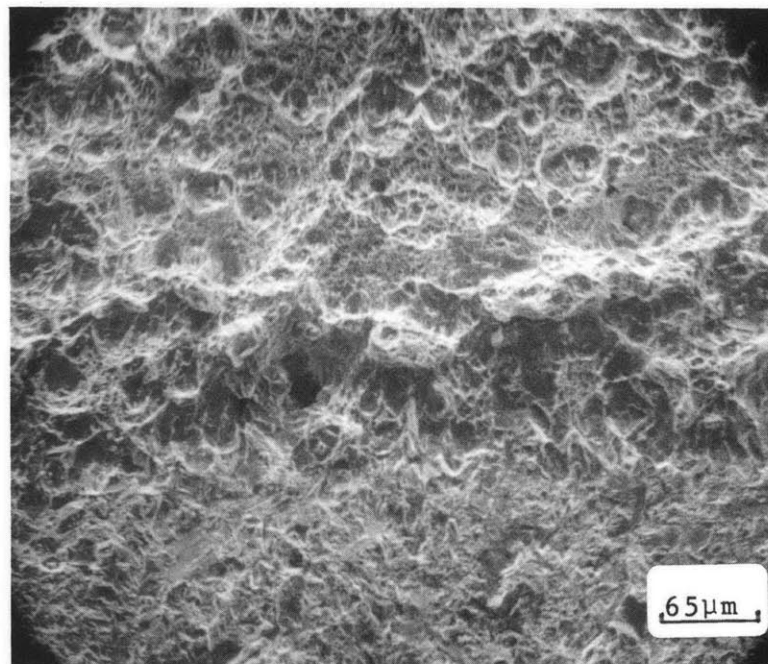
tempered 510°C for 1 hr. Crack propagation is from bottom to top. The wavelength of the ridges is $60 \pm 5 \mu\text{m}$, and they can easily be observed with the naked eye. The zig-zags in Figure 22 cover a large majority of the fracture surface, but several large voids are present which break up the continuity of the lines. The spacing of these voids roughly corresponds to the spacing of the larger inclusions in this alloy ($300 \mu\text{m}$, Table 4). The continuous width of a particular line of ridge is approximately 5 times the ridge spacing.

Typical zig-zags which occur on maraging 300 steel are shown in Figure 23a for a fracture toughness specimen aged 427°C for 1 hr. Figure 23b is a higher magnification view of the same specimen showing the transition between the fatigued precracked area (bottom) and fast fracture region (top). Crack propagation direction is bottom to top. Ridges are less continuous on the maraging steel than the 4340 steel, although the very large voids ($>100 \mu\text{m}$) such as seen in Figure 22 are absent. Large voids in Figure 23b range up to $50 \mu\text{m}$ in size; these are presumed due to the large ($>10 \mu\text{m}$) inclusions present in this steel.

Figures 23a and 23b show an irregularly shaped "stretched" or sheared off zone between the fatigue and ductile fracture regions. This zone appears to consist of greatly elongated tear dimples. The extent of the zone is very irregular across the crack front, ranging in width between 0 and $100 \mu\text{m}$.



(a)



(b)

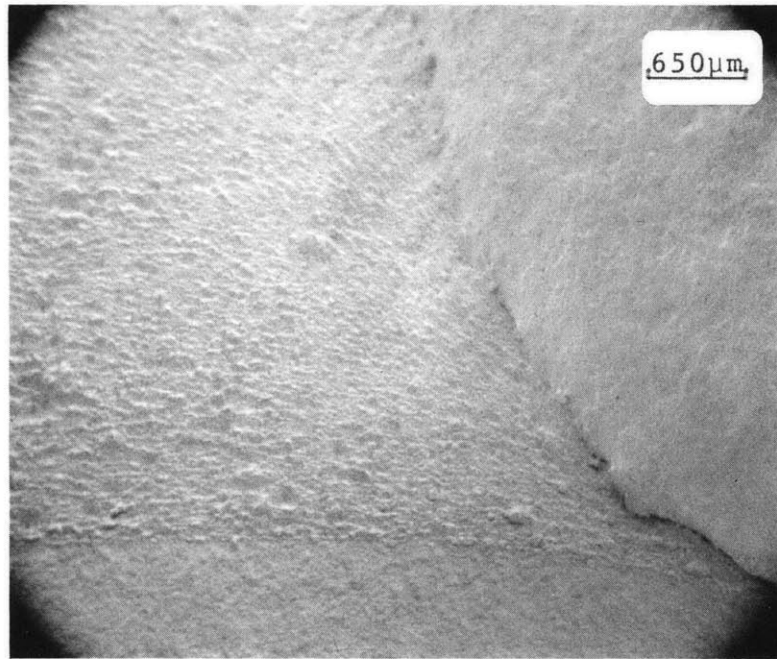
Figure 23

Ridges on plane strain region of fracture toughness specimen of maraging 300 steel ($K_{IC} \approx 140 \text{ ksi-in}^{1/2} / 153 \text{ MN-m}^{-3/2}$, $\lambda = 126 \pm 20 \mu\text{m}$): (a) ridges and (b) higher magnification view of fatigue-fast fracture transition. Both tilted 25° .

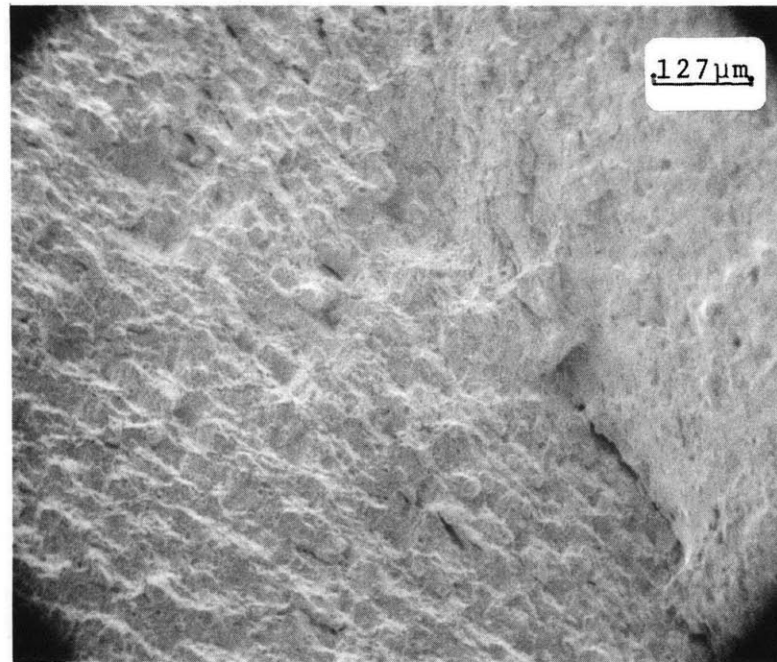
The calculated COD for this specimen is $50\mu\text{m}$, so the size scale between the stretched zone and COD is comparable. Formation of zig-zags begins immediately after the stretched zone as also shown in Figures 23a and 23b. The morphology of fracture initiation in 4340 steel is very similar: the irregularity of the stretched region is even more pronounced because the fatigue crack tends to branch into multiple crack fronts.

For both 4340 and maraging steels, the shape of the crack front becomes bowed as shear lips form and the crack propagates through the specimen. This is shown by the shape of the ridge front in Figure 24a where the overall direction of crack propagation is from bottom to top. The relatively smooth shear lip is on the right. It is seen that the ridges are parallel to the fatigue crack front initially, but begin to bow with further crack advance. In the higher magnification view of Figure 24b, it is evident that the zig-zags are tangential to the edge of the shear lip.

The spacing or wavelength of the ridges increases as the fracture toughness of the alloy is increased by heat treatment. This is shown in Figures 25a and 25b for 4340 steel: the top fractograph is of 4340 tempered to a K_{IC} of $70 \text{ ksi-in}^{1/2}$ ($76 \text{ MN-m}^{-3/2}$); the bottom is tempered to a K_{IC} of $\approx 130 \text{ ksi-in}^{1/2}$ ($142 \text{ MN-m}^{-3/2}$). The wavelengths of each are $27\pm 4\mu\text{m}$ and $60\pm 5\mu\text{m}$, respectively. At lower K_{IC} values the

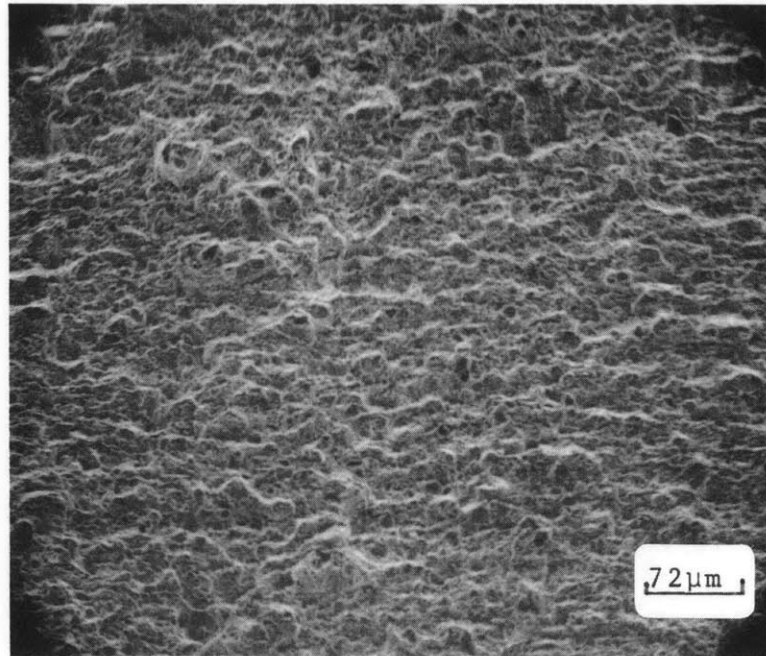


(a)

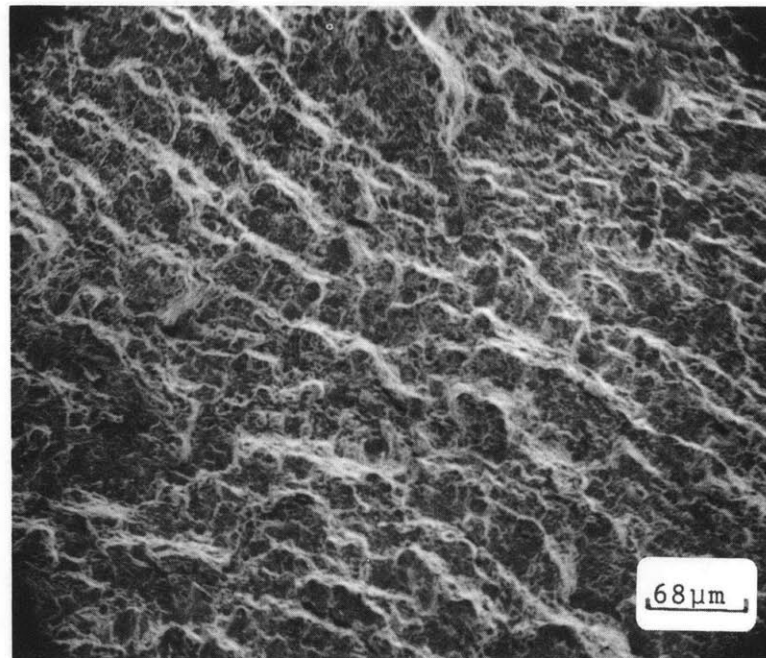


(b)

Figure 24 Curvature of ridges which become tangential to shear lip on fracture toughness specimen of 4340 steel: (a) overall view and (b) higher magnification. Both tilted 20°.



(a)



(b)

Figure 25

Increase of ridge wavelength with K_{IC} on 4340 steel fracture toughness specimens: (a) $K_{IC} = 70 \text{ ksi-in}^{1/2} / 76 \text{ MN-m}^{-3/2}$, $\lambda = 27 \pm 4 \mu\text{m}$; (b) $K_{IC} \approx 130 \text{ ksi-in}^{1/2} / 142 \text{ MN-m}^{-3/2}$, $\lambda = 60 \pm 5 \mu\text{m}$. Both tilted 45° .

spacing is not only shorter, but the ridges are less continuous and not as well formed.

The measured wavelengths (λ) of each of the heat treatments given to 4340 and maraging 300 steel are given in Table 7. The error limits shown are the root mean square deviation of at least 50 wavelength measurements made from several fractographs of each specimen. In order to determine whether wavelength is a function of position on the specimen, fractographs were made for several specimens on the front, middle, rear, and edge. Values of λ showed no statistical variation with position. This combined with numerous visual observations in the SEM leads to the conclusion that ridge spacing is constant over the plane strain surface of a particular specimen.

Figure 26 is a plot of yield strength versus wavelength for 4340 and maraging 300 steels. Over the range of attainable σ_y and λ for 4340 the curve is linear. In maraging steel the data falls on a curve which suggests that λ changes little at high strength levels. The data from specimens aged at one temperature (427°C) is on a more or less continuous line. The commercial ageing treatment (438°C for 3 hr) does not fall on this line, and the overaged point (538°C for 24 hr) appears to lie to the left of it.

A graph of λ versus calculated COD for the two steels is presented in Figure 27. The data points for maraging 300 steel aged at 427°C fall on a straight line for an order of

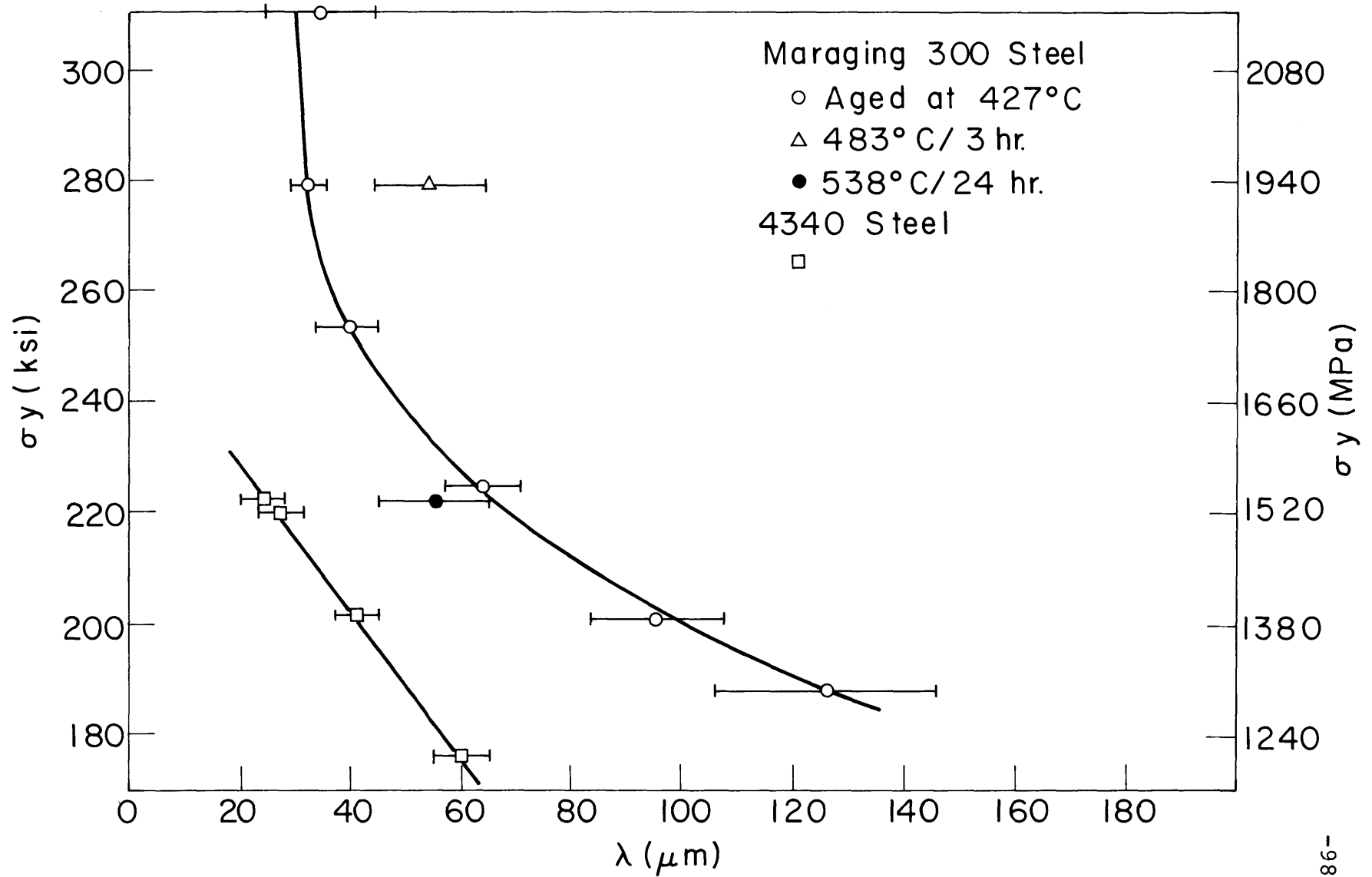


Figure 26 Yield strength versus ridge wavelength (λ) for 4340 and maraging 300 steels.

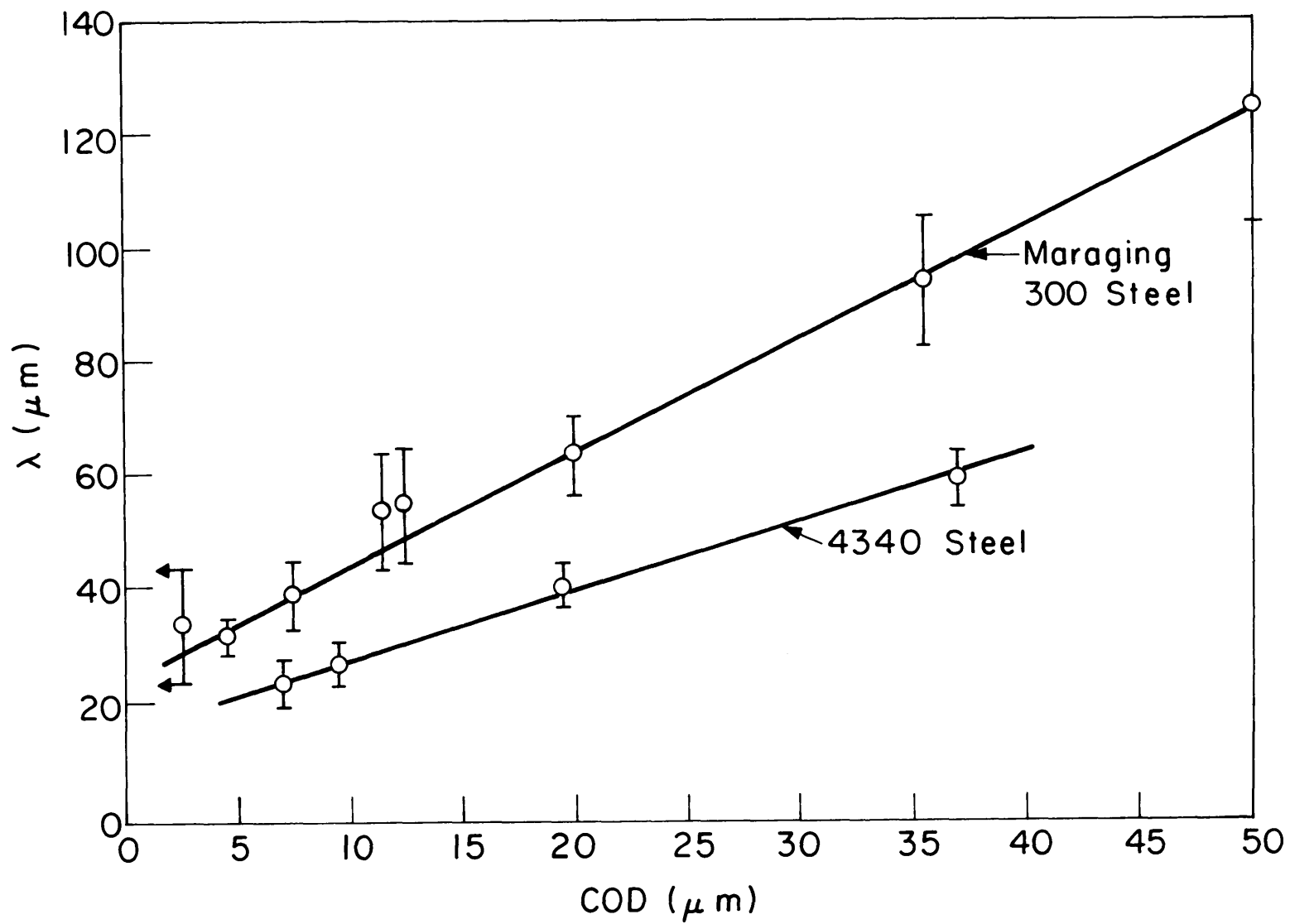


Figure 27 Ridge wavelength (λ) versus calculated COD for 4340 and maraging 300 steels.

magnitude spread in COD. Commercial aged and the overaged points are nearly equal and lie above the line. The curve for 4340 also appears linear within experimental accuracy.

A similar plot of λ versus calculated plastic zone size is given in Figure 28. Here the top scale r_p^x is the extent of the plastic zone directly in front of the crack, and r_p^y is the furthest extent above and below the crack plane. The curves in this case are not linear, although the values for maraging 300 steel once again lie above the 4340 data.

In Figure 29 the ridge spacing is plotted against K_{IC}^2 for both steels. Error bars for variation in K_{IC}^2 were obtained by assuming a $\pm 5\%$ experimental scatter in K_{IC} , which is reasonable for this type of testing. Both curves are linear over the range investigated. For maraging 300 steel, the commercial ageing treatment (483°C for 3 hr) falls on the same line as the low temperature aged specimens; the overaged specimen lies above the line, indicating a lower toughness at that wave length compared to the other treatments.

4.5.2 DETAILS OF RIDGE SHAPE FROM SECTIONED PROFILES AND

SEM OBSERVATIONS

The details of zig-zag shape and formation were studied both by stereo scanning electron microscopy and by sectioning epoxy-impregnated partially cracked fracture toughness specimens. The sectioning technique is useful to examine mating

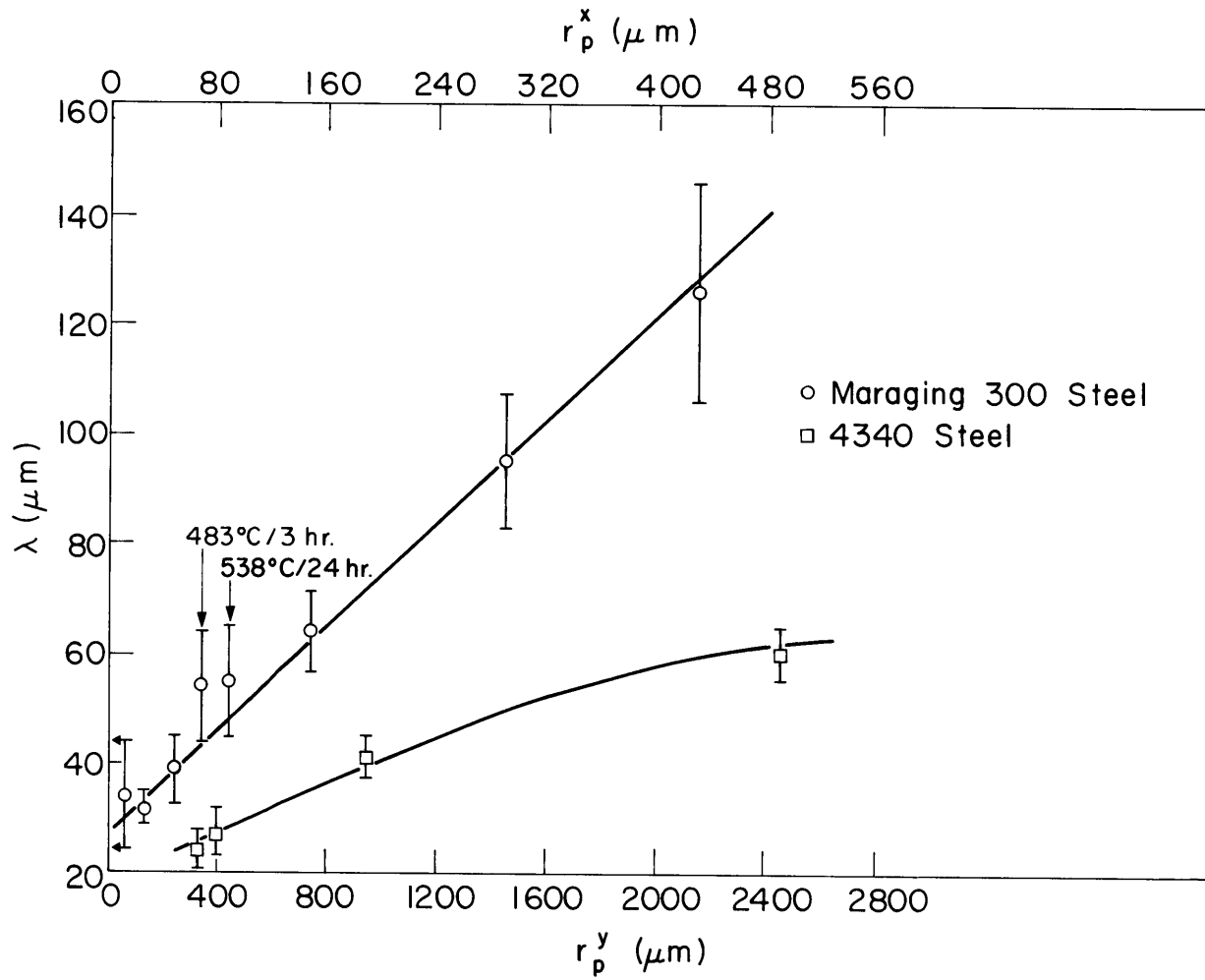


Figure 28 Ridge wavelength (λ) versus calculated r_p^x and r_p^y for 4340 and maraging 300 steels.

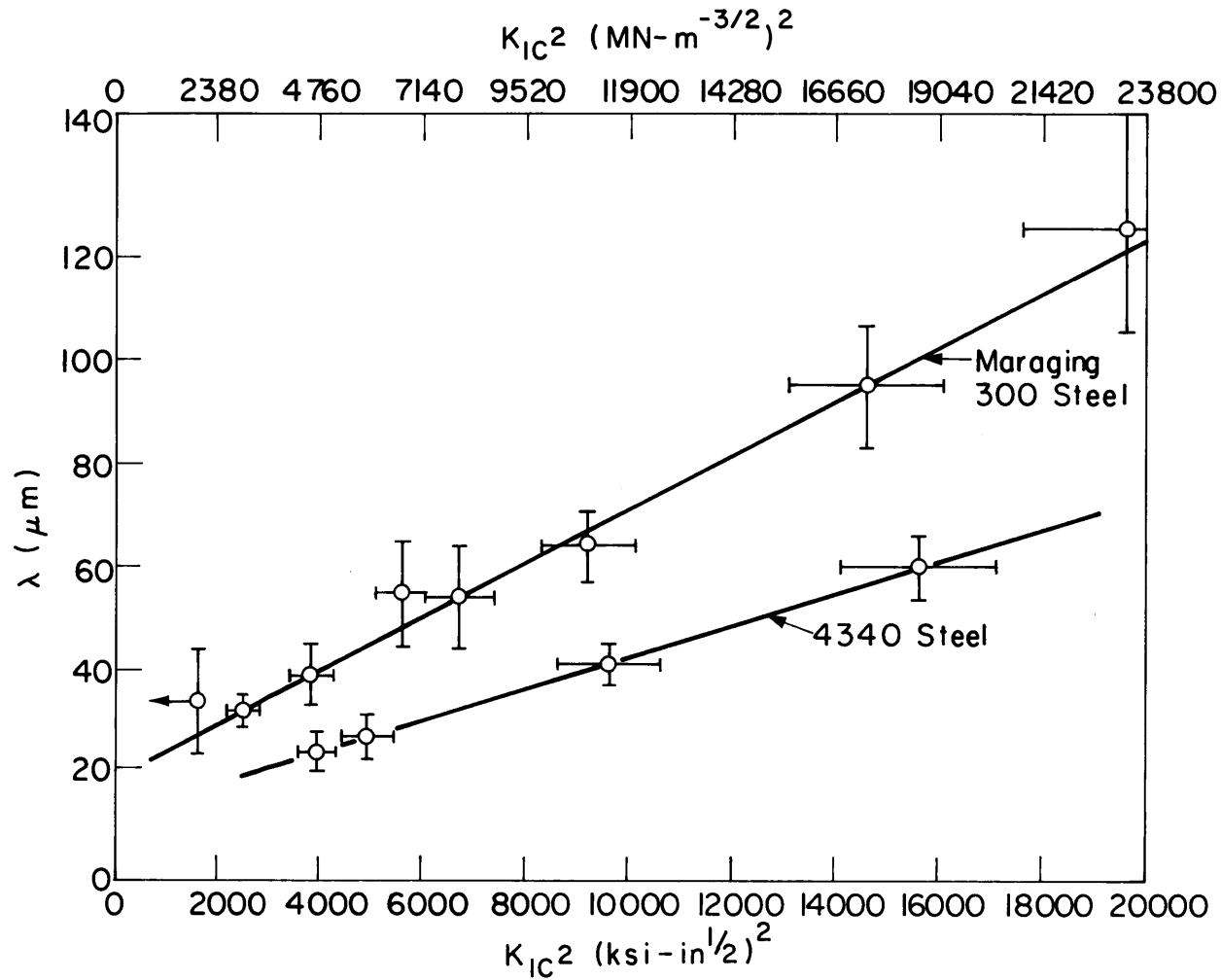
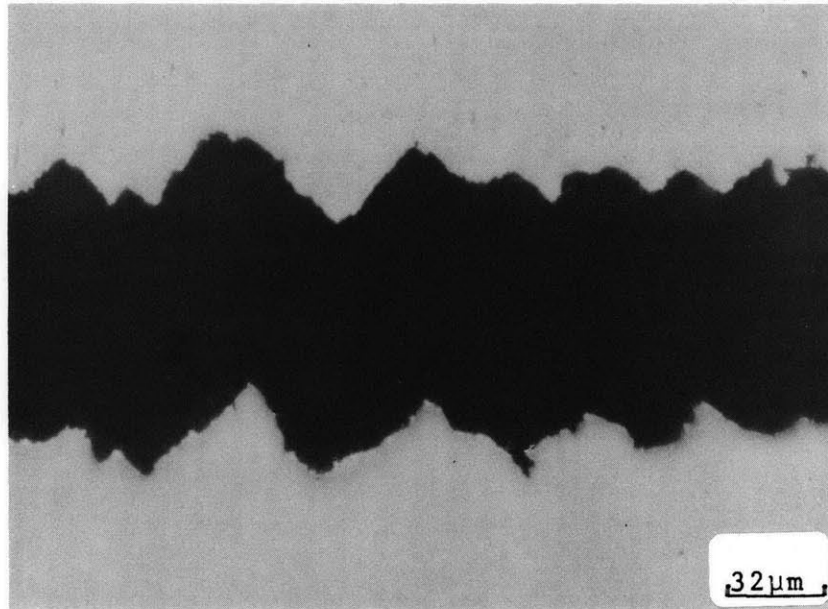


Figure 29 Ridge wavelength (λ) versus K_{IC}^2 for 4340 and maraging 300 steels.

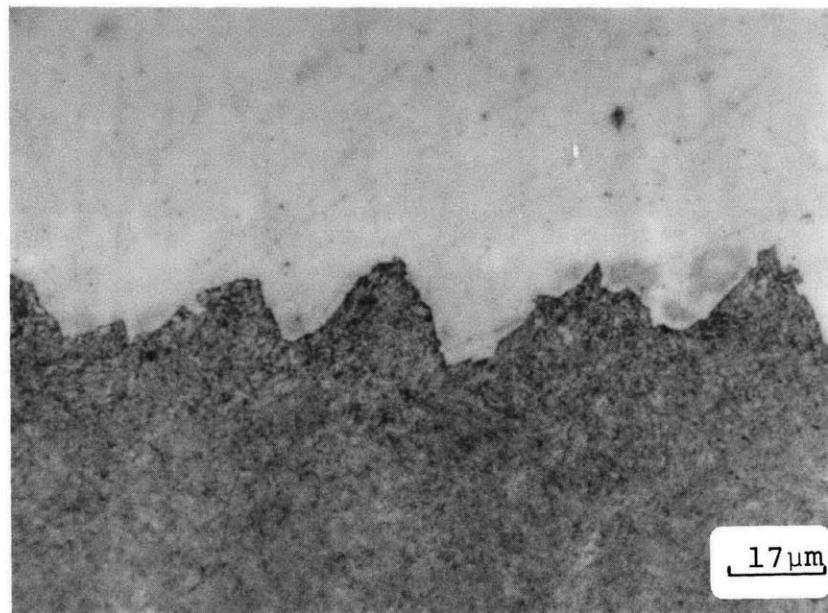
fracture surfaces and crack tip features. It is most successful if the distance between the surfaces is small: this minimizes rounding off edges and gives better match up of opposing features. It is important in this method to section the specimen accurately perpendicular to the crack plane since opposing features will otherwise not match up. The vacuum impregnation technique employed here was successful in forcing the epoxy to the very tip of the crack in all cases.

A sectioned crack in 4340 ($K_{IC} \approx 130 \text{ ksi-in}^{1/2}$ ($142 \text{ MN-m}^{-3/2}$), $\lambda = 60 \mu\text{m}$) is shown in Figure 30a; crack propagation is from right to left. Surface features are complementary; that is, peaks match valleys. A similar fracture surface showing zig-zags on 4340 is seen in Figure 30b, again crack growth is from right to left. The steel ($K_{IC} = 98 \text{ ksi-in}^{1/2}$ ($107 \text{ MN-m}^{-3/2}$), $\lambda = 40 \mu\text{m}$) is etched dark to show the martensitic structure, and the surface is plated with nickel (light) to improve edge retention for polishing.

For sectioned specimens such as these, it is usual to see only a few (2-5) well-formed ridges in a row followed by a length of irregular features. This occurs because the ridges have a length to spacing ratio of five or less, as previously mentioned. Looking, for example, at Figures 22 or 25, if one imagines a straight line drawn perpendicular to the ridge fronts (as in the case of these sectioned specimens), the line intersects only a few well-formed ridges at a time before it intersects a messy region.



(a)



(b)

Figure 30

Zig-zag profiles: (a) epoxy impregnated and wedged open fracture toughness specimen of 4340 steel ($K_{IC} \approx 130 \text{ ksi-in}^{1/2} / 142 \text{ MN-m}^{-3/2}$, $\lambda = 60 \pm 5 \mu\text{m}$); and (b) nickel plated fracture surface (etched) of fracture toughness specimen of 4340 steel ($K_{IC} = 98 \text{ ksi-in}^{1/2} / 107 \text{ MN-m}^{-3/2}$, $\lambda = 41 \pm 4 \mu\text{m}$). Propagation from right to left.

The great majority of well-formed ridges which were observed by sectioning in 4340 have sides which make angles on the average of $\pm 45^\circ$ with the macroscopic crack plane. This is somewhat at variance with the observations of Beachem and Yoder⁽³³⁾, who claimed the slopes of the ridge sides nearest the crack origin were less steep than the sides away from the origin ($36 \pm 10^\circ$ vs $52 \pm 9^\circ$). They measured these angles by tilting the specimen and observing changes in reflected light. The angles of $\pm 45^\circ$ do fall within their error band.

Beachem and Yoder⁽³⁴⁾ also claim as a rule that the peaks of ridges are sharp while the valleys are stretched out or blunted. These observations were based on studies of 13Cr-8Ni-2Mo steel fractured by hydrogen assisted cracking (HAC). Present observations do not support this as a general rule. While some instances of sharp peaks matching blunt valleys are seen (Figure 30A), there are also numerous examples of sharp valleys and blunt peaks (Figure 30b) or completely complementary peaks and valleys (Figure 31). An SEM view (Figure 33) of two ridges in 4340 ($K_{IC} \approx 130 \text{ ksi-in}^{-1/2}$ ($142 \text{ MN-m}^{-3/2}$), $\lambda = 60 \mu\text{m}$) shows that ridges may be alternatively sharp and blunt.

A sectioned crack tip wedged open under load in 4340 ($K_{IC} = 98 \text{ ksi-in}^{-1/2}$ ($107 \text{ MN-m}^{-3/2}$), $\lambda = 41 \mu\text{m}$) is presented in Figure 31. For this specimen the calculated COD = $20 \mu\text{m}$ and $r_p^X = 190 \mu\text{m}$. This figure shows features common to other

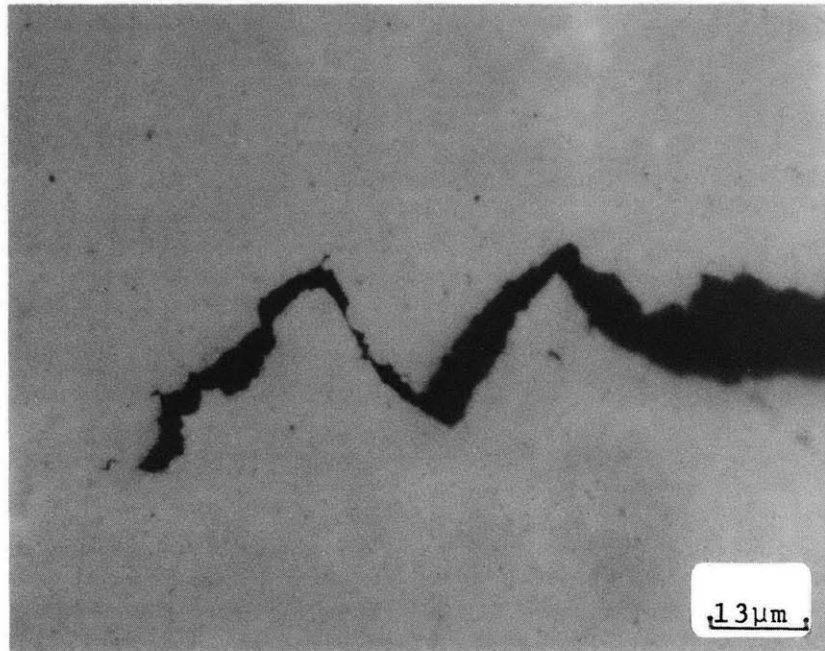


Figure 31 Sectioned tip of zig-zagging crack from wedged open 4340 steel fracture toughness specimen ($K_{IC} = 98 \text{ ksi-in}^{1/2} / 107 \text{ MN-m}^{-3/2}$, $\lambda = 41 \pm 4 \mu\text{m}$).

section crack tips for different toughness conditions of 4340:

- a) There are few, if any, voids nucleated ahead of the zig-zagging crack tip. Small, micron-sized voids may lie directly in front of the tip as in Figure 31; or as seen on other samples, a large void may form around a large inclusion located up to several wavelengths away from the tip. These large voids are observed above, below, or ahead of the tip, but are infrequently seen because the inclusion spacing ($300\mu\text{m}$) is large compared to the scale of the ridges.
- b) There is no formation of "cheezy" material directly in front of the tip as suggested by Berg⁽³²⁾.
- c) The observed COD near the tip is much less than the calculated COD based on assumed blunting⁽³⁾. Crack tips of sectioned zig-zagging cracks are generally sharp.

Figure 32 shows a section of the transition region between the fatigued zone and the fast fracture zone in a 4340 fracture toughness specimen ($K_{IC} = 98 \text{ ksi-in}^{1/2}$ ($107 \text{ MN-m}^{-3/2}$), $\lambda = 41\mu\text{m}$). The crack tip has apparently blunted, and a COD of approximately $10\mu\text{m}$ is measured by combining the depths of the two blunted halves. This measured COD is about one-half the calculated value of $20\mu\text{m}$. It is also evident that the crack begins to zig-zag immediately after the

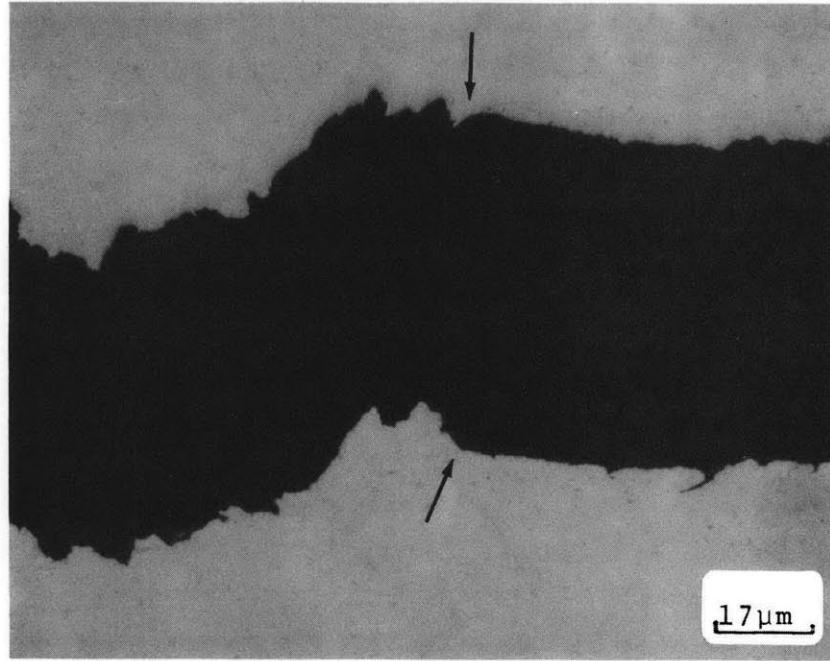


Figure 32 Sectioned profile of fatigue-fast fracture interface showing blunted crack tip. 4340 steel fracture toughness specimen ($K_{IC} = 98 \text{ ksi-in}^{1/2} / 107 \text{ MN-m}^{-3/2}$, $\lambda = 41 \pm 4 \mu\text{m}$). Arrows mark blunted tip.

initiation of fast fracture.

4.5.3 VOID SIZES ON RIDGE SIDES AND ON PLANE STRAIN
TENSILE SPECIMENS

Quantitative characterization of voids on the sides of ridges is difficult because there is a large range of void sizes, and the void shapes are quite irregular. Figures 33 and 34 show this for 4340 and maraging steels, respectively. Ridge side voids for the 4340 sample range from less than $1\mu\text{m}$ to $10\mu\text{m}$. Figure 35 gives a higher magnification view of a ridge side on the same sample shown in Figure 33. Dimples on maraging 300 also range in size from less than $1\mu\text{m}$ to about $20\mu\text{m}$ (Figures 34, 36a, b,). An average void size for these surfaces is not meaningful--a void size distribution measurement would be necessary to precisely measure changes in size with toughness. However, large changes in size distribution would be qualitatively visible on a series of fractographs.

With respect to dimple size on the sides of ridges, there appears to be no noticeable change of size distribution with toughness for either 4340 or maraging 300 steel. Examples of this are shown in Figures 35 and 36.

Figure 35 gives areas on ridge sides from two specimens which differ in K_{IC} by a factor of two (63 vs ≈ 130 $\text{ksi-in}^{1/2}$, 69 vs 142 $\text{MN-m}^{-3/2}$). Some larger voids are present, but the

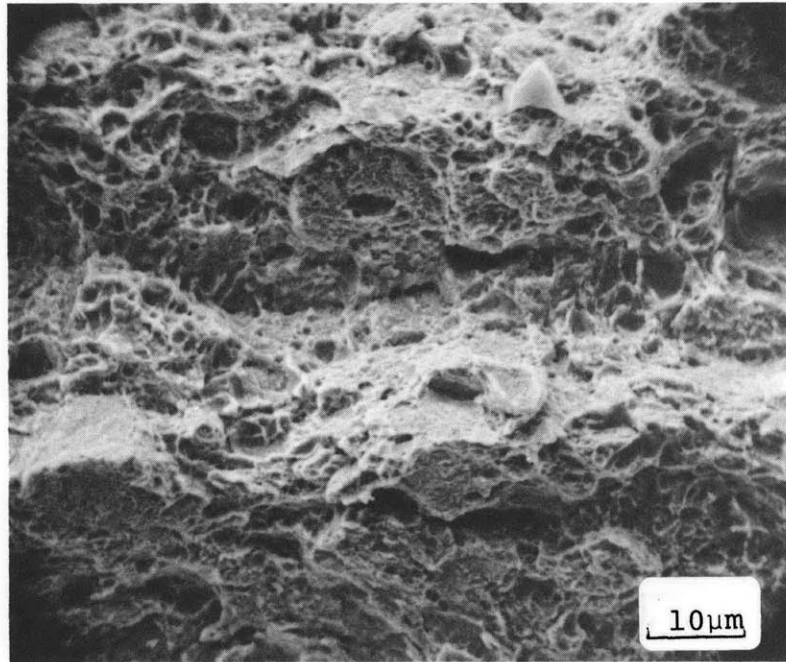


Figure 33 Two ridges adjoining a valley on the plane strain region of a fracture toughness specimen of 4340 steel ($K_{IC} \approx 130 \text{ ksi-in}^{1/2} / 142 \text{ MN-m}^{-3/2}$, $\lambda = 60 \pm 5 \mu\text{m}$). Zero degree tilt.

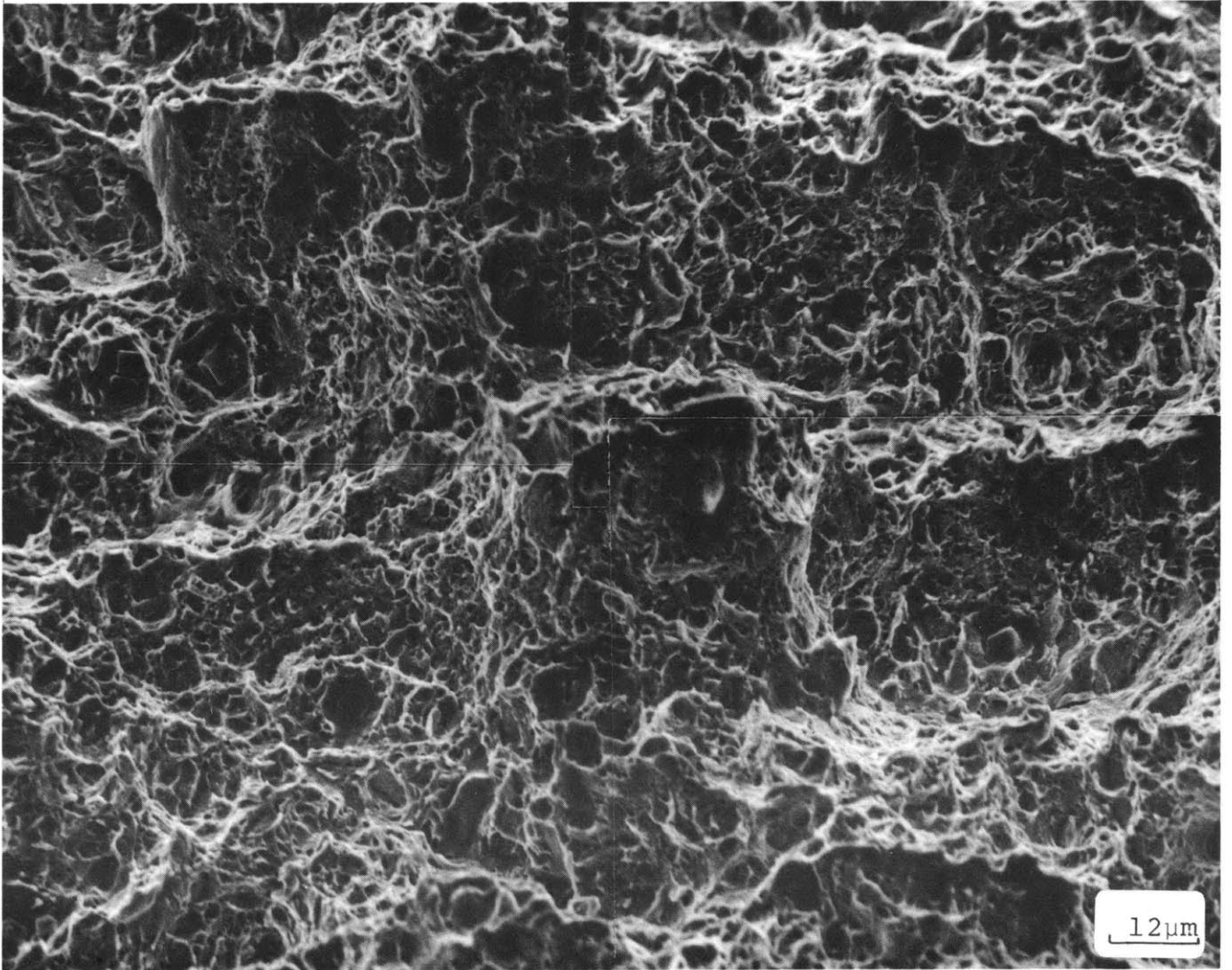
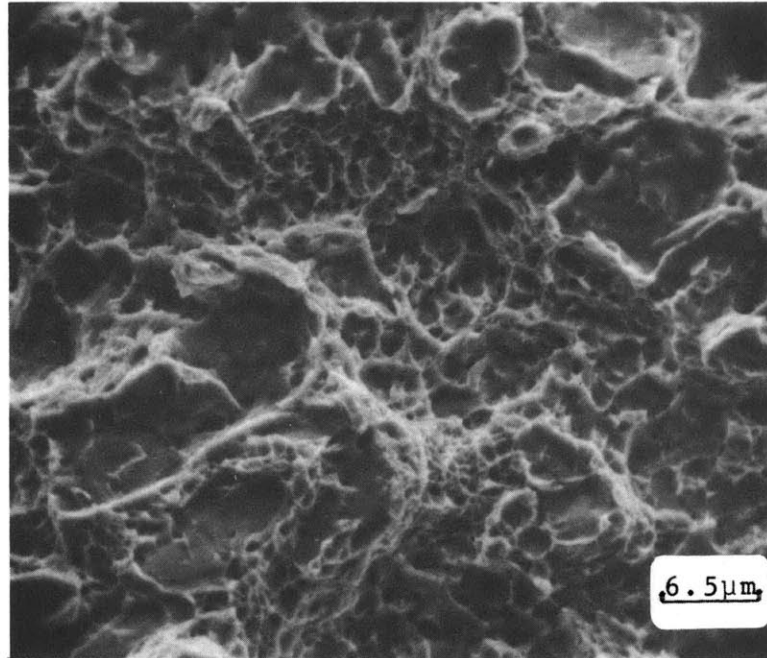
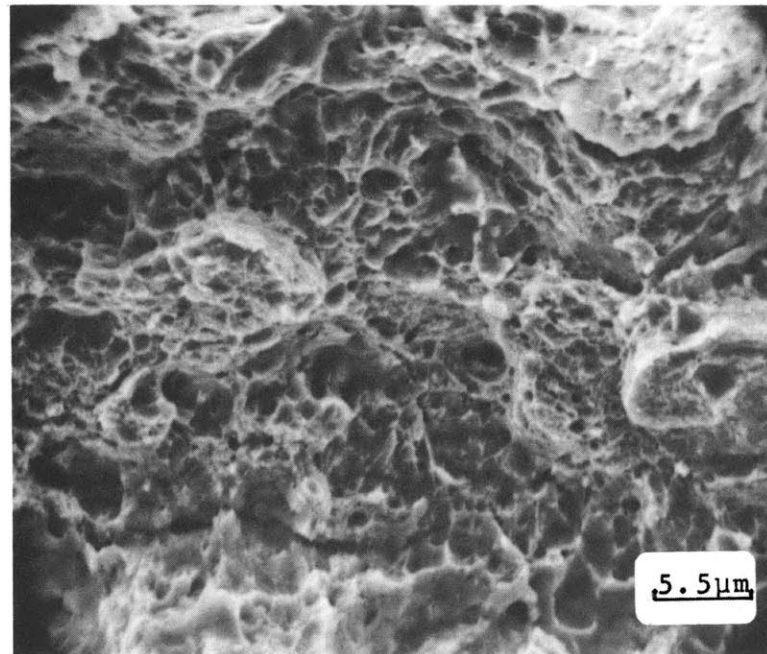


Figure 34 Several ridges on the plane strain region of a fracture toughness specimen of maraging 300 steel ($K_{IC} = 82 \text{ ksi-in}^{1/2} / 89 \text{ MN-m}^{-3/2}$, $\lambda = 54 \pm 10 \mu\text{m}$). Zero degree tilt.



(a)



(b)

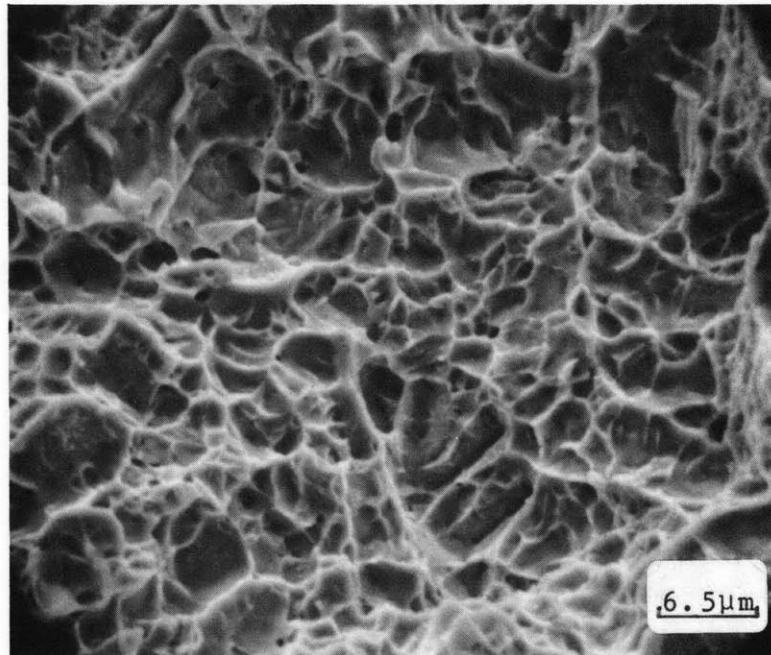
Figure 35

High magnification view of voids on the sides of ridges of fracture toughness specimens of 4340 steel: (a) $K_{IC} = 63 \text{ ksi-in}^{1/2} / 69 \text{ MN-m}^{-3/2}$, $\lambda = 24 \pm 4 \mu\text{m}$; (b) $K_{IC} \approx 130 \text{ ksi-in}^{1/2} / 142 \text{ MN-m}^{-3/2}$, $\lambda = 60 \pm 5 \mu\text{m}$.

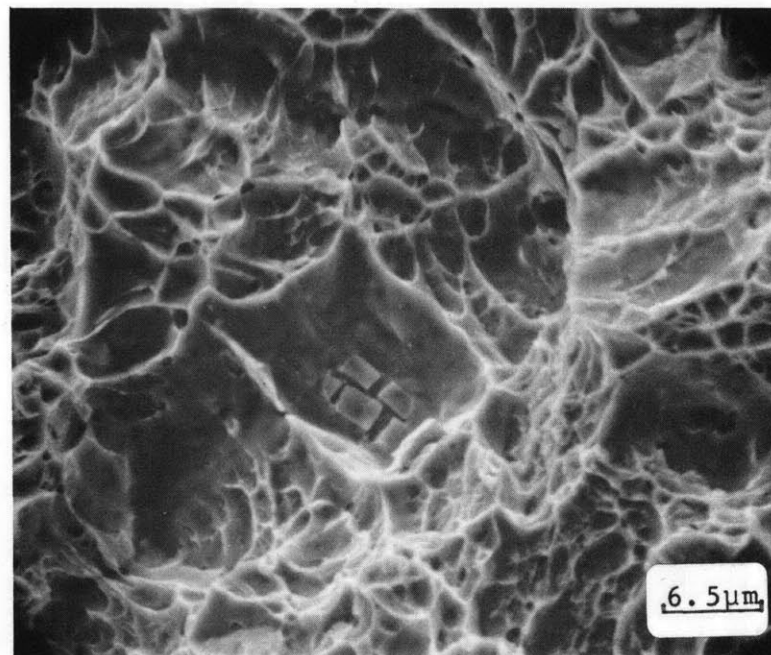
greatest number of voids average one micron or less in size for both samples. Dimples on ridges of maraging 300 are larger (Figure 36a, b), ranging between 1 and 5 μ m. K_{IC} changes by approximately a factor of three between these two tests. A large (10 μ m) void which nucleated around a 5 μ m inclusion is seen in Figure 36; several of these are also seen on Figure 34. For each pair of fractographs discussed, there is no visible large change in distribution of void sizes.

Observations of fracture surfaces from plane strain tensile tests also support the finding that ridge void sizes do not change significantly with toughness.

Plane strain specimens all fail by shear at 45^o to the tensile axis. Fracture surfaces produced are similar to the surfaces of shear lips produced on smooth bar tensile tests and fracture toughness specimens. SEM fractographs of two toughness levels for 4340 steel are shown in Figure 37. The higher toughness samples show increased roughness and plasticity, but the void sizes are similar, less than 1 μ m in size. The shear dimples formed in the maraging steel (Figure 38a, b) are much larger, 1 μ m to 5 μ m, but no real difference is seen between the two toughness levels. Figures 38a and b were purposely taken to include the large voids; the overall fracture surfaces are better represented by the small void distribution.



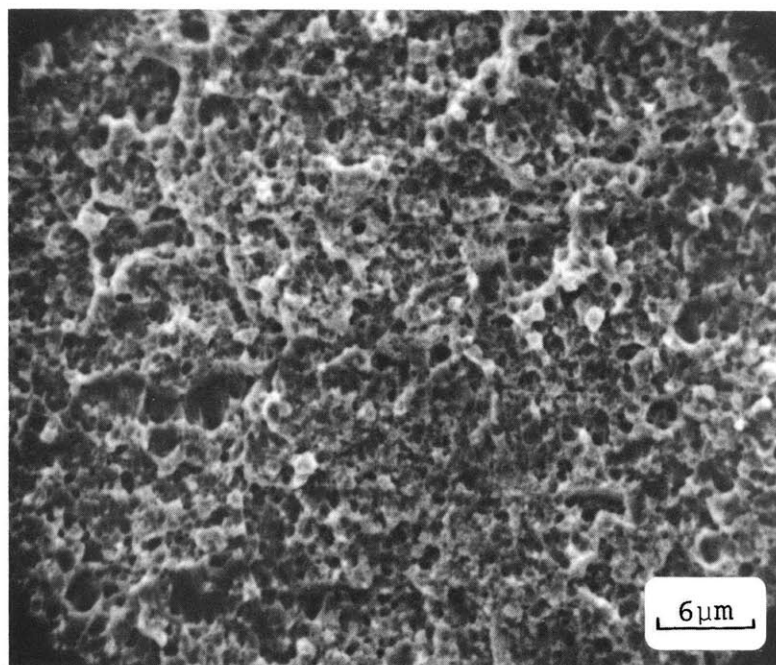
(a)



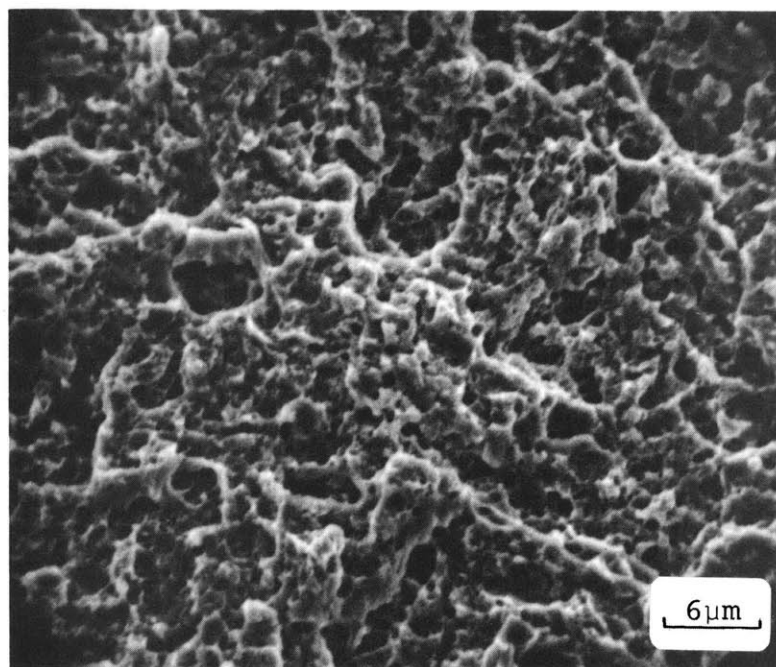
(b)

Figure 36

High magnification view of voids on the sides of ridges of fracture toughness specimens of maraging 300 steel: (a) $K_{IC} < 40 \text{ ksi-in}^{1/2} / < 44 \text{ MN-m}^{-3/2}$, $\lambda = 34 \pm 10 \mu\text{m}$; (b) $K_Q \approx 140 \text{ ksi-in}^{1/2} / 153 \text{ MN-m}^{-3/2}$, $\lambda = 126 \pm 20 \mu\text{m}$.



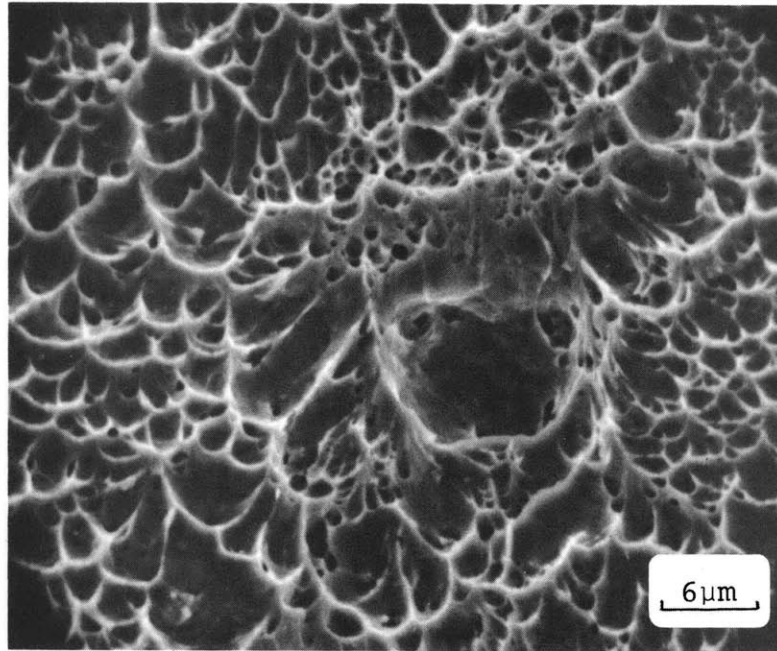
(a)



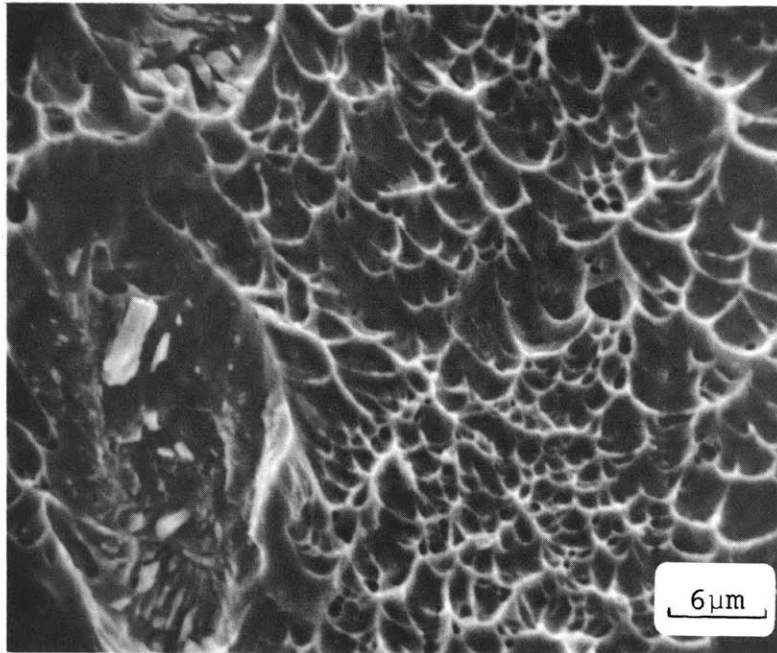
(b)

Figure 37

High magnification view of voids on the fracture surface of plane strain tensile specimens of 4340 steel: (a) tempered 270°C for 1 hr, $K_{IC} = 63 \text{ ksi-in}^{1/2} / 69 \text{ MN-m}^{-3/2}$; (b) tempered 510°C for 1 hr, $K_{IC} \approx 130 \text{ ksi-in}^{1/2} / 142 \text{ MN-m}^{-3/2}$. Zero degree tilt.



(a)



(b)

Figure 38

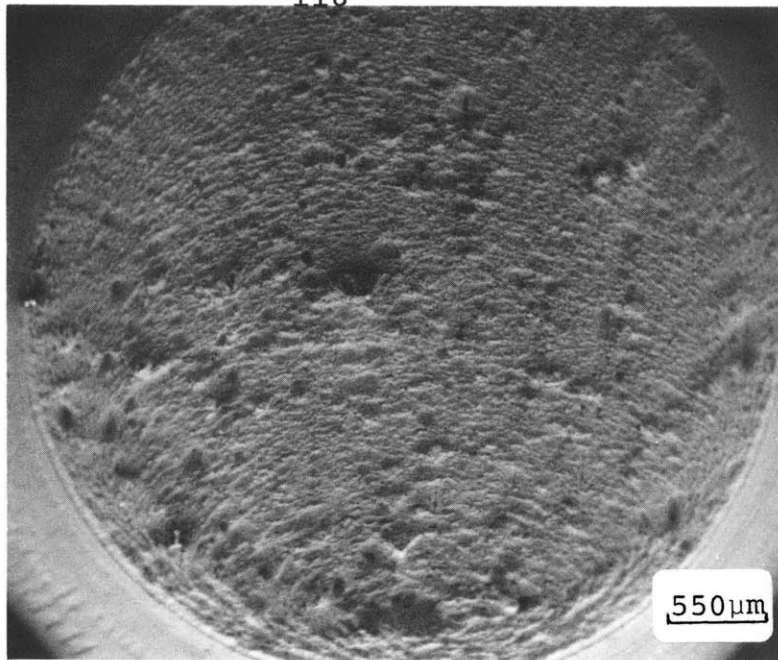
High magnification view of voids on the fracture surface of plane strain tensile specimens of maraging 300 steel: (a) aged 427°C for 1.5 hr; $K_{IC} = 121 \text{ ksi-in}^{1/2} / 132 \text{ MN-m}^{-3/2}$; (b) aged 427°C for 8 hr; $K_{IC} = 62 \text{ ksi-in}^{1/2} / 68 \text{ MN-m}^{-3/2}$. Zero degree tilt.

4.5.4 RIDGES ON 4340 NOTCHED TENSILE SPECIMENS

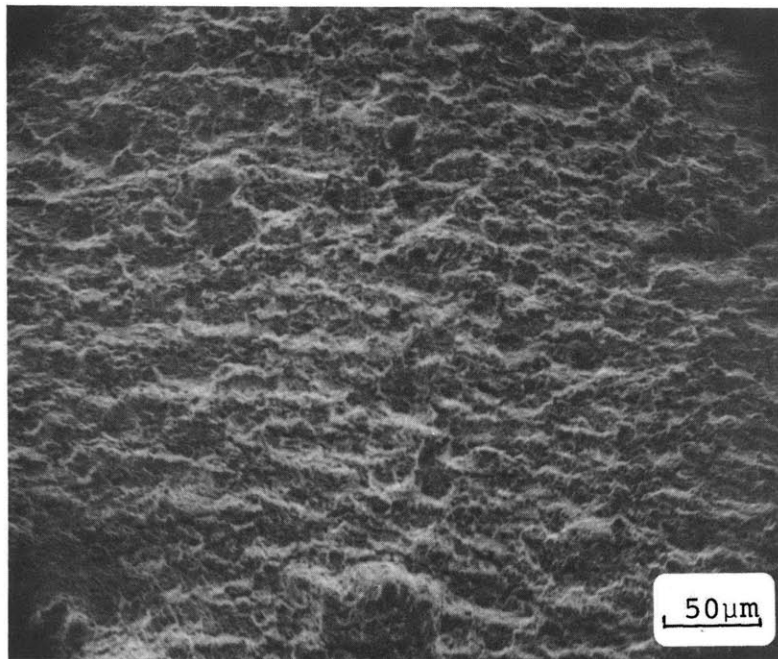
Ridges were observed on the fracture surfaces of 4340 steel notched tensile specimens. Figure 39 shows that fracture initiates below the root of the notch, and successive positions of the crack front are marked by the ridges. No shear lip is present on these specimens, but the zig-zags do curve around to become parallel to the notch edge, much as they became tangential to the shear lip in fracture toughness specimens. Many large dimples are present on the surface of Figure 39a; their spacing roughly corresponds to the spacing of large inclusions in the alloy (300 μ m).

The ridges formed in these notched tests have the same overall appearance as those on the fracture toughness specimens. Figure 39b gives a higher magnification view of a sample tempered to a K_{IC} of 98 ksi-in^{1/2}, (107 MN-m^{-3/2}). General observations suggest that zig-zags on these specimens are less well formed; that is, the ratio of continuous ridge length-to-spacing is lower. Measurements of this wavelength (λ_{NTS}) for the three toughness levels (Table 8) also show that λ_{NTS} is less at all three toughness levels than λ measured from fracture toughness specimens. Values of λ_{NTS} range from 0.5 to 0.6 of their respective λ counterparts.

Table 8 also compares notched test fracture stresses (σ_f^{NTS}) to round bar tensile test fracture stresses (σ_f , uncorrected for triaxiality). Measured notched fracture



(a)



(b)

Figure 39

Ridges on fracture surfaces of 4340 steel notched tensile specimens:

(a) tempered 510°C for 1 hr, $K_{IC} \approx 130 \text{ ksi-in}^{1/2} / 142 \text{ MN-m}^{-3/2}$, $\lambda = 40 \pm 10 \mu\text{m}$; (b) tempered 427°C for 1 hr, $K_{IC} = 98 \text{ ksi-in}^{1/2} / 107 \text{ MN-m}^{-3/2}$, $\lambda = 20 \pm 5 \mu\text{m}$.

TABLE 8 NOTCHED TENSILE TEST PROPERTIES OF 4340 STEEL

Tempering Treatment	σ_y^{AXI} ksi (MPa)	K_{IC} ksi-in ^{1/2} (MN-m ^{-3/2})	λ μm	λ_{NTS} μm	σ_f^{NTS} ksi (MPa)	σ_f ksi (MPa)
316°C/1 hr.	220 (1520)	70 (76)	27±4	16±5	308 (2130)	345 (2380)
427°C/1 hr.	202 (1390)	98 (107)	41±4	20±5	291 (2010)	308 (2120)
510°C/1 hr.	176 (1210)	≈130 (142)	60±5	40±10	263 (1820)	275 (1900)

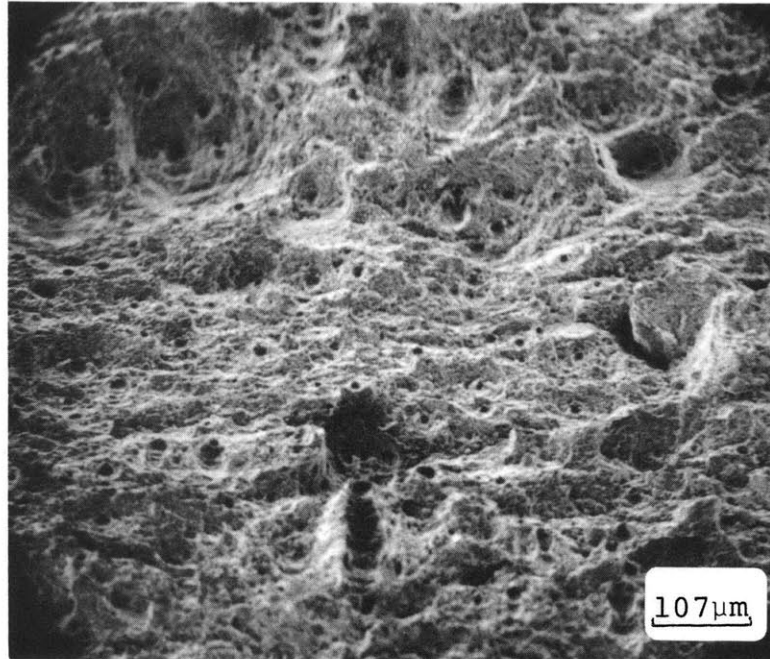
stress decreases with decreasing yield strength as does the round bar σ_f data. Values of σ_f^{NTS} are 4 to 11 percent less than the respective σ_f .

4.5.5 FRACTURE SURFACES OF 4340 CHARPY IMPACT SPECIMENS

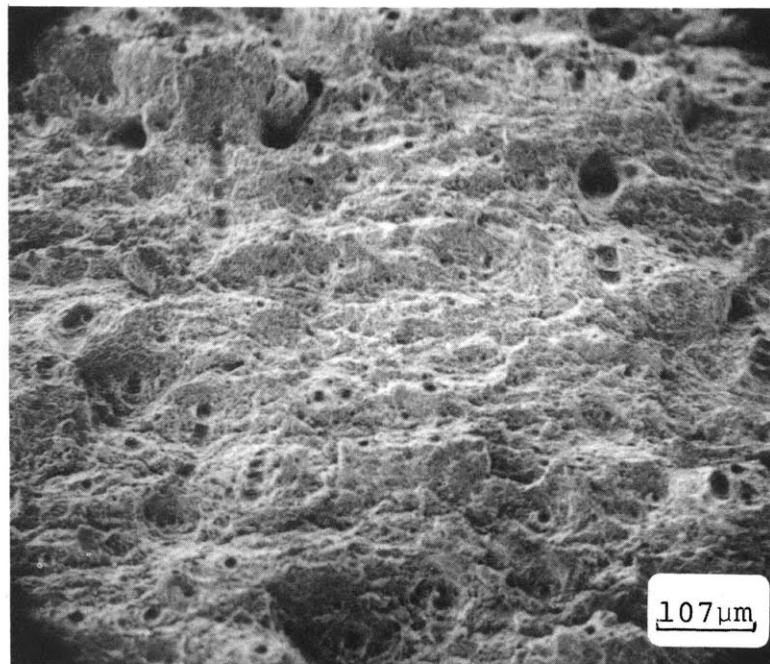
Fracture surfaces of 4340 Charpy impact specimens show a tendency for ridge formation, but they are very irregular in shape and spacing. Figures 40a and b show ridges on two toughness level specimens; crack propagation is from top to bottom. Numerous large voids are present on the surfaces of both specimens. No quantitative measurement of ridge spacing was attempted.

4.5.6 FRACTURE SURFACES OF THE ALUMINUM ALLOYS

Plane strain fracture surfaces from toughness specimens of 7075-T6, 2024-T4 aluminum alloys do not show well defined ridge formation. The surfaces of both (Figures 41 and 42) alloys are very rough and contain a large number of peaks and holes. At higher magnification (Figure 41b), the majority of the fracture surface consists of large dimples, approximately 20 μ m wide, which form around inclusions. Sheared off areas also occur between large voids which are on different levels above or below the mean fracture surface. These sheared areas consist of fine 1 to 2 μ m voids. These observations are true for 2024-T4 and 7075-T6.



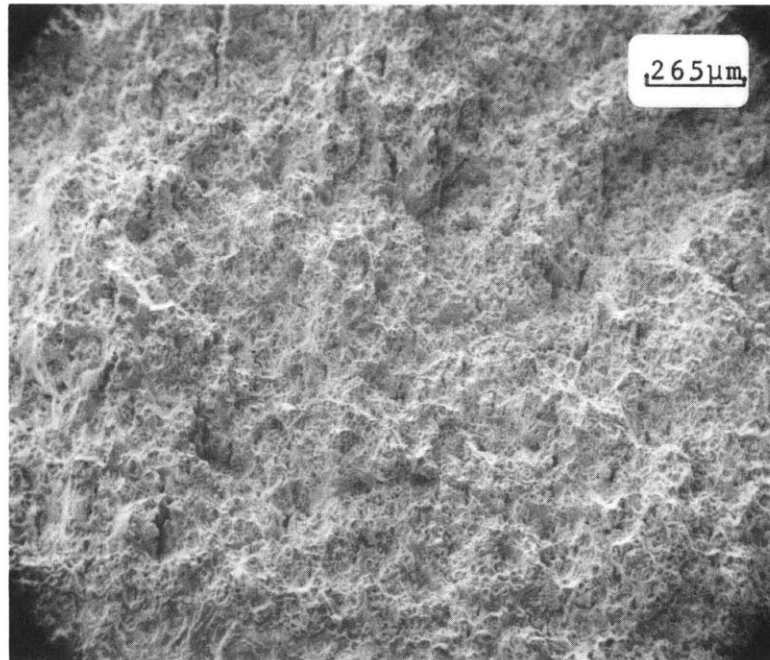
(a)



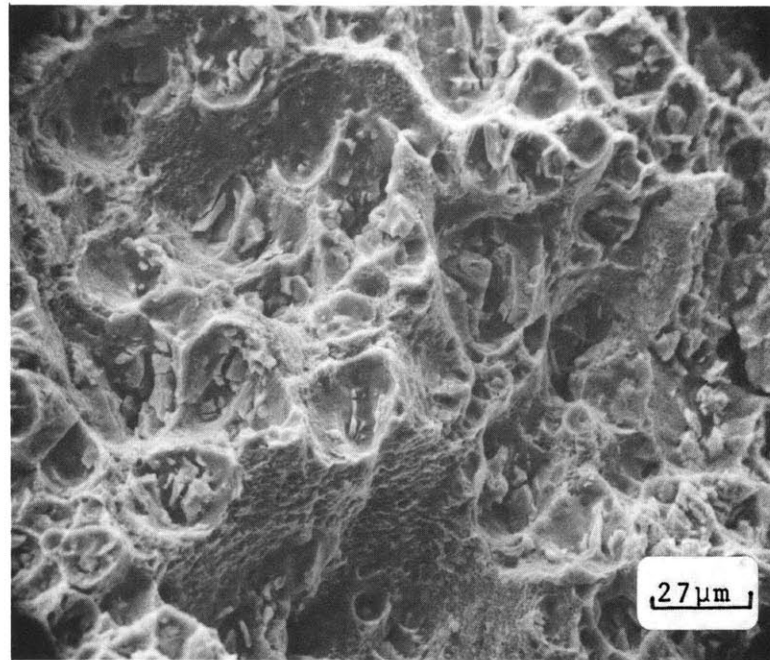
(b)

Figure 40

Ridges on fracture surfaces of charpy impact specimens of 4340 steel. Crack propagation top to bottom. (a) tempered 316°C for 1 hr; (b) tempered 427°C for 1 hr. Both tilted 45° .



(a)



(b)

Figure 41

Plane strain fracture surface of 2024-T4 aluminum fracture toughness specimen: (a) low magnification showing delamination parallel to crack propagation direction (bottom to top); (b) high magnification showing large number of large voids and associated inclusions. Zero degree tilt.

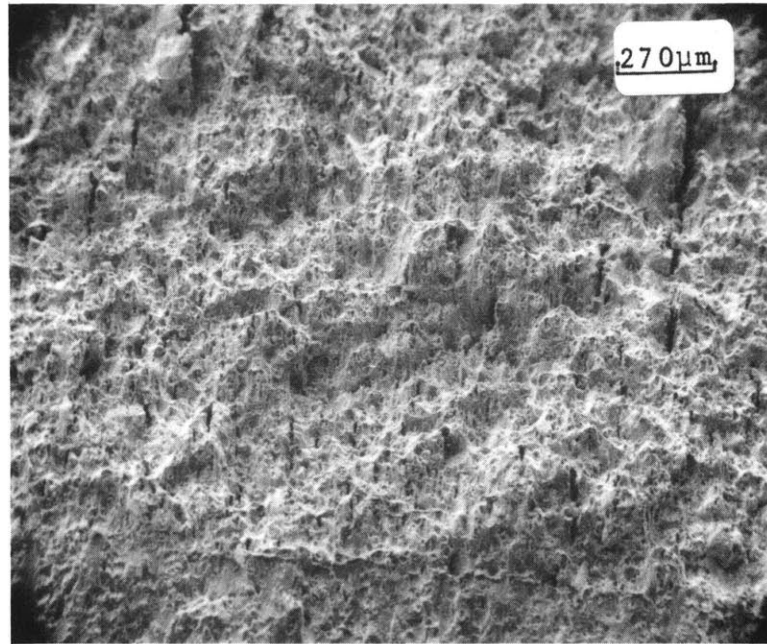


Figure 42 Plane strain surface of 7075-T6 aluminum fracture toughness specimen showing delaminations parallel to crack growth (bottom to top). Zero degree tilt.

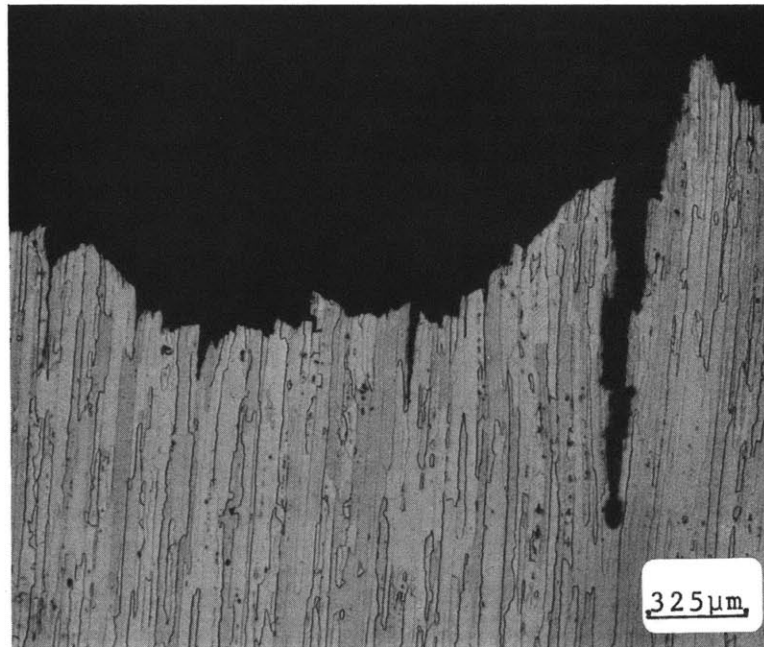


Figure 43 Polished and etched section of plane strain fracture surface of 7475-T651 aluminum. Propagation perpendicular to page (Keller's etch).

Crack propagation in Figures 41 and 42 is from bottom to top; the lines between the fatigued and fast fracture regions are visible at the bottoms of Figures 41 and 42. Another fracture feature common to the three alloys is cracks which occur parallel to the crack propagation direction. These are evident in Figures 41 and 42. Scanning electron microscope observations and sectioning of fractured specimens show these fissures to be delaminations along grain boundaries. Figure 43 shows a sectioned sample of 7475-T561; crack propagation is perpendicular to the page. This delamination is least severe in 2024-T4 and is much more prevalent in 7475-T651 than in 7075-T6. The majority of the fracture surface of 7475-T651 consists of sheared-off regions between grain boundary cracks. These have the appearance of many small shear lips on the nominally plane strain surface. As shown in Figure 43, the cracks can extend to over 1000 μ m below the surface; this is on the order of twice the calculated maximum plastic zone size in the y direction (\approx 650 μ m) for this material.

4.5.7 SHEAR LIP MEASUREMENTS ON TOUGHNESS SPECIMENS

Shear lip widths on the surfaces of fracture toughness specimens of the two steels were measured as outlined in section 3.2.3. Average shear lip sizes (SL) are given in Table 7. Shear lips in these specimens typically start out

small at the fatigue-ductile fracture interface and grow to a "steady state" size; it is this size which was measured. Values of SL are accurate to $\pm 10\%$ due to variations in width along the specimen and not due to precision of the measuring technique.

Since the size of shear lips is often used as an indication of the plastic zone size, values of shear lip width and plastic zone size are plotted in Figure 44. All of the data for the steels lie above the line $SL = r_p^Y$. There is considerable scatter, but it appears as a rule that the shear lip width is 1.5 to 2 times the size of the plane strain plastic zone in the y direction.

Figure 45 shows that the relationship between SL and λ is more continuous. Data points for 4340 and maraging 300 steels fall on respective curves. For the maraging samples aged at 427°C the curve is very approximately linear. The data point for the commercial treatment (483°C for 3 hr) falls well below this line. Data for 4340 show upward curvature.

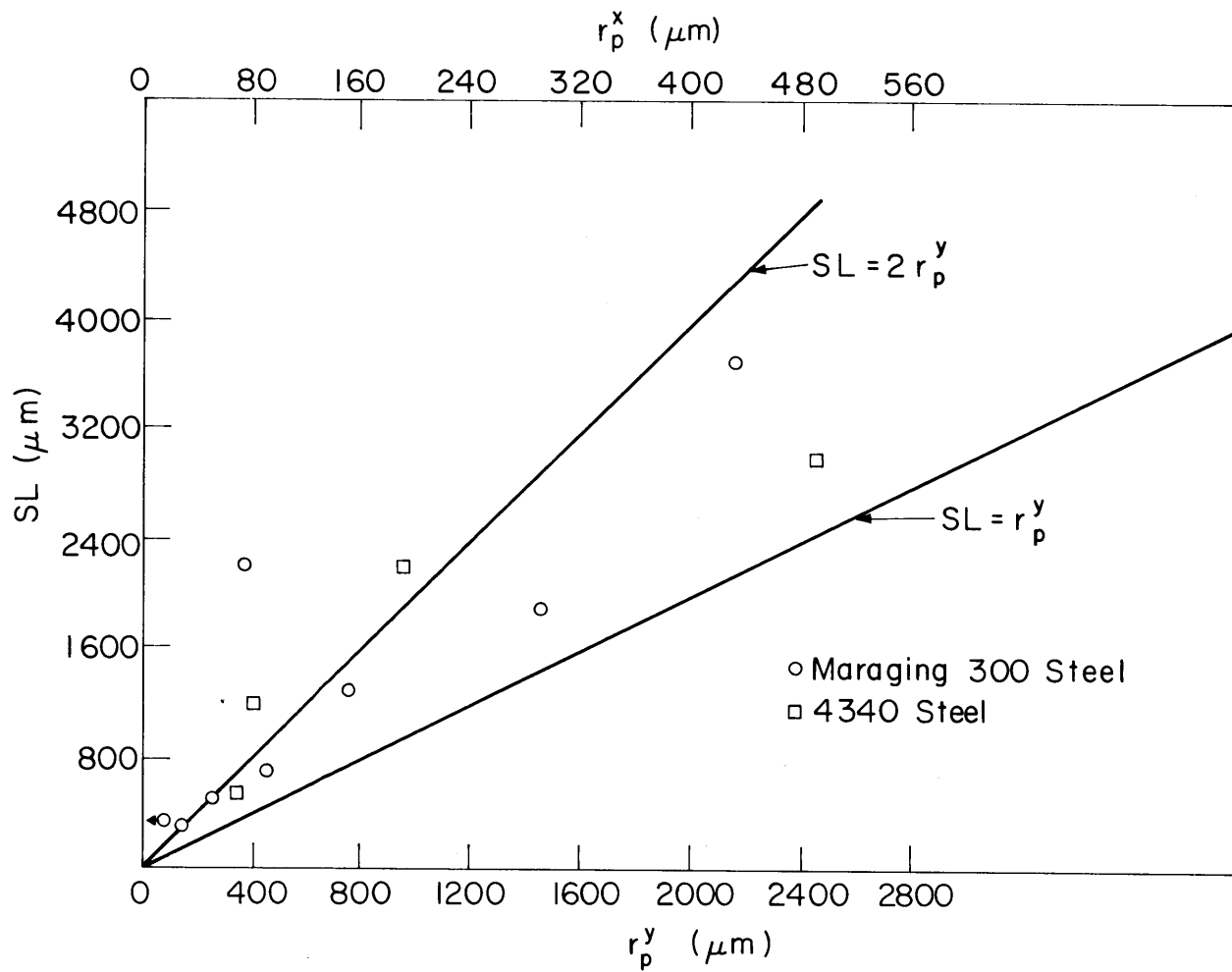


Figure 44 Shear lip widths (SL) versus plastic zone size, r_p^y and r_p^x , for 4340 and maraging 300 steels.

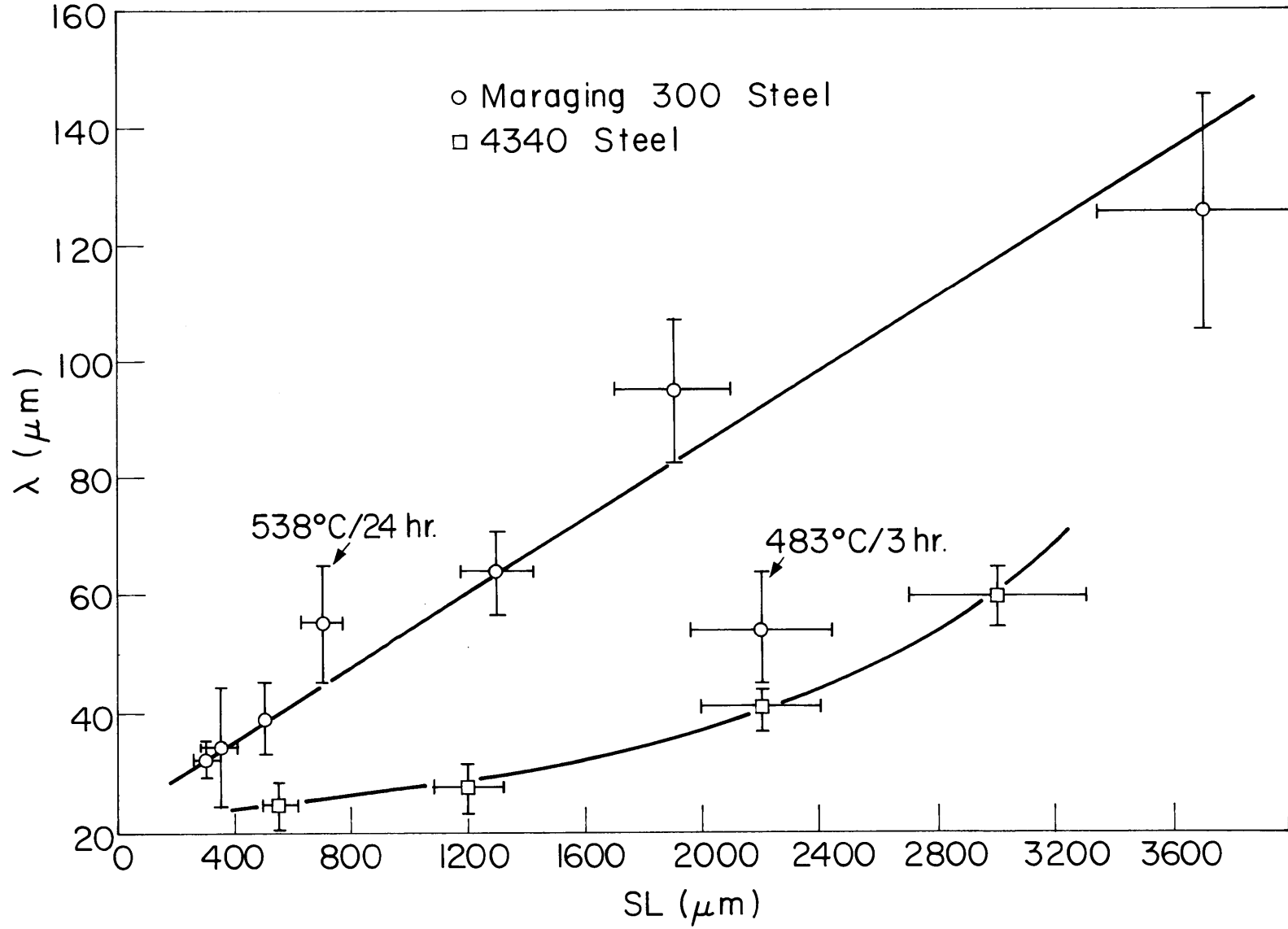


Figure 45 Shear lip widths (SL) versus ridge spacing (λ) for 4340 and maraging 300 steels.

CHAPTER V: DISCUSSION

5.1 RELATION OF TENSILE PROPERTIES TO FRACTURE TOUGHNESS

A close examination of both axisymmetric and plane strain tensile data shows the difficulty in modeling and calculating K_{IC} purely on the basis of tensile test results. In the relationship proposed by Hahn and Rosenfield^(22,23),

$$K_{IC} = \left[\frac{2}{3} E \sigma_Y \epsilon_f^n \right]^{1/2} \quad \text{Eq. 11}$$

the product ϵ_f^n must increase more than σ_Y decreases in order to observe an increase in K_{IC} with decreasing σ_Y .

Data for 4340 steel in Tables 5,6 and 7 show that ϵ_f is essentially independent of K_{IC} for both round bar and plane strain tensile tests. There is no significant difference in n values between the axisymmetric and plane strain tests at equivalent strength levels. Work hardening exponent values tend to decrease with increasing K_{IC} for 4340. Thus, ϵ_f^n decreases instead of increasing with lower σ_Y and the K_{IC} values of 4340 are not at all well-described by Eq. 11; Jones and Brown⁽⁶³⁾ reached this same conclusion for similar testing of 4340 steel.

For maraging 300 steel, ϵ_f does increase with K_{IC} for the axisymmetric and plane strain tensile tests for specimens aged at 427°C. Again plane strain and round bar n values are

essentially equivalent, but n does not increase systematically with K_{IC} . The Hahn and Rosenfield relationship (Eq. 11) does not work for this alloy either: for the 427°C ageing sequences a 40% decrease in σ_y is accompanied by a 50% increase in $\epsilon_f n^2$, but K_{IC} increases 200%.

Comparison of the axisymmetric tensile properties of maraging 300 steel specimens aged at 483°C and 538°C (Table 5) to the properties at 427°C shows that wide variations in K_{IC} can exist at equivalent yield strengths within a given alloy. The 483°C for 3 hrs. treatment has the same yield strength as the 427°C for 15.5 hrs. ageing treatment (279/1920 ksi/MPa), yet their respective K_{IC} values are 89 vs 54 MN-m^{-3/2}. The increase in toughness of the 483°C for 3 hrs. treatment has been attributed by Rack and Kalish⁽⁶¹⁾ to a change in slip mode from planar to wavy slip caused by formation of a different type of precipitate. The toughness of the overageing sequence (538°C for 24 hrs) is lower (82 vs 105 MN-m^{-3/2}) than its equivalent yield strength (427°C for 3 hrs) treatment.

These examples show that it is impossible to model the fracture process at a crack tip by assuming that the near tip material can be treated as a miniature tensile specimen. The stress and strain distributions in the plastic zone are very different from those formed in either a round bar specimen or a plane strain tensile specimen of the type used here.

Also, these simplistic theories do not account for the differences in near tip metallurgical structures or the size scales of these structures in relation to the plastic zone.

5.2 CRACK PROPAGATION AND FRACTURE TOUGHNESS

In order to understand fracture toughness it is important to examine the relative sizes and scales of microstructural and fractographic features for each material and compare them to the calculated crack tip opening displacements and plastic zone sizes. These comparisons can help to qualitatively explain the differences in fracture features between steels and aluminum alloys and it can also lead to the characterization of the structural factors which control toughness.

Figures 46-48 are schematic on-scale drawings of the plastic zone around the crack tip for the alloys studied here showing the COD, two dimensional spacing of large ($>1\mu\text{m}$) inclusions, and zig-zag formation where applicable. For all cases, it is assumed that the pre-existing fatigue crack tip blunts before the tear crack propagates. Figures 46 and 47 modeling the two steels show crack advance by zig-zagging over an arbitrary distance equal to $0.5 r_p^X$; the initial plastic zone formed as the crack blunted for the two steels is represented by a dashed line.

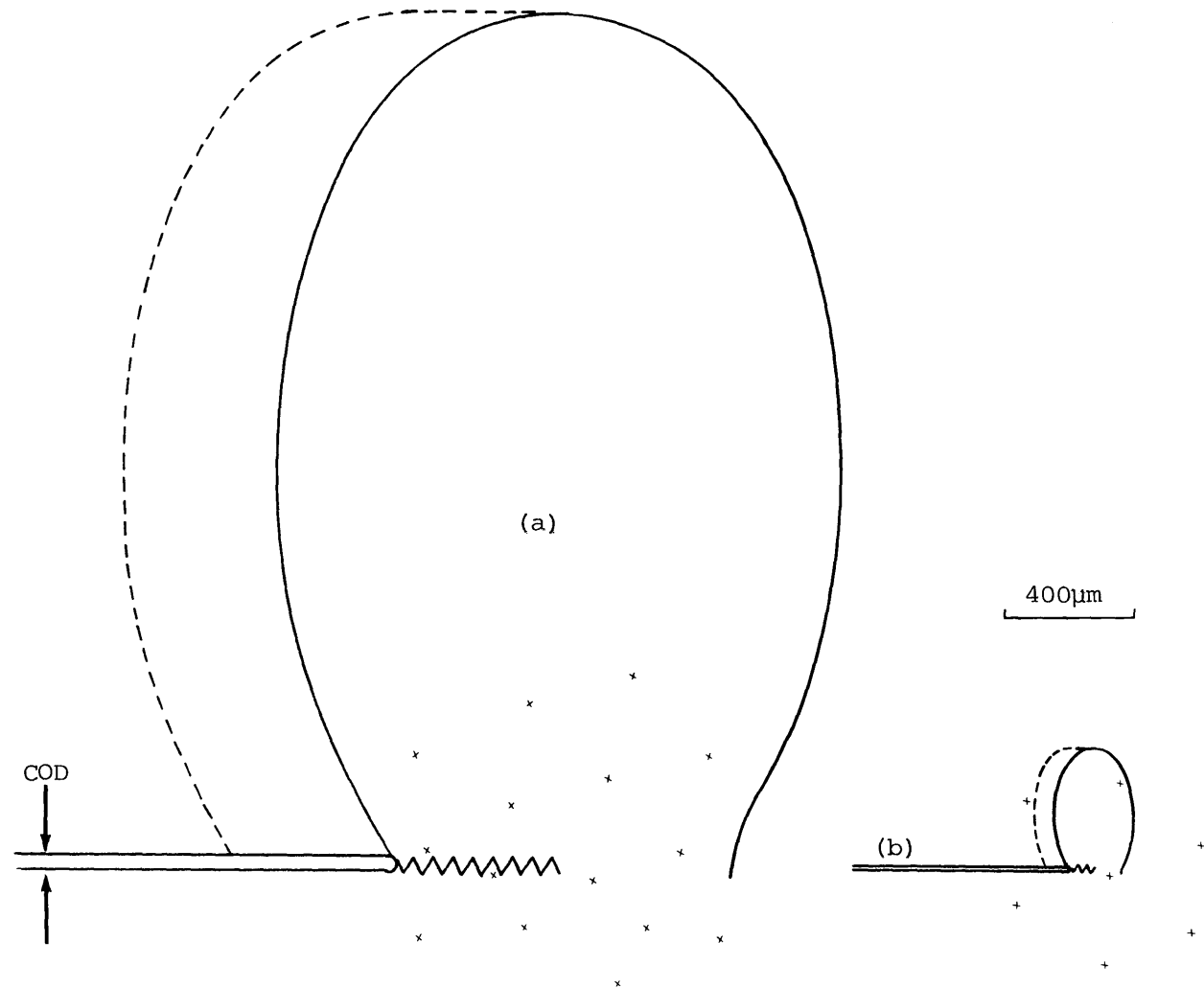


Figure 46 On-scale schematic drawings of calculated plastic zones and crack opening displacements, zig-zags, and 2D large inclusion spacing for two toughness levels of 4340 steel:
 (a) $K_{IC} \approx 130 \text{ ksi-in}^{1/2} / 142 \text{ MN-m}^{-3/2}$; (b) $K_{IC} = 63 \text{ ksi-in}^{1/2} / 69 \text{ MN-m}^{-3/2}$.

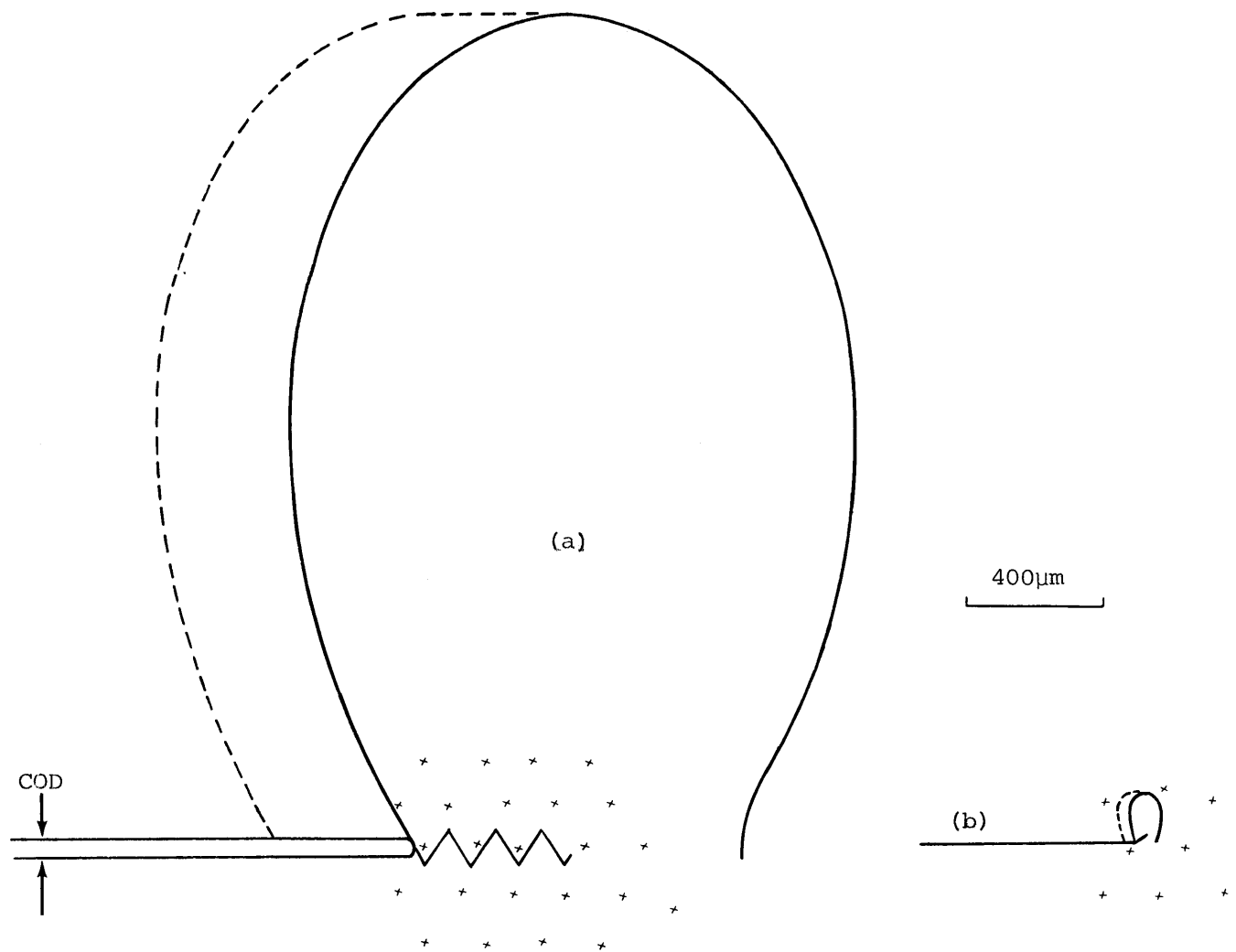


Figure 47 On-scale schematic drawings of calculated plastic zones and crack opening displacements, zig-zags, and 2D large inclusion spacing for two toughness levels of maraging 300 steel: (a) $K_{IC} \approx 140 \text{ ksi-in}^{1/2} / 153 \text{ MN-m}^{-3/2}$; (b) $K_{IC} = 50 \text{ ksi-in}^{1/2} / 55 \text{ MN-m}^{-3/2}$.

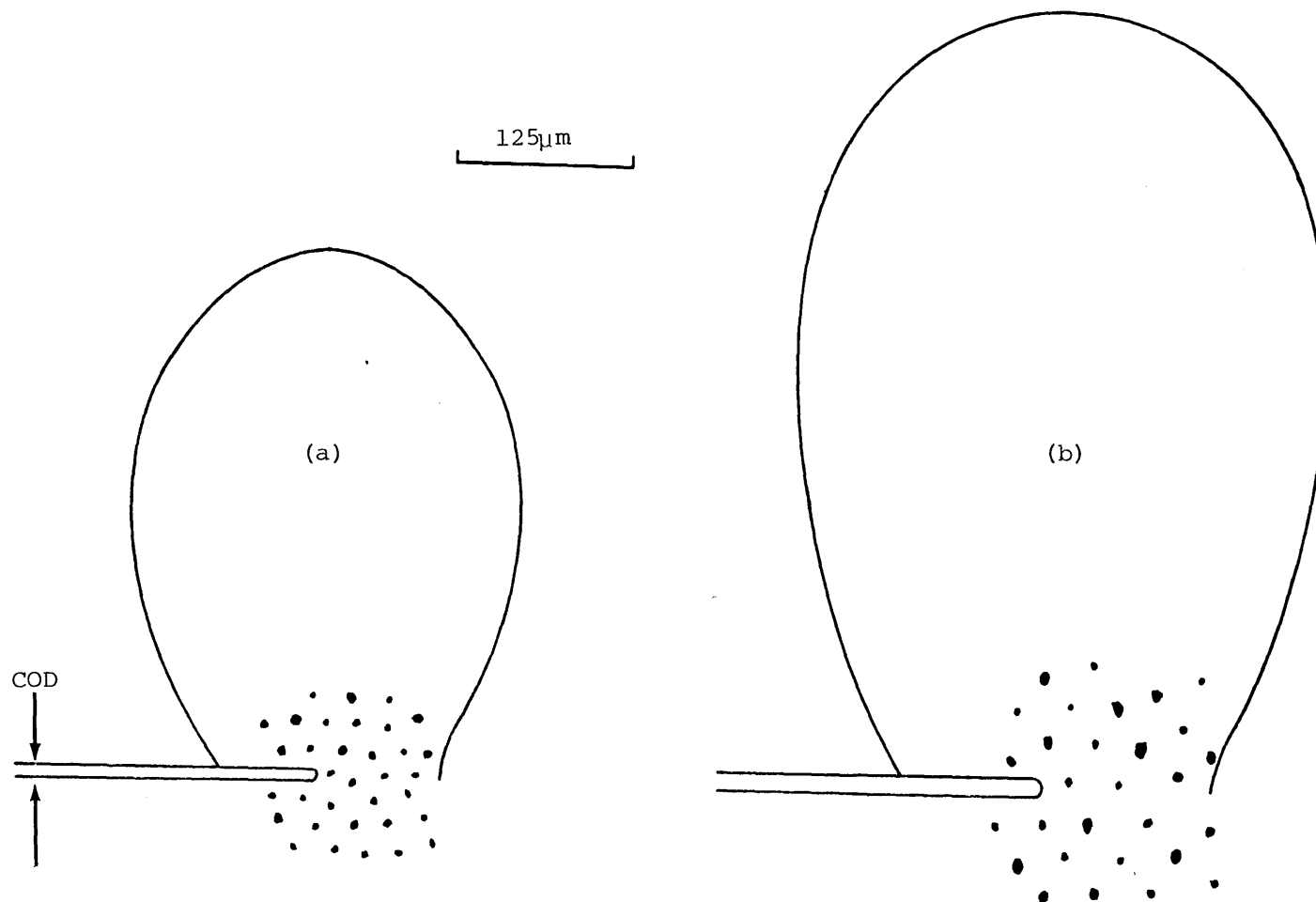


Figure 48 On-scale schematic drawing of calculated plastic zones, calculated crack opening displacements, and 2D large inclusion spacings of (a) 7075-T6; (b) 7475-T651.

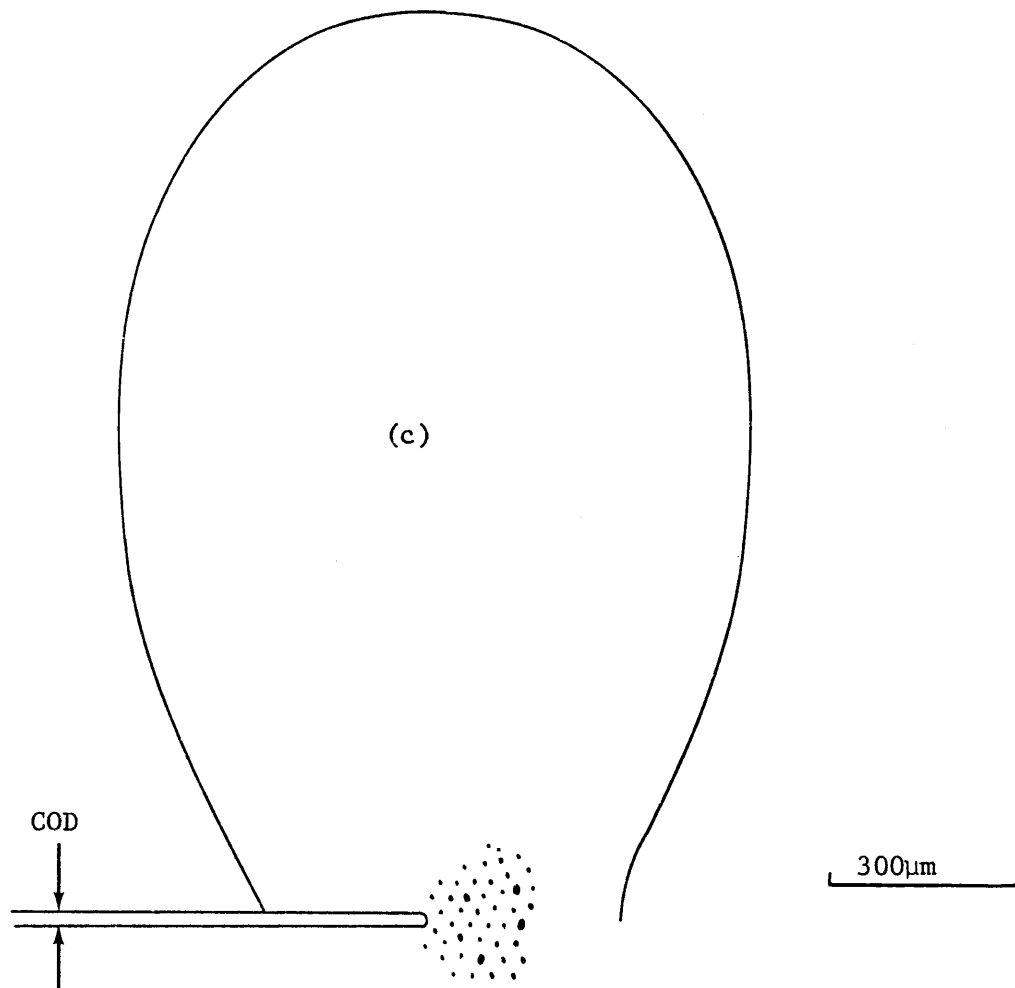


Figure 48 (cont.) (c) 2024-T4 aluminum alloys.

5.2.1 ROLE OF LARGE INCLUSIONS IN CRACK PROPAGATION

Two toughness levels of 4340 steel are depicted in Figure 46. For both cases the zig-zag spacing is much smaller than both the 2D and 3D spacing of large inclusions (Table 4) and the plastic zone dimensions. For this reason, spacing of large voids due to these inclusions (Figure 22 and 39a) tend to approximate the 2D spacing of the large inclusions, since the zig-zagging crack plane intersects large inclusions about as often as a planar interface. Spacing of the smaller ($<1\mu\text{m}$) inclusions in 4340 steel is equal to or less than the ridge wavelength, and these inclusions tend to nucleate voids which form on the ridge sides and break up the uniformity of the peaks and valleys. The zig-zags become less regular as the wavelength decreases with decreasing toughness down to a length equal to the spacing of the smaller inclusions. The smaller inclusions ($0.1-1\mu\text{m}$) then become relatively more important in the fracture process. Thus in plane strain propagation in this very clean 4340 steel, the widely spaced inclusions do not contribute significantly to the fracture process. Smaller inclusions interfere with the formation of uniform ridges, especially at low toughness levels.

The volume fraction of large inclusions in maraging 300 steel (Table 4) is several times greater than in 4340 steel, and the particle spacing is correspondingly smaller. Ridge wavelength for the high toughness ageing treatment of maraging

300 steel in Figure 47a is close to the 2D large inclusion spacing. For this reason the fracture surface contains a greater number of large voids nucleated at big inclusions than does 4340 steel, and the ridges on the surface are not as well formed as on 4340 steel. At lower toughness levels and for shorter wavelength the maraging steel (Figure 47b) inclusions range in size from 0.5 to $1\mu\text{m}$, and their spacing is such that voids which form around them tend to disrupt the zig-zagging process. The ridges become less regular at shorter wavelengths.

All the analyses by Hahn and Rosenfield⁽²⁸⁾, Krafft⁽²¹⁾, and Broek⁽⁹⁾, as discussed in Section 2.4, attempt to relate K_{IC} to the average inclusion spacing, by assuming that fracture is controlled by the coalescence of individual voids formed around large inclusions. In this research, observations of two clean steels have shown that large voids around the large inclusions do not contribute greatly to the total fracture process. Hahn and Rosenfield have shown that their relationship (Eq. 19) can correctly relate the K_{IC} dependence on particle volume fraction (f) as $f^{-1/6}$ for several alloys of equivalent strength. However, numerical solutions of this equation for the strength levels of 4340 and maraging 300 steels yield too large values of K_{IC} and also predict K_{IC} to increase with σ_y . This suggests that criteria for fracture by zig-zagging is more easily satisfied at very large

inclusion spacings than the criteria for fracture by growth and coalescence of large voids. Thus the $f^{-1/6}$ dependence would be valid only down to a volume fraction where zig-zagging could occur.

Aluminum alloys 2024-T4 and 7075-T6 both contain approximately 3 volume percent inclusions, an order of magnitude greater than the maraging 300 steel and two orders of magnitude times the value of 4340 steel (Table 4). This greater density is seen by comparing Figure 48a, c to Figures 46 and 47 for the two steels; the lower volume fraction of particles present in 7475-T651 is shown in Figure 48b.

The great majority of the fracture surface of 2024 and 7075 consists of large voids (10 to 20 μ m) which form around large particles (Figure 41b). Since no zig-zags were observed on the aluminum alloys, crack propagation and toughness are evidently controlled by void initiation and growth around individual inclusions and link up by shear between these voids. It is known that voids tend to form first around large inclusions, and since there is such a large number of particles in 2024 and 7075, criteria for propagation by this mechanism must be satisfied more easily than the stress and strain criteria for zig-zagging. Hahn and Rosenfield⁽²⁸⁾ showed that K_{IC} varies as $f^{-1/6}$ for 2024 and 7075, which fits this model of coalescence of large voids in the high inclusion density aluminum alloys.

5.2.2 DELAMINATION IN ALUMINUM ALLOYS

The schematic plastic zone in Figure 48b for 7475-T651 is very approximate because the large amount of grain boundary delamination observed in this alloy decrease the thru thickness constraint within the center portions of the specimen and invalidate the numerical solutions⁽³⁾ used to generate Eqs. 1-3 for r_p^y , r_p^x , and COD.

Grain boundary delamination in high-purity high-strength aluminum alloys has been previously reported. Joyce⁽⁶⁵⁾ saw grain boundary cracks parallel to the applied stress direction in fully plastic plane strain specimens of high purity 7075. Levy⁽⁶⁴⁾ also observed delaminations in fracture toughness tests of high purity 7075. The author is not aware of any systematic work done to determine the cause of this delamination. Joyce observed very fine dimples on the sides of the delaminated boundaries in 7075 which suggests that grain boundary precipitates may cause fracture. The present observations of 7475 show heavily sheared sides with few well-formed dimples. Since some delaminations are seen even on the alloys containing a large volume fraction of inclusions (2024 and 7075), it is not clear whether increased purity weakens the grain boundary structure or whether the lower inclusion content raises fracture toughness to a level where the increased transverse stresses pull apart the boundaries.

The extent of delamination in aluminum alloys with low

inclusion content complicates any analytical attempt to model fracture toughness. The increase of delamination with purity produces an overall change in deformation mode and could put a lower limit on the applicability of Hahn and Rosenfield's $f^{-1/6}$ variation of K_{IC} . Figure 43 shows that the scale (depth) of intergranular cracking is greater than the calculated plastic zone size for 7475-T651, thus invalidating the application of the results of Rice and Johnson⁽³⁾ to describe crack tip conditions for this material.

The influence of delamination on toughness would depend on the specimen orientation: when the applied stress is along the rolling plane of the plate, delamination along planes parallel to the rolling plane separates the material in the plastic zone into thin sheet ligaments which are essentially under a plane stress condition since they are only a few times the grain thickness. The "plane strain" fracture surface of 7475-T651 fracture toughness specimens is a typical example of extensive delaminations parallel to the rolling plane. Delamination in this specimen orientation will result in an increase in toughness since plastic deformation will occur over a larger volume, requiring more energy to propagate a crack. Fracture toughness testing of multilayered adhesive-bonded plates of 7075 by Kaufman⁽⁶⁶⁾ support this conclusion: the K_C value for a 1.2cm panel made up of eight layers of 0.15cm sheet was twice that of a 1.2cm plate. On the other

hand, toughness of specimens with the crack plane parallel to the rolling plane could be decreased if the crack followed weak intergranular boundaries.

5.2.3 CRACK INITIATION AND PROPAGATION BY ZIG-ZAGGING

It has been shown that the plane strain fracture surfaces of 4340 and maraging 300 steels are primarily composed of ridges and that the size of these ridges is a function of toughness. We have seen that the uniformity of ridge formation decreases with toughness, but the average microvoid size on the sides of the ridges does not change appreciably with toughness. This suggests that the particles responsible for the fracture voids on each flank of the ridges are relatively unaffected by heat treatment.

For the maraging 300 steel, these particles are very likely the small inclusions barely visible on optical micrographs with an average diameter of $0.2\mu\text{m}$ and a spacing of $2\mu\text{m}$ (in 3D), which roughly corresponds to the size of the small voids on ridges in this alloy (Figure 36). Roesch and Henry (12) observed these small particles on extraction replicas of fracture surfaces of a 250 grade maraging steel, and Rack and Kalish⁽⁶¹⁾ identified them as $\text{Ti}(\text{C},\text{N})$ using electron diffraction patterns in the transmission electron microscope. The sheared fracture surface of plane strain tensile specimens (Figure 38) also show dimples which have roughly the same

size as the ridge-side voids and which are thought to be nucleated at the same small inclusions.

Ridge-side voids on 4340 steel are very fine, with many voids less than $1\mu\text{m}$ in diameter (Figure 35). The plane strain tensile fracture surfaces of this steel also show voids more uniform in size which average less than $1\mu\text{m}$ (Figure 37). No inclusions are visible optically to account for these fine dimples. As discussed in Section 3.1.1, carbides range in size from 0.05 to $0.1\mu\text{m}$ and are very likely the particles which nucleate the voids responsible for zig-zag formation in 4340 steel. Cox and Low⁽²⁹⁾ arrived at a similar conclusion to account for void sheet formation of the fine cracks which link up larger voids formed around the inclusions at the center of round-bar tensile specimens of 4340. They reasoned that the toughness of 4340 can be lowered by the extensive shear interconnection of large voids by these sheets of small voids. The limited extent of the growth and coalescence of the large voids results in decreased overall plasticity and low fracture toughness.

Fractography and polished sections of specimens in Chapter IV demonstrated the zig-zagging begins immediately after the initial "sheared off" or "stretched" zone, and it propagates on alternating 45° planes. The fatigue pre-crack tip blunts in the manner predicted by Rice and Johnson⁽³⁾, but all microscopic observations indicate that the zig-

zagging crack tip is sharp. Thus the stress state (Figure 5) for the blunted geometry (Figure 4) calculated by Rice⁽³⁾ will apply up to initiation, but a sharp tip stress distribution (Figures 2 and 3) should be more applicable to describe zig-zagging crack propagation. These differences in geometries suggest that processes of crack initiation and propagation should be treated separately; we shall first discuss propagation by zig-zagging.

Observations of sectioned cracks (Figures 30-32) show that microvoid formation is essentially limited to the ridge surfaces; the only voids which occur below the surface are nucleated at large inclusions, and these are rarely observed because of the wide spacing of large inclusions. This observation appears to rule out the applicability of Berg's⁽³²⁾ analysis to explain zig-zag formation on the basis of the presence of a "cheezy" microporous region in front of the crack tip. The fact that voids form only on the fracture surface, even though the ridges are formed within a part of the plastic zone which has been highly plastically strained, suggests that zig-zags progress along lines of very highly localized strain. At $\pm 45^\circ$ the lines correspond to the boundary line (Figure 2) between the region of high hydrostatic stress (B) and the region of $1/r$ shear strain singularity (C). This slip line pattern should be representative of the conditions ahead of a sharp tip for 4340 and maraging 300 steels

since they have very low work hardening and approach ideal elastic-plastic behavior.

Comparison of void morphologies on ridge sides and on plane strain tensile specimen surfaces suggests that hydrostatic stresses play an important role on void formation in zig-zagging. Voids on the plane strain tensile specimens are virtually all shear voids; this is expected since triaxiality is low in this specimen geometry and fracture occurs along the 45° surface of maximum shear stress and shear strain. Ridge-side voids are comprised of a combination of tear dimples, indicative of Mode I loading, and shear dimples (Mode II loading). Beachem and Yoder⁽³⁴⁾ also reported observing a mixture of tear and shear voids. The greater number of larger voids (1 to $5\mu\text{m}$ in 4340 steel) on ridge sides as compared to plane strain tensile specimen surfaces indicates that higher hydrostatic stresses contribute to void growth for zig-zagging. Thus zig-zags appear to propagate along a band where the highest hydrostatic stress can be combined with the highest localized shear strain. This observation agrees with a fracture criteria proposed by McClintock⁽⁴⁾ and Carson⁽⁵⁾.

The data of Figures 27-29 which shows that a strong correlation exists between ridge spacing, applied elastic critical stress intensity (K_{IC}), and calculated COD and plastic zone sizes, imply that the width of the ridges is

controlled primarily by stress and strain fields existing within the plastic zone; naturally these local plastic stresses and strains are a function of the surrounding applied elastic fields. However the hydrostatic stress intensity within the plastic zone is a function of yield stress and work hardening, and it will increase with both σ_y and n , as shown by Rice and Johnson⁽³⁾. The size of the plastic zone is determined by both material properties (σ_y and n) and the surrounding applied elastic stress field, the strength of which is described by K . These relationships are expressed by Eq. 1 and 2. The distribution of strains within the plastic zone should be independent of size if strain history effects, such as work hardening or void formation are ignored. Carson⁽⁵⁾ and Hahn and Rosenfield⁽²²⁾ suggest that work hardening smooths out strain gradients, but for the present discussion this effect will be ignored since these materials work harden very little.

Zig-zagging crack propagation is proposed to occur by the following steps:

- 1) Within the plastic zone a crack leg grows upward at a 45° angle following a line of constant hydrostatic stress. As it propagates further out into the plastic zone, the front of the crack leg sees the plastic strain decrease as the reciprocal of the distance from the tip.

- 2) A crack leg grows at 45° to a distance where the local plastic strain combined with the local hydrostatic stress are too low to satisfy the critical combined stress-strain criteria for void sheet formation. At this position the crack front sees a higher plastic strain field at the edge of a new slipline fan 90° downward (45° to the macroscopic plane) which will satisfy the stress-strain fracture criterion, and it changes direction.
- 3) The crack proceeds downward until it reaches the same conditions as it had at the end of step 2 and it will change its direction again. As the crack propagates the plastic zone also advances in front of the crack.

This model predicts that the ridge side length and spacing increases with increasing toughness because the size of the plastic zone increases with K_{IC} , and the crack can propagate further before it reaches the fracture strain limit where it changes direction. A secondary effect shown in the data of Figure 28, which plots λ versus r_p^y and r_p^x , is that λ is a larger fraction of r_p^x at lower K_{IC} . Toughness decreases with increasing yield strength; so for the low toughness specimens the hydrostatic stress is higher. Recalling that the plastic zone size changes with K , but the relative plastic

strain distribution is unchanged; the critical strain for the change of direction must decrease at higher hydrostatic stress, since the ridge length is a relatively greater fraction of the plastic zone size at low K_{IC} . Thus the combined shear strain-hydrostatic stress failure criteria should be such that the minimum fracture strain decreases with increased stress. This is reasonable since higher strains can a) aid void initiation through stress intensification at dislocation pileups or b) aid void coalescence by growth of voids by shear, as in the plane strain tensile specimens.

The possibility that dynamic effects influence zig-zag crack propagation should be considered. One problem is that the available analytical solutions for plastic zone size and crack opening displacement strictly apply only for static or non-propagating crack tips. The solutions of Rice and Johnson⁽³⁾ which have been used here are based in part on crack tip singularity relationships developed by Hutchinson⁽⁶⁷⁾ and Rice and Rosengren⁽⁶⁸⁾; expressions for these singularities were developed using deformation plasticity, which assumes that no unloading occurs. During zig-zag crack propagation unloading does occur, so the applicability of Eqs. 1-3 is open to question. The shape and size, then, of a rapidly moving plastic zone in this type of material has not been analytically solved, and no results of other experimental work have been found to help explain the problem. In

any case, the data of Figures 27-29 demonstrate that there is a direct relationship between ridge spacing and the measured "static" fracture toughness.

It does appear that high velocity crack propagation is not a prerequisite for zig-zag formation. Earlier work by Beachem and Yoder⁽³⁴⁾ showed that zig-zags form during slow crack growth in hydrogen assisted cracking of a 13r-8Ni-2Mo stainless steel. In the present investigation, ridges were observed on surfaces of fracture toughness specimens which were pulled open very slowly in overload fracture at the slowest displacement rate of the testing machine. Thus while dynamic effects conceivably could change the size of the plastic zone by strain rate variations of the yield stress, high crack growth rates are not necessary to cause formation of ridges.

The data of Figure 29 show that λ is linearly related to K_{IC}^2 for both steels. This can be rationalized by examining solutions of the Hutchinson⁽⁶⁷⁾, Rice and Rosengren⁽⁶⁸⁾ (HRR) singularity for plastic strains near the tip of a sharp crack in a work hardening material. The strains are expressed in terms of the path independent J_1 integral of Rice⁽⁷⁰⁾ by the equation:

$$\varepsilon_{ij}(r, \theta) = \left[\frac{J_I}{\bar{\sigma}_1 I_n r} \right]^{1/n+1} \tilde{\varepsilon}_{ij}(\theta) \quad \text{Eq. 24}$$

where

$$\sigma = \bar{\sigma}_1 (\bar{\varepsilon}^P)^n \quad \text{Eq. 25}$$

is the uniaxial stress-strain relation and $\tilde{\varepsilon}_{ij}(\theta)$ and I_n are functions of n and θ which have been evaluated numerically by Hutchinson⁽⁶⁷⁾. For a non work hardening material $n = 0$ and $\sigma = \sigma_y = \bar{\sigma}_1$; in this case the strain distribution is equivalent to the Prandtl slipline field of Figures 1 and 2. The Prandtl field solution for the shear strain dependence on angle, $\tilde{\varepsilon}_{r\theta}(\theta)$, for $n = 0$ is:

$$\begin{aligned} \tilde{\varepsilon}_{r\theta} (0 \leq \theta < 45^\circ) &= 0 \\ \tilde{\varepsilon}_{r\theta} (45^\circ < \theta < 135^\circ) &= .7 \\ \tilde{\varepsilon}_{r\theta} (135^\circ < \theta \leq 180^\circ) &= 0 \end{aligned} \quad \text{Eq. 26}$$

This predicts a discontinuous increase in shear strain at $\theta = 45^\circ$. Solutions for $\tilde{\varepsilon}_{r\theta}(\theta)$ for work hardening materials⁽⁷¹⁾ show the step function at $\theta = 45^\circ$ and 135° to be

smoothed out; that is, shear strain gradients at constant r decrease with increasing n .

We have proposed that zig-zagging follows a path of 45° to the macroscopic fracture plane approximately along this line of high shear strain gradient in the θ direction. For our case of low work hardening material, if we use an approximation of $n \approx 0$, the strain from Eq. 24 along a line at θ slightly greater than 45° becomes:

$$\epsilon_{r\theta}(r, 45^\circ) = \frac{0.7J_I}{\sigma_y r I_n} \quad \text{Eq. 27}$$

The model for zig-zag propagation suggests that the length of a ridge side is determined by the distance to reach a critical strain ($\epsilon_{r\theta}^c$). If this strain occurs at a distance r_c at 45° , the wavelength is geometrically related to r_c by:

$$r_c = 0.707\lambda \quad \text{Eq. 28}$$

Substituting into Eq. 27 gives:

$$\epsilon_{r\theta}^c \approx \frac{J_{IC}}{\sigma_y \lambda I_n}$$

or,

$$J_{IC} \approx I_n \lambda \epsilon_{r\theta}^c \sigma_y \quad \text{Eq. 29}$$

$$J_{IC} \propto \lambda \quad \text{Eq. 30}$$

Rice has shown that for specimens which satisfy requirements for valid K_{IC} testing:

$$J_{IC} = \frac{(1-\nu^2)K_{IC}^2}{E} \quad \text{Eq. 31}$$

Thus: $K_{IC}^2 \propto J_{IC} \propto \lambda$ Eq. 32

This result should not change greatly for small amounts of work hardening since a) numerical calculations of $\epsilon_{r\theta}$ still show a sharp rise in $\epsilon_{r\theta}$ with increasing θ at constant r and b) the function $1/(1+n)$ is close to 1 for values of n measured for the two steels.

Equation 32 predicts that λ should be proportional to K_{IC}^2 . The data of Figure 20 shows λ varies linearly with K_{IC}^2 , but the curves do not extrapolate to zero λ at zero K_{IC}^2 . The reason for the shift in the curve to positive values of λ at zero K_{IC}^2 cannot be satisfactorily explained at this time. However, it does appear that a critical strain criteria for void formation along lines of localized shear

strain described by the HRR crack tip singularity solution can predict a linear relationship between λ and K_{IC}^2 .

Comparison of toughness and yield strength data for 4340 and maraging 300 steels (Tables 5 and 7) shows that maraging 300 is tougher at equivalent strength conditions. Ridge spacings (Table 7 and Figure 29) are also greater for the maraging steel at a given K_{IC} level. Finally, the ridge side voids on maraging 300 are larger than for 4340, averaging 1 to 5 μ m in maraging 300 versus less than 1 μ m in 4340. The differences in ridge spacing and ridge void size between these two alloys suggests that the combined stress-strain failure criterion could be a function of the properties of the particles which nucleate these voids. These factors would include size, spacing, and metal-particle bonding characteristics:

- a) Larger particles tend to nucleate voids at lower stresses and strains than small particles.
- b) Coalescence of widely spaced voids should require more plastic deformation and energy than closely spaced voids.
- c) Weakly bonded particles can initiate voids at lower stresses and strains than well-bonded particles.

These factors give some guidelines to the metallurgist who would like to further improve the toughness of alloys after removing the large inclusions at considerable cost and effort. It is possible that higher toughness may be achieved by control of these small particles which provide for zig-zag formation.

Following this work we can give a description of the most important structural features which should be taken into account by the stress analyst who might attempt a numerical solution to predict crack propagation by zig-zagging. A prerequisite to such a treatment is a satisfactory mechanics solution for the plane strain near-tip plastic stress and strain fields; hopefully this will be available in the future. The stress-strain curve for a particular material would be factored into the mechanics crack tip solution. This simple model is suggested:

- 1) Small particles ranging from 0.05 to 0.5 μ m in diameter should be considered as void initiation sites.
- 2) The 3D spacing-to-diameter ratio of such particles should be on the order of 10 to 1.
- 3) Voids would initiate on the particles when a critical normal stress is reached. This stress would be low for particles which debond easily from the matrix

and would be higher for those which crack or deform plastically.

These suggestions when combined with the needed plastic stress-strain distribution should lead to a zig-zagging crack path. The analytical solutions must be checked against experimental results reported in this thesis:

- localized void formation and cracking at $\pm 45^\circ$ angles.
- linear relationship between ridge spacing and K_{IC}^2 .
- lower critical strain for void formation at high hydrostatic stress.

Development of this analytical solution would be very useful: it would provide numerical calculations of the dependence of K_{IC} on size, spacing, and bonding characteristics of small particles.

CHAPTER VI: CONCLUSIONS

1. Current fracture toughness theories do not adequately relate tensile properties to K_{IC} for several strength levels of 4340 steel and maraging 300 steel. Stress and strain distributions in the tensile tests are not comparable to crack tip conditions, and the scale of second phase particles must be considered.
2. For metals with high volume fraction of inclusions, such as commercial high strength aluminum alloys and dirty steels, fractography shows that fracture at the crack tip is governed by growth and coalescence of large voids around large inclusions. K_{IC} is proportional to $f^{-1/6}$ for equivalent strength levels.
3. At very low inclusion densities in electroslag remelt 4340 steel and vacuum melted maraging 300 steel, fracture occurs by a process of zig-zagging or ridge formation on a fine scale above and below the macroscopic fracture plane. Large inclusions are too widely spaced to control crack propagation and toughness.
4. Zig-zags follow paths of highly localized shear strain at directions $\pm 45^\circ$ to the macroscopic fracture surface.

The crack tip remains sharp, and no voids are nucleated below the local fracture surfaces. A combined hydrostatic stress-localized shear strain criteria can explain the zig-zag path.

5. The spacing, λ , of zig-zags is found to increase linearly but not proportionally with K_{IC}^2 when toughness is varied by tempering in 4340 and ageing in maraging 300. λ appears to be related to a critical strain for void formation along lines of localized shear strain described by the HRR crack tip singularity solution.

6. For a given steel, void sizes on ridge sides and plane strain tensile test fracture surfaces do not vary significantly with changes in toughness by over a factor of two. This implies that the nucleating particles do not change with toughness; these particles are thought to be small 0.2 μ m diameter inclusions in maraging 300 steel and 0.05 to 0.1 μ m diameter Fe_3C carbides in 4340 steel.

7. Ridge side voids are larger for maraging 300 steel than 4340 steel, and the maraging steel has a greater fracture toughness at equivalent yield strength. Metallurgical control of toughness may be possible through variations in the size, spacing, and bonding characteristics of the small inclusions responsible for these voids.

CHAPTER VII: SUGGESTIONS FOR FUTURE WORK

1. The dependence of zig-zag formation on crack propagation velocity should be studied using a fracture toughness specimen with which the crack growth rate can be controlled. A suitable specimen would be the constant compliance "bat wing" design where the stress intensity does not change with crack length at a given load. Crack growth rates could be varied by changing the displacement rate of the testing machine.

2. The possibility of improving the fracture toughness of clean high strength steels by varying the size, spacing, and bonding of submicron particles which nucleate microvoids on ridge sides should be investigated. This study should include statistical measurements to relate particle size and spacing to the microvoid size distribution.

3. A continuum mechanics solution for the near tip plastic stress and strain field in plane strain is needed to combine with the model based on void formation around small closely spaced particles. The analytical results from such a treatment should predict zig-zagging, and they would provide a useful tool to calculate effects on toughness of variations in particle size, spacing, and bonding characteristics.

4. Investigations should be conducted to determine the cause for extensive grain boundary delamination in the high purity, high strength, 7000 series aluminum alloys. Transmission electron microscope observations could show possible changes in grain boundary structure such as formation of grain boundary precipitates or solute depleted zones.

CHAPTER VIII: BIBLIOGRAPHY

1. Irwin, G.R., "Analysis of Stresses and Strains Near End of a Crack," J. Appl. Mech., Vol. 24, pp. 361-364.
2. Rogers, H.C., "Tensile Fracture of Ductile Metals," Trans. Met. Soc. AIME, Vol. 218, pp. 498-506.
3. Rice, J.R. and Johnson, M.A., "The Role of Large Crack Tip Geometry Changes in Plane Strain Fracture," Inelastic Behavior of Solids, M.F. Kanninen, et al, eds., Battelle Institute Materials Science Colloquia, Sept. 1969, McGraw-Hill, New York, 1970.
4. McClintock, F.A., "Crack Growth in Fully Plastic Grooved Tensile Specimens," Physics of Strength and Plasticity, A.S. Argon, ed., MIT Press, Cambridge, Mass., 1969.
5. Carson, J.W., "A Study of Plane Strain Ductile Fracture," Ph.D. Thesis, Department of Mechanical Engineering, Massachusetts Institute of Technology, 1970.
6. Bluhm, J.I., and Morrissey, R.J., "Fracture in a Tensile Specimen," Proc. of First Int. Conf. on Fracture (1965), Vol. 3, pp. 1739-1780.
7. Argon, A.S. and In, J., "Separation of Inclusions in Spheroidized 1045 Steel, Cu-0.6% Cr Alloy, and Maraging Steel in Plastic Straining," Structure and Property Control Through Rapid Quenching of Liquid Metals, Final Technical Report ARPA Contract No. DACH17 70 C 0283, Center for Materials Science and Engineering, Massachusetts Institute of Technology, Cambridge, Mass., 1973.
8. Palmer, I.G. and Smith, G.C., "Fracture of Internally Oxidized Copper Alloys," AIME Met. Soc. Conf., Vol. 47, Oxide Dispersion Strengthening, Bolton Landing, New York, (1966), G.S. Ansell, ed., Gordon and Breach, New York, 1968.
9. Broek, D., A Study on Ductile Fracture, Ph.D. Thesis, Delft, Netherlands, 1971.
10. Baker, C. and Smith G.C., "Some Observations on the Ductile Fracture of Polycrystalline Copper Containing Inclusions," Trans, AIME, Vol. 242, Sept., 1968, p.1989.

11. Gurland, J. and Plateau, J., "The Mechanism of Ductile Rupture of Metals Containing Inclusions," Trans. ASM, Vol. 56, 1963, p. 442.
12. Roesch, L. and Henry G., "Relationship Between Precipitation and Dimple Fracture in an 18% Nickel Maraging Steel," 1968 ASTM Annual Meeting, Symposium on Electron Microfractography, San Francisco, June, 1968.
13. McClintock, F.A., Kaplan, S.M., and Berg, C.A., "Ductile Fracture by Hole Growth in Shear Bands," Int. J. of Frac. Mech., Vol. 2, (1966), p.614.
14. McClintock, F.A., J. of Appl. Mech., Vol. 35, (1968), pp. 363-371.
15. McClintock, F.A., "Local Criteria for Ductile Fracture," Int. J. of Appl. Mech., Vol. 4, No. 2, June, 1968, p. 101.
16. Thomason, P.F., "A Theory for Ductile Fracture by Internal Necking of Cavities," J. Inst. of Metals, Vol. 96, (1968), pp. 360-365.
17. Rice, J. R., and Tracey, D.M., "On the Ductile Enlargement of Voids in Triaxial Stress Fields," Division of Engineering, Brown University, Providence, R.I., Technical Report No. 33, USAEC Contract No. AT(30-1)-2394, August, 1968.
18. McClintock, F.A. and Argon, A.S., Mechanical Behavior of Materials, Addison-Wesley, Reading, Mass., 1966, p.406.
19. Rice, J.R., J. Appl. Mech., Vol. 35, (1968) p. 379.
20. Levy, N., Ph.D. Thesis, Brown University, Providence, R.I., 1969.
21. Krafft, J.M., "Correlation of Plane Strain Crack Toughness with Strain Hardening Characteristics of a Low, a Medium, and a High Strength Steel," Applied Materials Research, April, 1964, pp.88-101.
22. Hahn, G.T. and Rosenfield, A.R., "Sources of Fracture Toughness: The Relation Between K_{IC} and the Ordinary Tensile Properties of Metals," Applications Related Phenomena in Titanium Alloys, ASTM STP432, ASTM, 1968, pp.5-32.

23. Hahn, G.T., Rosenfield, A.R., Hulbert, L.E., and Kanninen, M.F., "Elastic-Plastic Fracture Mechanics," Batelle Mem. Inst., Columbus Laboratories, Technical Report AFML-TR-67-143, January, 1968.
24. Hahn, G.T., Kanninen, M.F., and Rosenfield, A.R., "Fracture Toughness of Materials," Ann. Rev. Mat. Sci., Vol. 2, (1972) p.381.
25. Robinson, J.N. and Tetelman, A.S., "The Critical Crack-Tip Opening Displacement and Microscopic and Microscopic Fracture Criteria for Metals," UCLA Report No. UCLA-ENG-7360, U.S. Army Research Office, Durham, Contract No. DAHCO-69-C-0008, Technical Report No. 11, August, 1973.
26. Broek, D., "Correlation Between Stretched Zone Size and Fracture Toughness," Engr. Frac. Mech., Vol. 6, 1974, pp. 173-181.
27. Erhardt, K., "A Quantitative Fractographic Approach to Brittle Fracture," Material und Technik, No. 1, March, 1974, pp. 10-13.
28. Hahn, G.T. and Rosenfield, A.R., "Metallurgical Factors Affecting Fracture Toughness of Aluminum Alloys," 5th Annual Spring Meeting of the Met. Soc. of AIME, May, 1973.
29. Cox, T.B. and Low, J.R., "An Investigation of the Plastic Fracture of AISI 4340 and 18 Nickel-200 Grade Maraging Steels," Met. Trans., Vol. 5, June, 1974, pp/ 1457-1470.
30. Carr, F.L., Nunes, J., and Larson, F.R., Temper Embrittlement in Steel, ASTM STP No. 407, p. 203, American Society for Testing and Materials, Philadelphia, Pa., 1968.
31. Nunes, J., Carr, F.L., and Larson, F.R., Techniques for Metals Research, R.F. Bunshah, ed., Vol. 2, Part 1, p.379, John Wiley and Sons, Inc., New York, 1968.
32. Berg, C.A., Inelastic Behavior of Solids, M.F. Kenninen, ed., McGraw-Hill, New York, 1970.
33. Yoder, G.R., "Fractographic Lines in Maraging Steel - A Link to Fracture Toughness," Met. Trans., Vol. 3, July, 1972, pp. 1851-1859.

34. Beachem, C.D., and Yoder, G.R., "Elastic-Plastic Fracture by Homogeneous Microvoid Coalescence Tearing Along Alternating Shear Planes," Met. Trans., Vol. 4, April, 1973, pp. 1145-1153.
35. Krafft, J.M., Techniques of Metals Research, R.F. Bunshah, ed., Vol. 5, Part 2, p. 1, John Wiley and Sons, Inc., New York, 1971.
36. Cohen, M., "Strengthening Mechanisms in Steel," Proc. of the Int. Conf. on the Strength of Metals and Alloys, Japan Institute of Metals, Sendai, Japan, 1968.
37. Banerjee, B.R., Hanser, J.J., Fracture Micromechanics in High Strength Steels and Titanium, Technical Documentary Report ML-TDR-64-182, Air Force Materials Laboratory, July, 1964.
38. Baker, A.J., Lauta, F.J., and Wei, R.P., "Relationships Between Microstructure and Toughness in Quenched and Tempered Untrahigh-Strength Steels," Structure and Properties of Ultrahigh-Strength Steels, ASTM STP 370, Amer. Soc. for Testing and Materials, Philadelphia, Pa., 1965.
39. Averbach, B.L., Cohen, M., Trans. ASM, Vol. 41, p. 1024, 1949.
40. Kula, E.B., Anctil, A.A., "Tempered Martensite Embrittlement and Fracture Toughness in SAE 4340 Steel," J. of Materials, Vol. 4, p. 817, 1969.
41. Dehoff, R.T. and Rhines, R.N., Quantitative Microscopy, McGraw-Hill, New York, 1968.
42. Floreen, S., "The Physical Metallurgy of Maraging Steel," Met. Rev., Review 126, p. 115, 1968.
43. Miller, G.P., Mitchell, W.I., "Structure of Nickel-Cobalt-Molybdenum Maraging Steels in the Air-cooled Condition," J. Iron and Steel Inst., p. 203, 895, 1965.
44. Gilbert, A., Owen, W.S., "Diffusionless Transformation in Iron-Nickel, Iron-Chromium, and Iron-Silicon Alloys," Acta. Met., Vol. 10, p. 45, 1962.

45. Jones, R.W., Pumphrey, W.I., "Free Energy and Metastable States in the Iron-Nickel and Iron-Maganese Systems," J. Iron and Steel Inst., Vol. 163, p. 122, 1949.
46. Goldberg. A., O'Conner, D., "Influence of Heating Rate on Transformations in an 18 Percent Nickel Maraging Steel," Nature, Vol. 170, January, 1967.
47. Mihalisin, J.R., "Fifty Years of Progress in Physical Metallographic Techniques," Effect of Carbon Content on Transformation Structures of Iron-22 Percent Nickel Alloys, ASTM STP 430, p. 250, 1968.
48. Goldberg, A., "Morphology of Martensite Formation in a 300 Grade Maraging Steel," Trans, ASM, Vol. 62, p. 219, 1969.
49. Winchell, P.G., Cohen, M., "The Strength of Martensite," Trans. ASM, Vol. 55, p. 347, 1962.
50. Bourgeot, J., Maitrepierre, P.H., Manena, J., Thomas, B., "Dircossem, emt Par Renenu Des Martensites Fe-Ni-Mo et Fe-Ni-Co-Mo," Institute de Recherches de la Siderrurgie Fransaise, IRS.D, Vol. 167, October, 1972.
51. Marcus, H., Schwartz, L.W., Fine, M.E., "A Study of Precipitation in Stainless and Maraging Steels Using the Mossbauer Effect," Trans. ASM, Vol. 59, p. 468, 1966.
52. Floreen, S., Speich, G.R., "Some Observations on the Strength and Toughness of Maraging Steels," Trans. ASM, Vol. 57, p.714, 1964.
53. Banerjee, R.B., Hanser, J.J., "Hardening Mechanisms and Delamination Studies of 18 Percent Nickel Maraging Steels," Wright-Patterson AFB, Technical Report AFML-TR-66-166, 1965.
54. Van Swam, L.F.P., "Fatigue Behavior of Maraging Steel 300," Sc.D. Thesis, Department of Metallurgy and Materials Science, Massachusetts Institute of Technology, 1973.
55. Boyd, J.D., Drennen, D.C., Martin, C.H., Price, C.W., Rosenfield, A.R., Williams, D.N., Thompson, D.S., "Research on Sythesis of High Strength Aluminum Alloys," Technical Report AFML-TR-72-199, July 1, 1971 to July 31, 1972, Air Force Avionics Laboraotry, Wright-Patterson AFB, Ohio.

56. Dieter, G.E., Mechanical Metallurgy, McGraw-Hill, 1961.
57. Ghosh, A.K., "Strain Hardening and Instability in Biaxially Stretched Sheets," Ph.D. Thesis, Department of Metallurgy and Materials Science, Massachusetts Institute of Technology, August, 1972.
58. Backofen, W.A., Deformation Processing, Addison-Wesley, Reading, Mass., 1972.
59. Selines, R.J., "Fatigue Behavior of High Strength Aluminum Alloys," Sc.D. Thesis, Department of Metallurgy and Materials Science, Massachusetts Institute of Technology, February, 1975.
60. Rice, J.R., Proc. Third Int. Conf. on Fracture, Vol. 2, (1973), Paper I-441.
61. Rack, H.J. and Kalish, D., "The Strength and Fracture Toughness of 18Ni(350) Maraging Steel," Met. Trans., vol. 2, 1971, pp. 3011-3020.
62. Matthews, W.T., "Plane Strain Fracture Toughness (K_{IC}) Data Handbook for Metals," AMMRC MS 73-6 Army Materials and Mechanics Research Center, Watertown, Mass., 1973.
63. Jones, M.H. and Brown, W.F., "The Influence of Crack Length and Thickness in Plane Strain Fracture Toughness Tests," Review of Developments in Plane Strain Fracture Toughness Testing, ASTM STP 463, American Society for Testing and Materials, 1970, pp. 63-101.
64. Levy, S.A., "The Effect of Homogeneity on the Properties Of 7075 Aluminum," Project No. 38-ACC-221B, Metallurgical Research Division, Reynolds Aluminum Corp., June, 1970.
65. Joyce, J., "On the Mechanisms and Mechanics of Plastic Flow and Fracture," Sc.D. Thesis, Department of Mechanical Engineering, Massachusetts Institute of Technology, May, 1974.
66. Kaufman, J.G., "Fracture Toughness of 7075-T6 and -T651 Sheet, Plate, and Multilayered Adhesive-Bonded Panels," Trans, ASME, J. of Basic Engineering, September, 1967, pp. 503-507.

67. Hutchinson, J.W., J. Mech. Phys. Solids, Vol. 16, (1968), p. 13.
68. Rice, J.R. and Rosengren, G.F., "Plane Strain Deformation Near a Crack Tip in A Power Law Hardening Material," J. Mech. Phys. Solids, Vol. 16, (1968), pp. 1-12.
69. Pelloux, R.M.N., Private communication.
70. Rice, J. R., "A Path Independent Integral and the Approximate Analysis of Strain Concentration by Cracks and Notches," J. Appl. Mech., Vol. 35, pp. 379-386.
71. McClintock, F.A., "Plasticity Aspects of Fracture," Fracture, H. Liebowitz, ed., Vol. 3, Academic Press, New York, 1971.

BIOGRAPHICAL NOTE

The author was born on September 13, 1946 in South Bend, Indiana. He resided in Mishawaka, Indiana where he graduated from Mishawaka High School in 1964. He then attended Purdue University, where he received the degree of Bachelor of Science in Metallurgy in June, 1968.

On June 15, 1968 he married the former Carol Lynn Havens, also of Mishawaka. He was employed by Sandia Laboratories of Albuquerque, New Mexico during the summer of 1968 and enrolled at M.I.T. that fall under Sandia's One Year on Campus Program. He graduated with a Master of Science degree in August, 1969 and returned to Sandia.

In August, 1971 he returned to M.I.T to begin work on his doctoral program; during the 1972 and 1973 academic years he was financially supported by Sandia's Doctoral Study Program. Upon graduation, he will continue employment at Sandia Laboratories.